

**MEASUREMENTS OF LEAKAGE, POWER LOSS AND  
ROTORDYNAMIC FORCE COEFFICIENTS IN A  
HYBRID BRUSH SEAL**

A Thesis

by

JOSE ENRIQUE BAKER

Submitted to the Office of Graduate Studies of  
Texas A&M University  
in partial fulfillment of the requirements for the degree of

MASTER OF SCIENCE

May 2008

Major Subject: Mechanical Engineering

**MEASUREMENTS OF LEAKAGE, POWER LOSS AND  
ROTORDYNAMIC FORCE COEFFICIENTS IN A  
HYBRID BRUSH SEAL**

A Thesis

by

JOSE ENRIQUE BAKER

Submitted to the Office of Graduate Studies of  
Texas A&M University  
in partial fulfillment of the requirements for the degree of

MASTER OF SCIENCE

Approved by:

Chair of Committee, Luis San Andrés

Committee Members, Dara Childs

Helen Reed

Head of Department, Dennis L. O'Neal

May 2008

Major Subject: Mechanical Engineering

## ABSTRACT

Measurements of Leakage, Power Loss and Rotordynamic Force Coefficients  
in a Hybrid Brush Seal. (May 2008)

José Enrique Baker, B.S., University of New Orleans

Chair of Advisory Committee: Dr. Luis San Andrés

This thesis presents measurements of power loss and leakage in a hybrid brush seal (HBS) for increasing pressure differentials and over a range of rotor speeds. The test HBS, Haynes-25 bristle pack [ $\sim 850$  bristles/cm] and  $45^\circ$  lay angle, is 166.4 mm in diameter and integrates 20-arcuate pads connected with thin EDM-webs to the seal casing.

The measured drag power at low rotor speeds ( $< 11$  m/s at 1,300 rpm) decreases as the pressure differential across the seal increases. At a fixed rotor speed, a significant drop in drag torque (and drag power) ensues as the supply pressure increases, thus demonstrating a gas film separates the rotor from the seal pads. A constant operating temperature ( $\sim 24^\circ\text{C}$ ) at the rotor/seal interface during tests with shaft rotation also indicates the absence of intermittent contact between the seal pads and rotor.

Flow rate measurements at room temperature ( $25^\circ\text{C}$ ) show an improved sealing ability with a leakage reduction of about 36%, when compared to a 1<sup>st</sup> generation shoed-brush seal. The HBS predicted effective clearance ( $\sim 50$   $\mu\text{m}$ ) is a small fraction of that in an equivalent one-tooth labyrinth seal.

Identified HBS direct stiffness coefficients decrease ( $\sim 15\%$ ) as function of rotor speed for an increasing supply pressure condition ( $P_r = 1.7$  and  $2.4$ ). The identified cross-coupled stiffness is at least one or two orders of magnitude smaller than the direct stiffness coefficient. The cross-coupled mass is negligible for all tested rotor speeds and supply pressures. The HBS energy dissipation mechanism is characterized in terms of a loss factor ( $\gamma$ ) and dry friction coefficient ( $\mu$ ). The direct HBS viscous damping

coefficient is strongly dependent on the excitation frequency, while showing minimal dependence on rotor speed or supply pressure.

The HBS novel configuration incorporates pads contacting on assembly the shaft; and which under rotor spinning; lift off due to the generation of a hydrodynamic pressure. Experimental results obtained show that hybrid brush seals (HBS) are a viable alternative to overcoming the major drawbacks of labyrinth seals; namely excessive leakage and potential for rotordynamic instability. Additionally, during operation a gas film in HBS eliminates rotor and bristle wear, as well as thermal distortions; which are commonly known limitations of conventional brush seals.

## **DEDICATION**

To my grandmother, Carmen Varela, and to my mother, Xamiry Villalobos, for their unconditional love, guidance and numerous sacrifices. To them I owe all my personal and professional victories. Your love fills my heart everyday. To my father, José Enrique Baker, even though he is not with me anymore I believe he guides my steps from heaven.

## **ACKNOWLEDGEMENTS**

I thank Dr. Luis San Andrés, my committee chair and advisor, for granting me the opportunity to join the Tribology group at Texas A&M University Turbomachinery Laboratory. His financial support and technical advice are greatly appreciated.

I especially thank my colleague and friend, Adolfo Delgado, for his help during the early and final stages of my investigation. Thanks for sharing the knowledge you gained from working at the Turbomachinery Laboratory prior to my arrival. To all my other colleagues, Ahmed Gamal, Arun Suryanarayanan, Aaron Schomerus, and Joel Harris, with whom I shared technical and personal experiences.

## NOMENCLATURE

$A$	Shaft cross-sectional area [m <sup>2</sup> ]
$B_w$	Brush seal width [m]
$C_{eq}$	Seal equivalent viscous damping coefficient [N-s/m]
$C_{\alpha\beta}$	System damping coefficient [N-s/m], $\alpha, \beta = x, y$
$C_{sa\beta}$	Seal damping coefficient [N-s/m], $\alpha, \beta = x, y$
$D_j$	Rotor diameter [m]
$D_{Si}$	Brush seal inner diameter [m]
$D_o$	Brush seal outer diameter [m]
$E_{dis}$	Energy dissipated in one period of forced motion [J]
$F_{ext}$	Excitation force [N]
$K_{eq}$	Equivalent stiffness for test system [N/m]
$K_{shaft}$	Shaft stiffness [N/m]
$K_s$	Brush seal structural stiffness [N/m]
$K_{\alpha\beta}$	System stiffness coefficient [N/m], $\alpha, \beta = x, y$
$K_{sa\beta}$	Brush seal stiffness coefficient [N/m], $\alpha, \beta = x, y$
$L$	Shaft length [m]
$M_{eq}$	System equivalent mass [kg]
$M_D$	Disk mass [kg]
$M_{\alpha\beta}$	System mass [kg], $\alpha, \beta = x, y$
$P_e$	Electrical power [W]

$P_d$	Absolute discharge pressure [Pa]
$P_s$	Absolute supply pressure [Pa]
$P_r$	Pressure ratio ( $P_s/P_d$ )
$P_x$	Precision index
$R$	$\omega/\omega_n$ . Frequency ratio
$R_i$	Radial interference between rotor and seal [m]
$R_j$	Rotor radius [m]
$T_d$	Drag torque [N-m]
$U$	Experimental uncertainty
$X, Y$	Displacement direction [m]
$t$	Time [s]
$z$	Axial coordinate along shaft [m]
$\alpha$	Bristle lay angle [degrees]
$\gamma_{eq}, \gamma$	Structural loss coefficient, equivalent and brush seal
$\mu$	Brush seal dry friction coefficient
$\rho$	Shaft material density [kg/m <sup>3</sup> ]
$\psi(z)$	Shape function of cantilever beam due to a static load
$\omega$	Excitation frequency [rad/s]
$\omega_n$	$(K_{eq}/M_{eq})^{1/2}$ , system natural frequency [rad/s]
$\Omega$	Rotor speed [rad/s]



### Complex variables in frequency domain

$\bar{F}$  Complex amplitude of force [N]

$\bar{x}, \bar{y}$  Complex amplitude of displacement [m]

$Z$  Frequency domain impedance function [N/m]

### Subscripts

$eq$  Equivalent system: shaft + disk + brush seal

$f$  measurement axial location, load action

$s, d$  Seal and disk axial location

### Acronyms

$HBS$  Hybrid brush seal

$SBS$  Shoed-brush seal

## TABLE OF CONTENTS

	Page
ABSTRACT.....	iii
DEDICATION.....	iv
ACKNOWLEDGEMENTS .....	vi
NOMENCLATURE.....	vii
LIST OF FIGURES.....	xiv
LIST OF TABLES.....	xx
 CHAPTER	
I INTRODUCTION.....	1
II LITERATURE REVIEW.....	3
Advantages and Disadvantages of Labyrinth Seals .....	4
Advantages and Disadvantages of Brush Seals.....	5
Description and Experimental Investigation of a 1 <sup>st</sup> Generation Shoed- Brush Seal (SBS).....	9
Description and Experimental Investigation of a Hybrid Brush Seal (HBS) .....	11
III DESCRIPTION OF HYBRID BRUSH SEAL AND TEST FACILITY.....	14
Description of Hybrid Brush Seal .....	14
Test Rig I: Non-Rotating Test Rig Configuration.....	15
Test Rig II: Rotordynamic Test Rig Configuration.....	17
IV LEAKAGE CHARACTERISTICS OF A HBS UNDER STATIC CONDITION (NO SHAFT ROTATION) .....	20
Experimental Procedure .....	20
Experimental Results and Discussion .....	22

CHAPTER	Page
V IDENTIFICATION OF THE STATIC STRUCTURAL STIFFNESS OF A HBS AT INCREASING SUPPLY PRESSURES.....	27
Experimental Procedure .....	28
Experimental Results and Discussion .....	29
VI SINGLE PAD STIFFNESS PREDICTION MODEL AND OVERALL STIFFNESS FOR A HBS.....	34
Computational Programs.....	35
VII BREAK-AWAY TORQUE ESTIMATION FOR A HBS UNDER STATIC CONDITION FOR INCREASING SUPPLY PRESSURES.....	37
Experimental Procedure for Static Torque Measurements.....	37
Experimental Results and Discussion .....	37
VIII IDENTIFICATION OF HBS STRUCTURAL STIFFNESS AND EQUIVALENT VISCOUS DAMPING.....	39
Experimental Procedure .....	39
Parameter Identification Method.....	42
Experimental Results and Discussion .....	45
IX LEAKAGE OF A HBS UNDER DYNAMIC LOADING CONDITION.....	54
Experimental Procedure .....	54
Experimental Results and Discussion .....	54
X LEAKAGE OF A HBS AT LOW ROTOR SPEEDS.....	58
Experimental Procedure .....	58
Experimental Results and Discussion .....	59
XI POWER LOSS AND DRAG TORQUE OF A HBS AT LOW ROTOR SPEEDS.....	62
Experimental Procedure .....	62
Experimental Results and Discussion .....	63

CHAPTER	Page
XII IDENTIFICATION OF ROTORDYNAMIC FORCE COEFFICIENTS OF A HBS FOR INCREASING SUPPLY PRESSURES .....	66
Experimental Procedure .....	66
Parameter Identification Method.....	67
Experimental Results and Identified Rotordynamic Force Coefficients .....	71
XIII PREDICTIONS OF ROTORDYNAMIC FORCE COEFFICIENTS OF A HBS.....	78
XIV CONCLUSIONS AND RECOMMENDATIONS.....	84
REFERENCES.....	88
APPENDIX A STATIC STRUCTURAL STIFFNESS MEASUREMENTS .....	90
APPENDIX B PRECISION OF FLOW RATE MEASUREMENTS .....	97
APPENDIX C IDENTIFICATION OF STRUCTURAL PARAMETERS OF ROTOR ASSEMBLY (ROTORDYNAMIC TEST RIG CONFIGURATION) FROM IMPACT TESTS .....	99
Experimental Set up and Procedure .....	99
Experimental Results.....	100
Theoretical Prediction of Stiffness, Mass and Damping Coefficients of Rotor Assembly .....	103
APPENDIX D NATURAL FREQUENCY AND MODE SHAPES OF ROTOR ASSEMBLY (ROTORDYNAMIC TEST RIG CONFIGURATION).....	105
Free-Free Mode Shapes.....	105
Fixed-Free Mode Shapes.....	107
APPENDIX E UNCERTAINTY ANALYSIS .....	110
Dynamic Loading Tests .....	111
Drag Torque Estimation .....	112
Leakage Tests .....	112
APPENDIX F EVALUATION OF DISK AND SEAL WEAR .....	113

	Page
APPENDIX G CALIBRATION OF INSTRUMENTATION.....	115
Pressure Sensors .....	115
Eddy Current Sensors.....	115
Turbine Flowmeter .....	116
VITA.....	118

## LIST OF FIGURES

	Page
Figure 1 Axial and cross-sectional views of commercial brush seal .....	6
Figure 2 Close up photograph of a shoed brush seal.....	10
Figure 3 Photograph of a hybrid brush seal (close up of pad and elastic supports).....	12
Figure 4 Profile for a hybrid brush seal (not to scale).....	15
Figure 5 Cut view of non-rotating HBS test rig .....	16
Figure 6 View of the test brush seal installation and instrumentation .....	17
Figure 7 Revamped rotordynamic test rig for hybrid brush seal (HBS) .....	18
Figure 8 Cut view of HBS rotordynamic test rig .....	19
Figure 9 Detail view of disk/shaft assembly .....	19
Figure 10 Schematic drawing of test rig air supply line and instrumentation for leakage tests .....	21
Figure 11 Setup for conducting leakage measurements across hybrid brush seal .....	22
Figure 12 Air flow rate (leakage) versus supply to discharge pressure ratio ( $P_r$ ) for 1 <sup>st</sup> generation shoed brush seal and current hybrid brush seal.....	24
Figure 13 Calculated effective clearance from leakage data for 1 <sup>st</sup> generation shoed-brush seal and hybrid brush seal versus supply to discharge pressure ratios ( $P_r$ ) .....	26
Figure 14 Schematic view of set up for static load tests .....	28
Figure 15 Seal direct deflection versus applied load at pressure ratio $P_r=1.0$ for (A) non-tapping and (B) tapping testing condition. Lines for extraction of static stiffness shown.....	31
Figure 16 Direct static stiffness of hybrid brush seal for non-tapping and tapping conditions at increasing pressure ratios ( $P_r$ ) .....	32

	Page
Figure 17 Schematic view of the HBS pad for stiffness prediction .....	35
Figure 18 Visual graphical user interface for calculation of HBS static stiffness .....	36
Figure 19 Break-away torque versus supply pressure to discharge pressure ratio ( $P_r$ ) for a hybrid brush seal (HBS) under static conditions.....	38
Figure 20 Waterfall of recorded disk (seal) displacement and accelerations due to a external harmonic load (55 N). Frequency range (20 Hz- 110 Hz). Pressure ratio $P_r=1.0$ .....	41
Figure 21 Waterfall of recorded disk (seal) displacement and accelerations due to a external harmonic load (63 N). Frequency range (20 Hz- 110 Hz). Pressure ratio $P_r=1.0$ .....	42
Figure 22 Schematic view of test system and representation of equivalent mechanical system .....	43
Figure 23 Identified system dynamic stiffness versus excitation frequency. Load magnitude = 63 N, for increasing supply pressure to discharge pressure ratios ( $P_r$ ) and no shaft rotation .....	47
Figure 24 Imaginary part of the test system versus excitation frequency. Load magnitude = 63 N, for increasing supply pressure to discharge pressure ratios ( $P_r$ ) and no shaft rotation .....	48
Figure 25 Equivalent viscous damping versus excitation frequency. Load magnitude = 63 N, for increasing supply pressure to discharge pressure ratios ( $P_r$ ) and no shaft rotation .....	49
Figure 26 Direct stiffness of hybrid brush seal identified from static (tapping) and dynamic load tests versus supply pressure to discharge pressure ratio ( $P_r$ ) .....	50
Figure 27 System equivalent mass for hybrid brush seal versus supply pressure to discharge pressure ratio ( $P_r$ ) .....	50
Figure 28 Work = energy dissipated by test system versus frequency for one period of motion. Loads 63 N and 66 N on frequency range 20-110 Hz. No shaft rotation. Pressure ratio, $P_r=1.7$ .....	51

Figure 29 Work = energy dissipated by test system versus frequency for one period of motion. Loads 55 N and 63 N on frequency range 20-110 Hz. No shaft rotation. Pressure ratio , $P_r=2.4$ .....	52
Figure 30 Work = energy dissipated by test system versus frequency for one period of motion. Loads 63 N and 66 N on frequency range 20-110 Hz. No shaft rotation. Pressure ratio , $P_r=3.0$ .....	52
Figure 31 Loss factor ( $\gamma$ ) and dry friction ( $\mu$ ) coefficients for hybrid brush seal versus supply pressure to discharge pressure ratio ( $P_r$ ).....	53
Figure 32 HBS mass flow rate (leakage) versus excitation frequency (15 – 90 Hz) for increasing supply pressure to discharge pressure ratios ( $P_r$ ) no shaft rotation and upstream air temperature of 23°C.....	55
Figure 33 HBS mass flow rate (leakage) versus supply pressure to discharge pressure ratio ( $P_r$ ) for single frequency excitation loads (55N and 66N), no shaft rotation and upstream air temperature of 23°C (frequency average).....	56
Figure 34 Effective HBS clearance versus supply pressure to discharge pressure ratio ( $P_r$ ) for single frequency excitation loads (55N and 66N), no shaft rotation and upstream air temperature of 23°C.....	57
Figure 35 Photograph of rotordynamic test rig for a hybrid brush seal (HBS).....	58
Figure 36 HBS mass flow rate (leakage) versus rotational speed for increasing supply pressure to discharge pressure ratio ( $P_r$ ) at an upstream air temperature of 23°C.....	59
Figure 37 HBS mass flow rate (leakage) versus supply pressure to discharge pressure ratio ( $P_r$ ) for static condition (no rotation) and shaft speeds (600 and 1,300 RPM).....	60
Figure 38 Effective HBS clearance versus supply pressure to discharge pressure ratio ( $P_r$ ) for static condition (no rotation) and shaft speeds (600 and 1,300 RPM).....	61
Figure 39 Hybrid brush seal power loss versus rotational speed for increasing supply pressure to discharge pressure ratios ( $P_r$ ).....	64



	Page
Figure 40 Hybrid brush seal drag torque versus rotational speed for increasing supply pressure to discharge pressure ratios ( $P_r$ ).....	65
Figure 41 Reference coordinate system for rotating tests with periodic external loading .....	67
Figure 42 Waterfalls of rotor displacements (X,Y) resulting from a periodic excitation load (22 N). Excitation frequency range of 20-90 Hz, $P_r = 1.7$ and rotor speed: 600 rpm (10 Hz).....	68
Figure 43 Structural rotor model with location of HBS.....	69
Figure 44 Identified system rotordynamic stiffness versus frequency. Load magnitude = 22 N, for increasing supply pressure to discharge pressure ratios ( $P_r$ ) and rotor speeds .....	73
Figure 45 Imaginary part of system impedance versus excitation frequency. Load magnitude = 22 N, for increasing supply pressure to discharge pressure ratios ( $P_r$ ) and rotor speeds .....	74
Figure 46 Test data and identified equivalent viscous damping for increasing rotor speeds ( 600 and 1200 rpm) and increasing pressure ratios ( $P_r = 1.7$ and 2.4) .....	75
Figure 47 Average cross-coupled stiffness ( $K_{xy}$ ) for increasing rotor speeds (600 and 1,200 rpm) and increasing supply to discharge pressure ratios, $P_r$ .....	77
Figure 48 Schematic view and reference coordinate of multiple pad seal [19] .....	79
Figure 49 Visual graphical user interface for calculation of rotordynamic force coefficients [19] .....	80
Figure 50 Predicted non-synchronous HBS stiffness coefficients versus excitation frequency at two supply to discharge pressure ratios, $P_r = 1.7$ and 2.4. Rotor speed: 600 rpm (10Hz) and 1200 rpm (20Hz).....	81
Figure 51 Predicted HBS viscous damping coefficients versus excitation frequency. Rotor speeds: 600 (10Hz) and 1,200 rpm (20Hz) and supply to discharge pressure ratio, $P_r = 1.7$ and 2.4.....	83
Figure A1 Seal direct deflection versus applied load at pressure ratio $P_r=1.3$ for (A) tapping and (B) non-tapping testing conditions .....	91

	Page
Figure A2 Seal direct deflection versus applied load at pressure ratio $P_r=1.7$ for (A) tapping and (B) non-tapping testing conditions .....	92
Figure A3 Seal direct deflection versus applied load at pressure ratio $P_r=2.0$ for (A) tapping and (B) non-tapping testing conditions .....	93
Figure A4 Seal direct deflection versus applied load at pressure ratio $P_r=2.4$ for (A) tapping and (B) non-tapping testing conditions .....	94
Figure A5 Seal direct deflection versus applied load at pressure ratio $P_r=2.7$ for (A) tapping and (B) non-tapping testing conditions .....	95
Figure A6 Seal direct deflection versus applied load at pressure ratio $P_r=3.0$ for (A) tapping and (B) non-tapping testing conditions .....	96
Figure C1 Test schematic and instrumentation for structural parameter identification of HBS rotor assembly via impact load tests.....	99
Figure C2 Disk and shaft prior to assembly .....	100
Figure C3 Impact and displacement time traces for HBS rotor assembly .....	101
Figure C4 Transfer function and model fit for rotor assembly uncoupled and coupled to drive motor (Range 0-80Hz).....	102
Figure C5 Coherence from an average of 5 impacts for rotor assembly uncoupled and coupled to drive motor .....	103
Figure D1 First free-free mode shape for rotor assembly, measurements and predictions.....	106
Figure D2 Second free-free mode shape for rotor assembly, measurements and predictions.....	106
Figure D3 Third free-free mode shape for rotor assembly, measurements and predictions.....	107
Figure D4 First fixed-free mode shape for rotor assembly, measurements and predictions.....	108

	Page
Figure D5 Second fixed-free mode shape for rotor assembly, measurements and predictions.....	109
Figure F1 Surface profile of disk along its axial span. Estimation of wear after 10 hours of operation (tests with shaft rotation).....	113
Figure F2 Close up photograph of disk and HBS for wear assessment after tests with shaft rotation.....	114
Figure G1 Output voltage versus applied pressure using a dead weight tester.....	115
Figure G2 Output voltage of eddy current sensor versus measured displacement. Calibration curve.....	116
Figure G3 Volumetric flow rate versus output frequency (turbine flowmeter). Data provided from manufacturer. (Upstream pressure 100 psi).....	117

## LIST OF TABLES

	Page
Table 1 Dimensions and material properties of test hybrid brush seal .....	15
Table 2 Flow conditions for HBS leakage measurements .....	22
Table 3 Leakage rates for hybrid brush seal.....	23
Table 4 Static stiffness for shaft-disk assembly, experimental and theoretical (non rotating test rig configuration) .....	29
Table 5 System static stiffness and hybrid brush seal direct stiffness for increasing pressure ratios ( $P_r$ ). Non-tapping and tapping testing condition .....	33
Table 6 Flow conditions for dynamic load tests on a hybrid brush seal .....	40
Table 7 Identified test system equivalent parameters from dynamic load tests (Load 66 N & 63 N, 20 Hz to 110 Hz) for increasing pressure ratios ( $P_r$ ). Non-rotating test rig configuration .....	46
Table 8 Identified hybrid brush seal (HBS) parameters from dynamic load tests (Load 66 N & 63 N, 20 Hz to 110 Hz) for increasing pressure ratios ( $P_r$ ). Non-rotating test rig configuration .....	46
Table 9 Calculated natural frequencies (Forward and Backward) for test rotor with HBS in place (*) .....	69
Table 10 Identified test system direct force coefficients from rotordynamic tests (Load 22 N, 20 Hz to 80 Hz, rotating test rig configuration) for increasing pressure ratios ( $P_r$ ).....	72
Table 11 Identified test system cross-coupled force coefficients from rotordynamic tests (Load 22 N, 20 Hz to 80 Hz, rotating test rig configuration) for increasing pressure ratios ( $P_r$ ).....	76
Table C1 Identified parameters from impact tests exerted on rotor assembly (no HBS in place). Uncoupled and coupled to drive motor on rotordynamic test rig configuration.....	102

	Page
Table C2 Predicted structural parameters of rotor assembly .....	104
Table D1 Natural Frequencies for rotor assembly, measurements and predictions.....	105
Table D2 Natural Frequencies for rotor assembly, measurements and predictions.....	107
Table G1 Eddy current sensors gain estimated from calibration tests. ....	115

# CHAPTER I

## INTRODUCTION

Labyrinth seals are the most commonly used sealing configuration in turbomachinery applications. However, their sealing effectiveness is associated with maintaining very tight radial clearances. Operational conditions such as thermal expansion and rotor radial displacement produce teeth wear increasing the operating clearance, thus also increasing secondary leakage and potential for rotordynamic instability [1,2,3].

Conventional brush seals (a type of contacting seal) offer an improved sealing capability over labyrinth seals. Brush seals occupy less axial space and are able to better accommodate radial rotor excursions without significantly affecting its sealing performance. However, excessive bristle tip wear, rotor surface wear, and localized heat generation are well known issues in conventional brush seals [4,5]. Additionally, due to their construction, conventional brush seals are limited to relatively low pressure differential applications and only allow shaft rotation in one direction.

Hybrid brush seals (HBS) offer a better leakage control in turbomachinery without the major drawbacks of labyrinth and conventional brush seals [6]. The HBS innovative design resolves known brush seal reliability issues, while allowing for bi-directional rotation. Replacing a multiple-teeth labyrinth seal with a HBS effectively controls secondary leakage and allows rotors to become shorter and lighter. In addition, due to their low radial stiffness, hybrid brush seals can better accommodate rotor radial excursions without affecting their sealing capability. Under certain circumstances, a HBS may also act as an effective vibration damper [6].

Current and future operational conditions in high performance turbomachinery, i.e. increasing pressure differentials, operating temperatures and rotational speeds demand effective clearance control to reduce secondary leakage and consequently improve power delivery. Incorporating HBSs in turbomachines will reduce leakage and power losses with savings in fuel consumption, operation and maintenance costs, and increased engine reliability [4].

The main objective of this work is to quantify the leakage, power loss and structural parameters of a hybrid brush seal as a function of various operating conditions (i.e., supply pressure, load magnitude and rotor speeds). Characterization of sealing performance is paramount for their successful application in high-performance turbomachinery.

## CHAPTER II

### LITERATURE REVIEW

Parasitic secondary flow (seal leakage) in gas turbines represents a considerable loss in power delivery with an increase in specific fuel consumption [4]. A reduction in secondary flow in high performance turbomachinery gives an increased fuel efficiency and enhanced performance, in particular under strenuous operating conditions (i.e., high pressure differentials, operating temperatures, and rotor speeds). Under these conditions, it is imperative to outfit the rotating machinery with state-of-the-art sealing components to improve its performance.

This review discusses literature related to labyrinth and conventional brush seals commonly used in turbomachinery. The review focuses primarily on the well known advantages and disadvantages of both types of dynamic seals. Additionally, work performed on the 1<sup>st</sup> generation multiple shoed-brush seal (SBS) and its successor the hybrid brush seal (HBS) is also discussed.

Chupp et al. [7] present a comprehensive review of seals in steam and gas turbines, discuss the different sealing environments in a turbomachinery, and highlight the benefits resulting from proper clearance control. In a high pressure turbine, a 0.0254 mm (0.001 in) blade tip clearance increase renders up to a 1 % rise in specific fuel consumption and exhaust gas temperature. Turbomachinery designers must consider operational conditions (i.e., pressure differentials, temperatures and rotor speeds) and material characteristics (thermal and structural behavior) for a specific application. A minimal change in any of these factors affects overall engine efficiency and dynamic behavior. For static, dynamic and advanced design seals, Ref. [7] details current materials and manufacturing process. Seal geometry, typical applications and locations within a turbomachine, and seal life are also thoroughly described.



## **Advantages and Disadvantages of Labyrinth Seals**

Review Ref. [7] details well known advantages and disadvantages of labyrinth seals and brush seals of common use in non-contacting dynamic sealing applications. Labyrinth seals comprise of circumferential knife-edge teeth to make a tortuous axial path that restricts gas flow from a high pressure region into a low pressure region. Labyrinth seals provide satisfactory sealing at a low manufacturing cost; albeit their leakage control effectiveness is highly dependent on maintaining, at all times, a tight radial clearance between the seal and the rotor. Transient large amplitude rotor excursions and partial rubbing of the rotor against the labyrinth teeth lead to an increase in leakage and a reduction in engine efficiency. Importantly enough, labyrinth seals are also prone to develop cross-coupled (follower) forces with the potential of inducing rotordynamic instability [1,2,3].

In 1980, Benckert and Wachter [2] discuss the effect of pressure differential, rotor speed, entry flow conditions, and seal geometry on the rotordynamic stability of labyrinth seals. Tests results show that the inlet swirl velocity of a gas entering a labyrinth seal or developed within its cavities (due to shaft rotation) generates destabilizing forces (i.e. cross-coupled stiffness), therefore reducing the effective damping of the seal. As a corrective measure “swirl brakes” are implemented upstream of the labyrinth seal to reduce, and in some cases even eliminates the preswirl entering a labyrinth seal.

Childs and Vance [3] discuss the advantages and disadvantages of annular pressure gas seals on the dynamic behavior of compressors and turbines. Test measurements demonstrate that the origin of the destabilizing forces in interlocking and “see-through” labyrinths is the fluid rotation within the seal. The fluid is either pre-rotated as it approaches the seal or the swirl is induced by the rotor. In either case, measurements show that the cross-coupled stiffness (responsible for rotordynamic instability) increases due to the circumferential flow developed within the labyrinth cavities.

Xi and Rhode [1] present a study on the degrading effects of damaged labyrinth seal teeth on impeller eye seals in compressors. A CFD-perturbation model predicts the

rotordynamic coefficients acting on a rotor running at 6,000 rpm, with air as the working fluid at an upstream pressure of 13.77 bar and operating at a pressure ratio of 0.71. Predicted rotordynamic coefficients for a labyrinth seal in pristine condition, with a radial clearance of 0.254 mm, show good correlation when compared with measurements obtained by Soto and Childs [8] for a long, 20-teeth on stator labyrinth seal. Predicted leakage rate increases linearly as the seal clearances widens (i.e., ~320% for a 0.762 mm radial clearance). The largest clearance simulates the enlarged gap between the seal and rotor generated by radial impacts of the rotor against the seal teeth. Additionally, the swirl velocity through the labyrinth seal increases with increasing leakage rates; resulting in a net reduction of the *effective* damping of the seal, and the potential for rotordynamic instabilities due to aerodynamic cross-coupling forces.

### **Advantages and Disadvantages of Brush Seals**

Over the past 20 years brush seals have gained popularity over traditional labyrinth seals as an effective sealing component. Initially implemented in aerospace applications, brush seals are now an essential component in power generation turbomachinery, offering significant efficiency improvement and reduced fuel consumption [9]. Commercially available brush seals consist of packed metallic bristles<sup>1</sup> of fine diameter clamped between a front plate on the upstream (high pressure region) and a backing plate on the downstream (low pressure region), as shown in Figure 1. Bristles are slanted at an angle (i.e. lay angle) in the direction of rotor spinning. The bristles bend rather than buckle during transient rotor radial excursions.

---

<sup>1</sup> Nowadays there are also brush seals with polymer bristles; their usage is limited by the operating temperature.

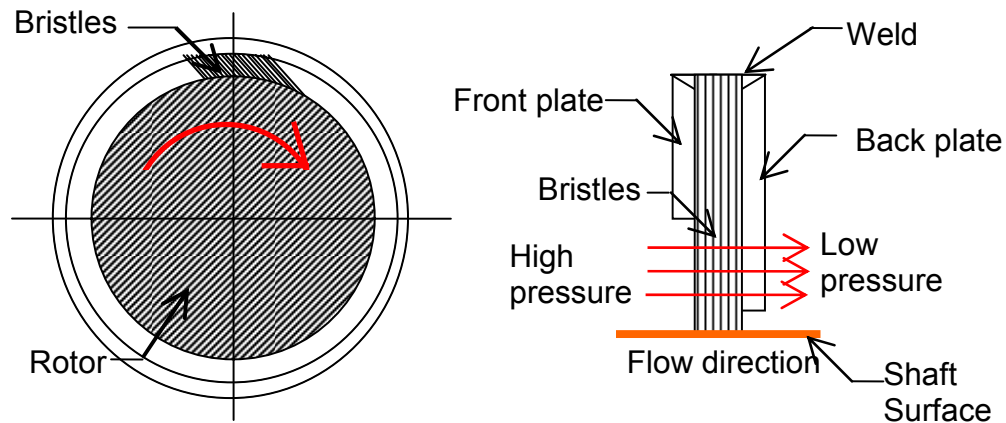


**Figure 1 Axial and cross-sectional views of commercial brush seal**

In 1988, Ferguson [10] describes the brush seal as the first simple and practical sealing alternative for labyrinth seals in gas turbines. Test rig and back to back engine tests performed for a range of pressure ratios on various labyrinth seals and a brush seal demonstrate the improved sealing performance of a brush seal over labyrinth seals. Results for a brush seal show a leakage reduction of approximately 10% when compared to a labyrinth seal having a 0.70 mm radial clearance. Heat generated by a brush seal during rotational tests at a pressure ratio of 1.3 was approximately 25% of that generated by a five-teeth labyrinth seal. Additional test results show that brush seal leakage decreases with increasing rotor speed, approximately a 20% overall leakage reduction from 0 to 30 krpm.

Chupp and Dowler [9] present experimental results from research characterizing the performance of brush seals in gas turbine engines. The results of interest are leakage improvements, seal wear, and costs of replacing labyrinth seal with brush seals. Performance test results for two brush seal configurations, i.e. 0.127 mm and 0.0254 mm (0.005 and 0.001 inches) radial interference with test rotor at 30,000 rpm and 260 °C (500 °F) air temperature show a considerably lower leakage (i.e. 4 to 7 times less), when compared to a reference labyrinth seal having a radial clearance of 0.152 mm (0.006 in.) under identical operational and flow conditions. Measurements also reveal that multiple brush seals in series allow for higher pressure drops, while maintaining reduced leakage.

Furthermore, reduction in parasitic leakage represents lower fuel costs and enhanced engine performance.

Reliable leakage prediction across a brush seal is essential to readily evaluate seal design and performance after manufacturing and previous to its installation in a gas turbine engine environment. Unfortunately, to date due to the structural complexity of brush seals; and also due to operating conditions such as external pressurization and rotor speed, it is difficult to predict brush seal leakage with high confidence. Despite these difficulties, research efforts are aimed to develop simple brush seal leakage predictive model for actual engine operational conditions.

In 1996, Chupp and Holle [11] present a semi-empirical model predicting leakage flow in a conventional brush seal. The parameters of importance are the effective brush thickness parameter ( $B$ ), the reduced effective thickness ( $B_o$ ) for a no flow condition, and the flow factor ( $\phi$ ).  $B$  and  $B_o$ , in conjunction with other geometric parameters, relate the compactness of the bristle bed at different flow conditions. The model neglects the radial flow component, since pressure drop across the seal induces mainly axial flow. Predictions correlate well with leakage measurements presented by Basu *et al.* [12] for a conventional brush seal.

Chew and Hogg [13] presents a brush seal leakage model which treats the bristle pack as a porous medium. The model defines flow resistance coefficients for the inertial and viscous contributions of gas flow across the bristle bed. The model represents a steady-one dimensional axial flow of an isothermal ideal gas. Despite the differences in operating conditions (i.e., variations in pressures downstream and upstream of the seal) during testing, leakage predictions generated by the one-dimensional form of the model correlate very well with experimental measurements presented in [14,15] for brush seals with interference fits only. The one-dimensional form of the model applies only for brush seal with interference fits to the rotor, and it is not appropriate for brush seal configurations operating with clearance between bristle tips and rotor. The flow regime becomes highly two dimensional; i.e. a combination of flow through the bristle bed and

the clearance. Additionally, the authors describe a multi-dimensional form of the porosity model to account for different flow regimes; such as clearance flows.

Over recent years, investigations aiming to characterize brush seal leakage and structural behavior have been undertaken to improve brush seal technology and to overcome known issues such as excessive leakage rates and rotordynamic instability faced by steam and gas turbine engines. Carlile *et al.* [14] investigate the leakage performance of a brush seal with different gases, i.e., helium, air and carbon dioxide, under static and at low rotor speeds for various brush seal/rotor interference configurations. Proctor and Delgado [4] compare test leakage and power loss measurements for a brush seal and a finger seal. Both seals show improved sealing performance and a reduced power loss compared to a labyrinth seal.

Conner and Childs [16] present measurements of rotordynamic coefficients for a four-stage brush seal operating at increasing pressure ratios, shaft speed, fluid pre-rotation and seal spacing. Cross-coupled stiffnesses (i.e. source of destabilizing forces in annular gas seals) identified from measurements are very low and generally negative; thus having a stabilizing effect, opposite to that in labyrinth seals. Direct damping coefficients increase marginally as a function of rotor speed. These test results indicate the apparent benefits of implementing brush seals instead of labyrinth seals in turbomachinery applications.

Current state of the art for conventional brush seals limits them to low pressure differential applications. At high pressure differentials, bristles tend to deflect in the flow direction and occasionally radially inward (i.e. blowdown effect) due to the low axial stiffness of the bristle matrix. As a result, in many applications, brush seals are installed or retrofitted in parallel with labyrinth seals. Basu *et al.* [12] identifies pressure induced bristle “hysteresis” and “stiffening” as two of the major drawbacks of brush seals. Bristle hysteresis prevents displaced bristles from returning to their original position after a rotor radial excursion, increasing the seal leakage since the flow area increases. Furthermore, conventional brush seals are prone to persistent wear due to intermittent

contact between the bristles and rotor surface, inducing on most occasions grave local thermal distortions.

Dogu and Askit [5] investigate the temperature distribution of a brush seal resulting from the frictional heat generated at the bristle tips as they contact a rotating shaft. Predictions show maximum heat generation at the contact location between the bristle tips and rotor. The temperature diminishes along the length of a bristle. This condition not only accelerates the oxidation rates of the bristle matrix, but in extreme cases, melts the bristle tips; thus degrading the overall seal and rotor mechanical integrity. For these reasons, on many occasions costly protective coatings are applied on the rotor of machines using brush seals; to prevent the deterioration of the rotor surface. In addition, conventional brush seals-due to their slanted bristles-orientation are unable to accommodate rotational motions in both directions, an issue for certain aircraft turbine applications.

### **Description and Experimental Investigation of a 1<sup>st</sup> Generation Shoed-Brush Seal (SBS)**

Justak [17] introduced the 1<sup>st</sup> generation of a multiple shoed-brush seal (SBS) to resolve poor reliability of conventional brush seals associated with excessive bristle tip wear and heat generation resulting from the intermittent contact between the rotor and bristles. In addition, shoed-brush seals allow for shaft rotation in both directions. This seal innovative design, shown in Figure 2, incorporates a series of arcuate pads spot-welded to the bristles free ends (two spots per pad). Prior to shaft rotation the pads or shoes are in contact and pressing against the rotor surface. As the rotor spins, the shoes lift-off due to the generation of a hydrodynamic gas film pressure that reduces or eliminates wear during steady operation. The shoed-brush seal, as well as conventional brush seals, are also limited to low pressure differentials due to the low axial stiffness of the bristle pack tilting the pads axially at a high pressure differential operation.

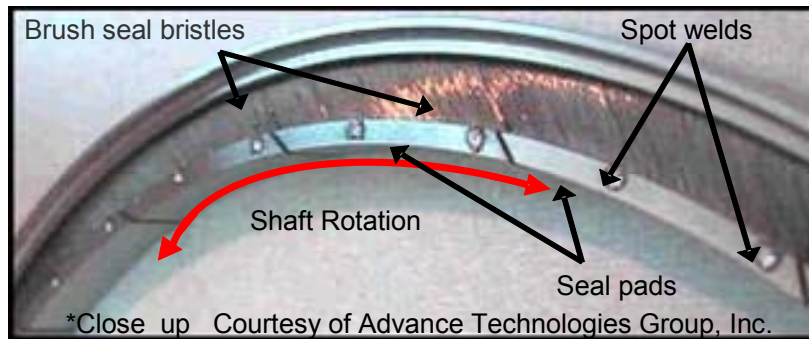


**Figure 2 Close up photograph of a shoed brush seal**

Delgado and San Andrés [18] present measurements to determine the static structural stiffness and damping coefficients of a large diameter, 279 mm, 20-shoe brush seal. Static load pull tests and recorded seal deflections (along direction of load) allow the measurement of the seal structural stiffness. Two test procedures, tapping and non-tapping of the test seal were implemented for the identification procedure. For the tapping condition, the seal holder is perturbed to break the stick-slip (dry friction) between the bristles in the test seal as the shaft is gradually loaded. No external perturbation is introduced for the non-tapping case. A model that considers the bristles as thin beams renders a simple formula for the estimation of the whole shoed-brush seal stiffness. Static stiffness measurements validate the simple model predictions within  $\sim 3.0\%$ . Impact tests to identify the dynamic structural stiffness of the seal and its effective viscous damping coefficient, evidence a non-linear behavior, making the viscous damping model not suitable for damping response predictions at low frequencies ( $\sim 50$  Hz).

Delgado and San Andrés [19] introduce a comprehensive analysis for prediction of rotordynamic force coefficients of a 20 shoe-brush seal, 279 mm in diameter, for rotor speeds varying from 5krpm to 20krpm. The physical model couples the gas film forces generated in the thin gap between the rotor and a shoe and the structural characteristics (stiffness and damping) from the bristle pack underneath. Predictions indicate that rotordynamic force coefficients are independent of the operating gas film clearance and pressure differential across the seal. Predicted direct seal stiffnesses at null rotor speed correlate well with the structural seal stiffness ( $\sim 22.5$  kN/m) measured in [18], and

decreasing rapidly with increasing rotor speed. Seal cross-coupled stiffnesses are at least one order of magnitude smaller than the direct stiffnesses. Hysteretic (structural) damping, expressed in terms of a structural loss factor, accounts for most of the seal damping.

Delgado and San Andrés [20] detail a sound identification method to extract the structural stiffness and damping coefficients of a 20 shoe-brush seal (SBS), 153 mm in diameter, using single frequency dynamic loads in a controlled motion test rig (without shaft rotation) and no external pressurization. The structural seal stiffness identified (143 kN/m) is ~12% higher than the measured static stiffness (125 kN/m) for this shoed-brush seal geometry. The brush seal energy dissipation mechanism is modeled as a combination of structural damping and Coulomb damping mechanisms, and represented by a loss factor ( $\gamma$ ) and a dry friction coefficient ( $\mu$ ), respectively. Analysis of test results show the method for identification of brush seal structural coefficients is only valid above a threshold load (i.e. macro-slip motion regime), where seal deflections are dependent on the applied load, and the friction force is nearly constant in amplitude. Seal motion below this load show super-harmonic frequency components (3X and 5X) evidencing the presence of dry-friction arising from the bristle-to-bristle and bristle-to-backplate interaction.

### **Description and Experimental Investigation of a Hybrid Brush Seal (HBS)**

Justak introduces the next generation of a shoed brush seal, the hybrid brush seal (HBS) [21]. As shown in Figure 3, in a hybrid brush seal the arcuate pads are connected to the seal casing through EDM slender spring lever elements. The novel construction eliminates reliability issues associated to the original used spot-welded connections. The thin EDM spring lever connections have a low radial stiffness and high axial stiffness; thus eliminating bristle and rotor wear, and at the same time, preventing pad pitching motions caused by high pressure differentials across the seal. The bristles are located in series with the EDM-webs (second stage); thus now acting as a secondary seal to the gas film riding pad element. The bristle tips are not welded to the pads, but rather contacting the back part of the pads.





**Figure 3 Photograph of a hybrid brush seal (close up of pad and elastic supports)**

Justak and Crudgington [6] evaluate the performance of a hybrid brush seal in terms of measured leakage under static and rotational speed conditions (maximum 15,000 rpm). The seal is tested in both an ambient and a high temperature test rigs, at pressure differentials ranging from 0 to 3 bar, to simulate engine conditions. Performance of the seal is characterized in terms of an semi-empirical effective clearance parameter ( $C_E$ ) derived from the mass flow rate across the seal, inlet pressure, and temperature. An increase in effective clearance as a function of increasing pressure represents a minimal increase in leakage across the seal. A gradual temperature decrease at the rotor/seal interface as the pressure across the seal increases evidences the presence of a gas film separating the seal pads and rotor. In addition, test results show that power requirements to conduct the rotational tests remained approximately constant under pressurized conditions (i.e. for the differential pressure range tested), indicate that no evident increase in power loss was incurred as a result of operating a hybrid brush seal at various pressurized conditions.

San Andrés et al. [22] present measurements of power loss and leakage in a hybrid brush seal (HBS) for increasing pressure differentials and over a range of rotor speeds. Power loss and drag torque measured at low rotor speeds ( $< 11$  m/s at 1,300 rpm) decrease as the pressure differential across the seal increases. Maximum power losses ( $\sim 350$  W) occur without external air pressurization (rubbing between pads and rotor). Power losses decrease by approximately 90% over the test speed range (400 to 1300 rpm) as the seal is pressurized, evidencing the generation of a hydrodynamic gas film separating the seal pads from the rotor surface. A low constant temperature ( $\sim 25^\circ\text{C}$ )

at the rotor/seal interface during rotating tests confirms the presence of a gas film; thus eliminating rotor and seal wear. Additionally, leakage measurements at room temperature (25°C) show an improved sealing ability with a leakage reduction of about 36%, when compared to a first generation shoed-brush seal (SBS) [23]. This sealing improvement is associated to an increase in the pads' support axial stiffness, provided by the EDM-webs connecting the shoes to the seal casing, and which effectively prevents pads' pitching motions caused by pressure differentials across the seal.

## CHAPTER III

### DESCRIPTION OF HYBRID BRUSH SEAL AND TEST FACILITY

This chapter describes the test hybrid brush seal (HBS), and the test facilities (non-rotating and rotating shaft configurations) used in the tests. The seal manufacturer provided seal dimensions and tolerances. These dimensions were verified prior to initiating the series of static and dynamic load tests. Static and dynamic shaker load (without shaft rotation) tests are performed in a non-rotating test rig configuration (controlling relative motion of the shaft). Subsequently, rotordynamic tests are performed in a revamped test rig that allows for shaft rotation. Details of the test rigs follow.

#### Description of Hybrid Brush Seal

The hybrid brush seal (HBS), a 2<sup>nd</sup> generation shoed-brush seal, integrates arcuate pads connected directly to the seal casing through EDM-webs, as shown in Figure 3. The novel construction eliminates reliability issues associated with the originally used spot-welded connections. More importantly, the thin beam connections (webs) provide a high axial stiffness while maintaining a low radial stiffness; thus reducing pad and rotor wear and secondary flow (leakage). This property eliminates pad pitching motions caused by the large pressure differential imposed across the seal.

In contrast to conventional brush seals, the HBS design accommodates shaft rotation in both directions, and it also eliminates bristle tip wear, pad/rotor contact and thermal distortions by means of a hydrodynamic gas film lifting the pads as the rotor spins. Figure 4 show a schematic profile view of the HBS. Once the HBS is pressurized, the pad design allows for a hydrostatic lift off effect, prior to shaft rotation. It is thought that this effect is further enhanced by shaft rotation. Table 1 details the dimensions and material properties for the test hybrid brush seal.

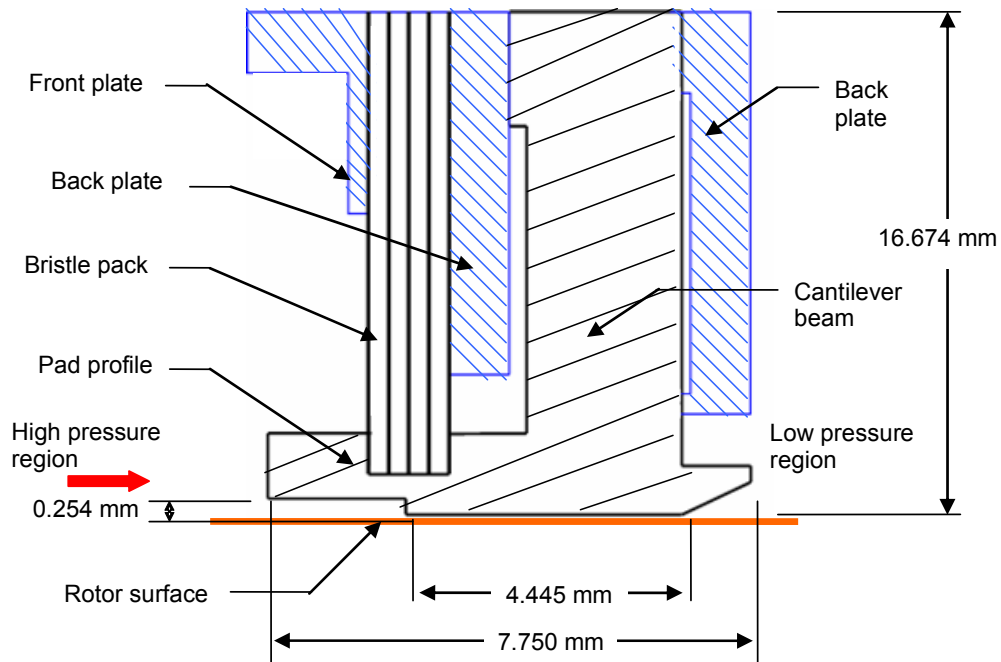


**Figure 4 Profile for a hybrid brush seal (not to scale)**

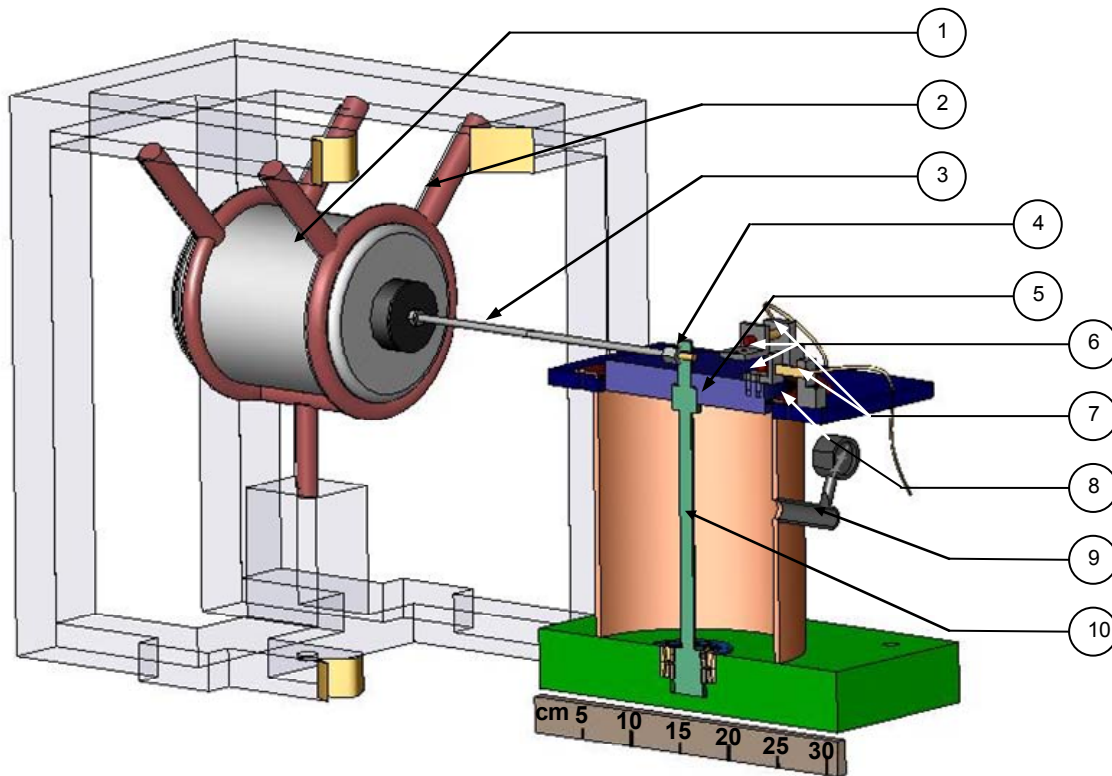
**Table 1 Dimensions and material properties of test hybrid brush seal**

Physical Properties	SI unit	English Unit
Rotor diameter, $D_j$	167.1 mm	6.580 in
Brush seal (pads) inner diameter, $D_{s_i}$	166.4 mm	6.550 in
Brush seal (retainer) outer diameter, $D_o$	183.1 mm	7.210 in
Brush seal width, $B_w$	8.53 mm	0.336 in
Radial Interference between rotor and seal, $R_i$	0.381 mm	0.015 in
Number of pads	20	
Width of pads	7.23 mm	0.331 in
Bristle lay angle, $\alpha$	45 deg.	-
Bristle modulus of elasticity, $E$	$22.48 \times 10^5$ bar	$32.6 \times 10^6$ psi
Bristle density (circumference)	850 bristle/cm	2300 bristle/in

### Test Rig I: Non-Rotating Test Rig Configuration

Figure 5 depicts a cut view of the non-rotating HBS test rig, consisting of an aluminum disk (167.1 mm in diameter and 25.4 mm in length) mounted on a long and slender steel shaft located inside a cylindrical steel vessel. One end of the shaft is affixed to the bottom of the vessel via two rolling elements bearings. The test brush seal (166.4

mm in diameter at the pads circumference) is secured atop the vessel with a retainer ring. The seal assembly nominal radial interference fit with the disk is 0.38 mm (0.015 in). The air supply line is instrumented with a pressure gauge, a turbine flowmeter, a static pressure transducer, and thermocouples.



1	Electromagnetic Shaker	6	Accelerometers
2	Soft supports (rubber cords)	7	Targets and displacement sensors
3	Stinger	8	Shoed brush seal
4	Load Cell	9	Air inlet
5	Solid Disk	10	Cantilever shaft

**Figure 5 Cut view of non-rotating HBS test rig**

Figure 6 shows a close-up view of the test brush seal and disk depicting the instrumentation for dynamic load testing. Two eddy current sensors, 90° apart, are installed atop the vessel and facing small brackets mounted on the top disk. The sensors record the disk displacements along two orthogonal directions. Two piezoelectric accelerometers, attached to the brackets on the disk, record the disk acceleration along

two orthogonal directions on the horizontal plane. A slender rod (stinger) connects the end of the shaft to an electromagnetic shaker. A piezoelectric load cell is fastened at one end of the stinger.

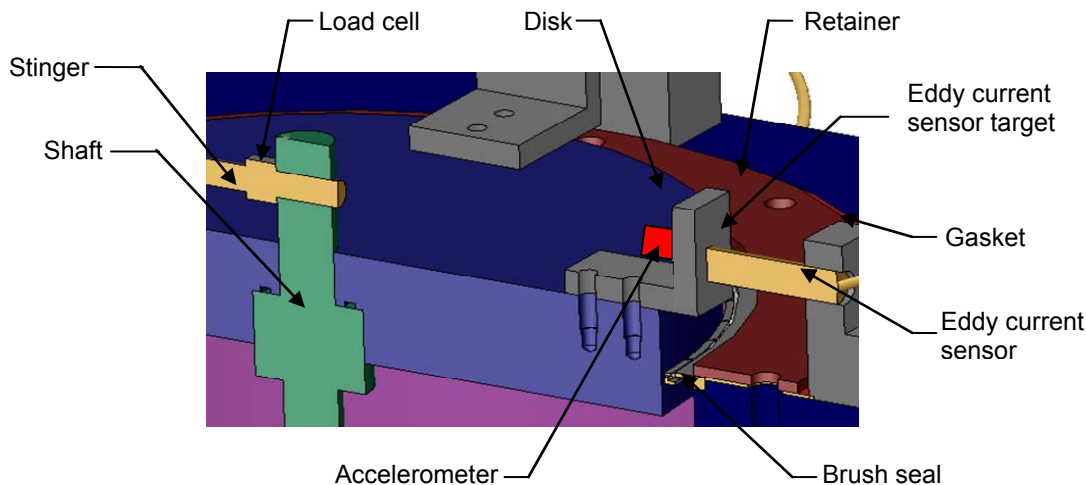
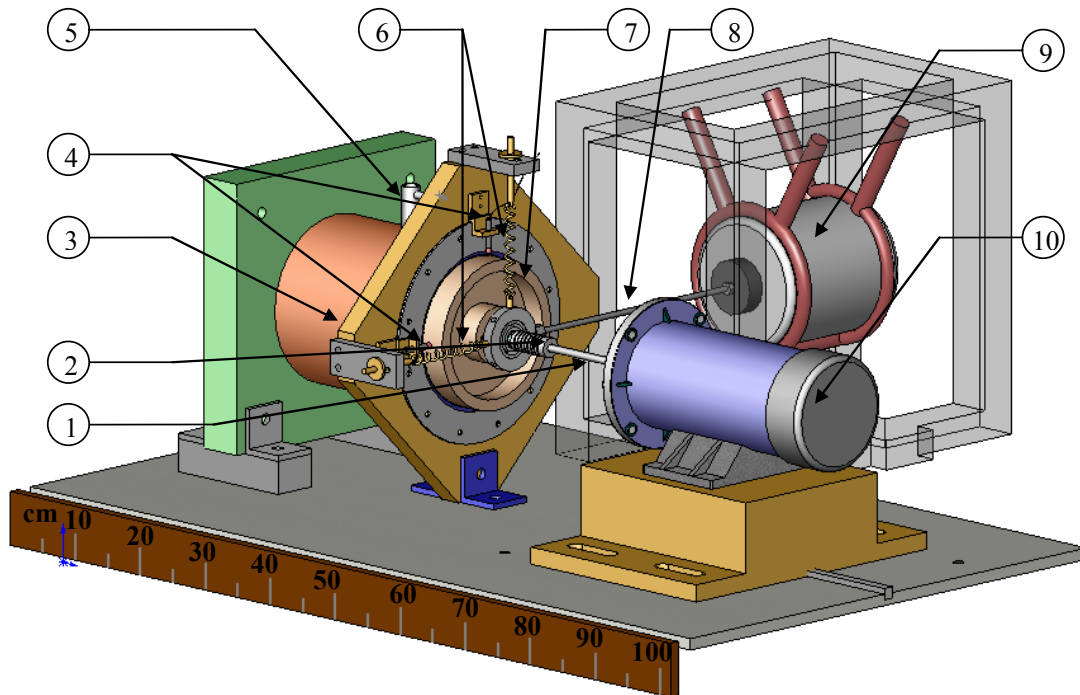


**Figure 6 View of the test brush seal installation and instrumentation**

### **Test Rig II: Rotordynamic Test Rig Configuration**

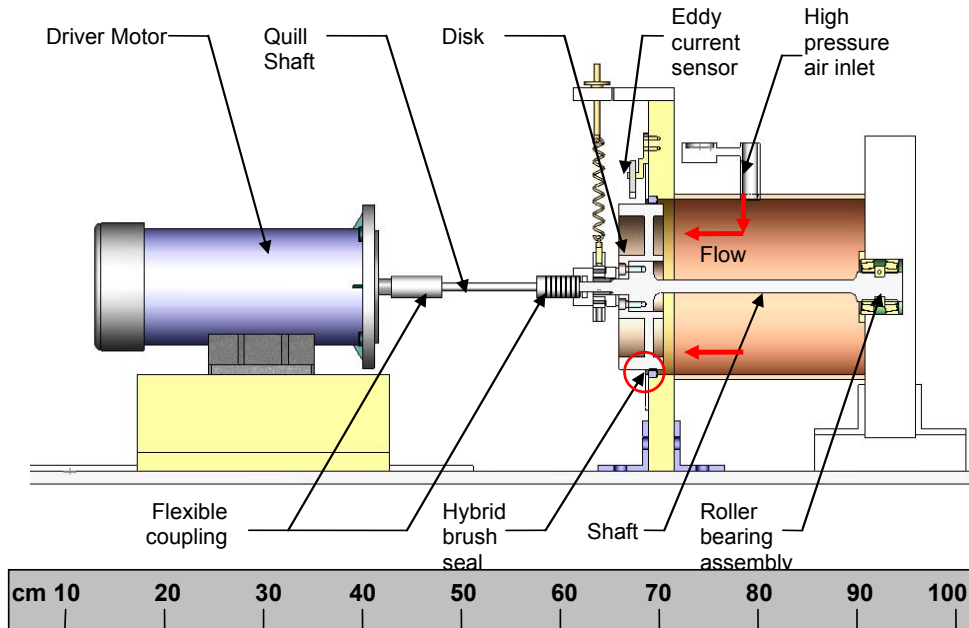
Figure 7 depicts the rotordynamic test rig assembly constructed for the project. This test rig is a revamped version of the original (controlled motion) test rig described above. In the current arrangement, the steel vessel is placed in horizontal position with the steel shaft and disk secured in a similar manner as for the non-rotating test rig. The steel shaft is connected to the base of the steel vessel via two taper roller bearings and the free end holds a steel disk. A DC motor 745 Watts (1 HP) drives the overhang disk/shaft assembly at the shaft free end through a flexible coupling. Two soft coil springs located at the drive end of the shaft, in the vertical and horizontal directions, allow centering the rotor free end with respect to the seal. The coils connect to the shaft through a ball bearing enclosed within an aluminum housing (see Fig. 8). Appendices C and D detail the characterization of natural frequencies, stiffness and mass coefficients and vibration mode shapes of the disk and shaft system alone, respectively.



1	Quill shaft	6	Supporting springs
2	Flexible coupling	7	Rotor
3	Pressurization vessel	8	Stinger
4	Eddy current sensors	9	Electromagnetic shaker
5	Supply pressure inlet	10	DC motor

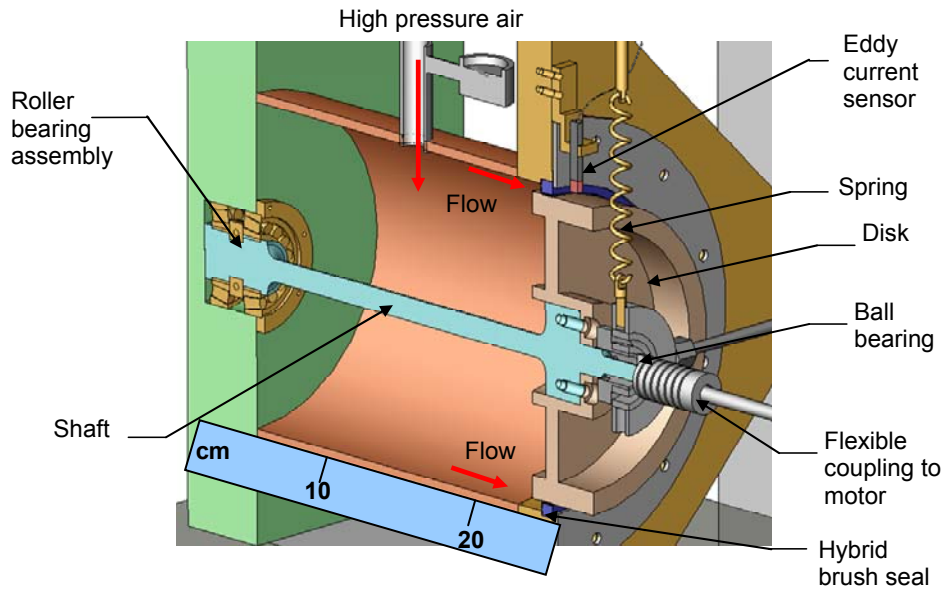
**Figure 7 Revamped rotordynamic test rig for hybrid brush seal (HBS)**

Figure 8 shows the rotordynamic test rig with a cut view of the cylindrical vessel. The drawing displays the main components of the rotordynamic test rig, as well as the location of the HBS and the inlet for high pressure air.



**Figure 8 Cut view of HBS rotordynamic test rig**

Figure 9 shows a detail view of the steel vessel and rotor/shaft assembly. The figure depicts the bearing assembly, one of the coil springs, and the eddy current sensor in the vertical direction.



**Figure 9 Detail view of disk/shaft assembly**



## CHAPTER IV

### LEAKAGE CHARACTERISTICS OF A HBS UNDER STATIC CONDITION (NO SHAFT ROTATION)

The following section presents results for leakage measured (secondary flow) through a hybrid brush seal (HBS). The test conditions are: centered position, room temperature, no rotation for increasing supply pressures ( $P_s$ ). A pressure ratio ( $P_r$ ) is defined as absolute supply pressure ( $P_s$ ) over discharge pressure ( $P_d$ ), ( $P_r = \frac{P_s}{P_d}$ ). The discharge pressure ( $P_d$ ) is atmospheric, i.e. 101 kPa (14.7 psia). A semi-empirical effective clearance parameter ( $C_E$ ) calculated using the measured HBS leakage, supply pressure and inlet air temperature allows comparing the HBS leakage to that of a labyrinth seal.  $C_E$  represents the equivalent film thickness in a “one-sharp tooth” labyrinth seal [6]. A description of the experimental procedure for measuring static leakage of the test HBS follows.

#### Experimental Procedure

Figure 10 shows a diagram of the air supply line and instrumentation for the leakage tests. The air line is instrumented with multiple pressure gauges, a turbine flowmeter, a strain gauge pressure transducer and thermocouples.

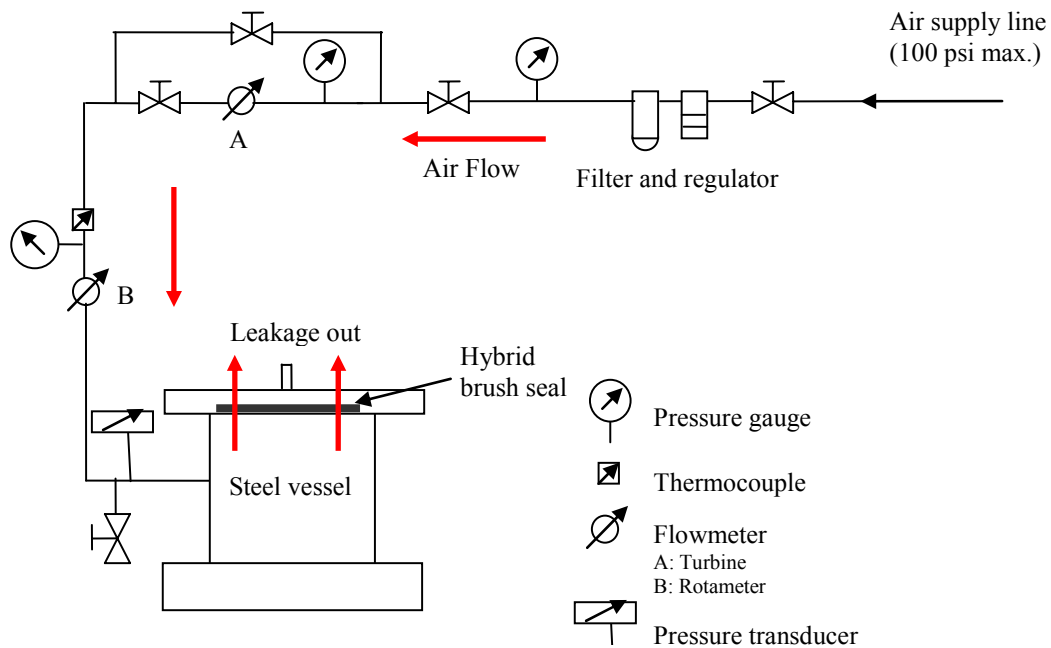


**Figure 10 Schematic drawing of test rig air supply line and instrumentation for leakage tests**

Figure 11 shows the test HBS secured atop the cylindrical vessel. The supply pressure into the cylindrical vessel,  $P_s$ , is recorded with a pressure transducer installed close to the air inlet of the steel vessel and manually controlled with a valve located downstream of the turbine-flow meter. Table 2 displays the air flow conditions for the test brush seal leakage flow measurements. Seal leakage (mass flow rate) is measured at eleven increasing pressures within the range shown in Table 2, 136 to 307 kPa (19.7 to 44.5 psia). Eight independent trials are conducted to confirm the repeatability and reliability of the measurements for each corresponding pressure.

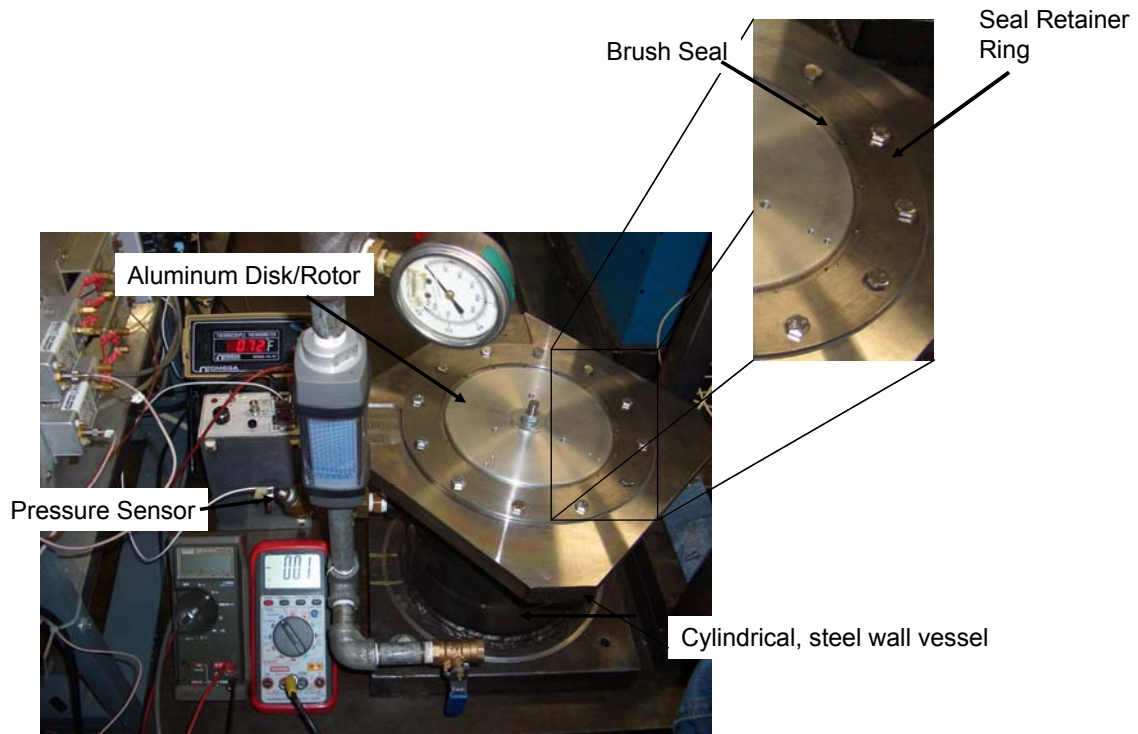


Figure 11 Setup for conducting leakage measurements across hybrid brush seal

Table 2 Flow conditions for HBS leakage measurements

<b>Fluid: air</b>	SI Unit	US Unit
Pressure Downstream (discharge ), $P_d$	101 kPa	14.54 psia
Pressure Upstream (supply), $P_s$	136 to 307 kPa	19.7 to 44.5 psia
Temperature upstream, $T_u$	69 to 71 °F	20.5 to 21.7 °C

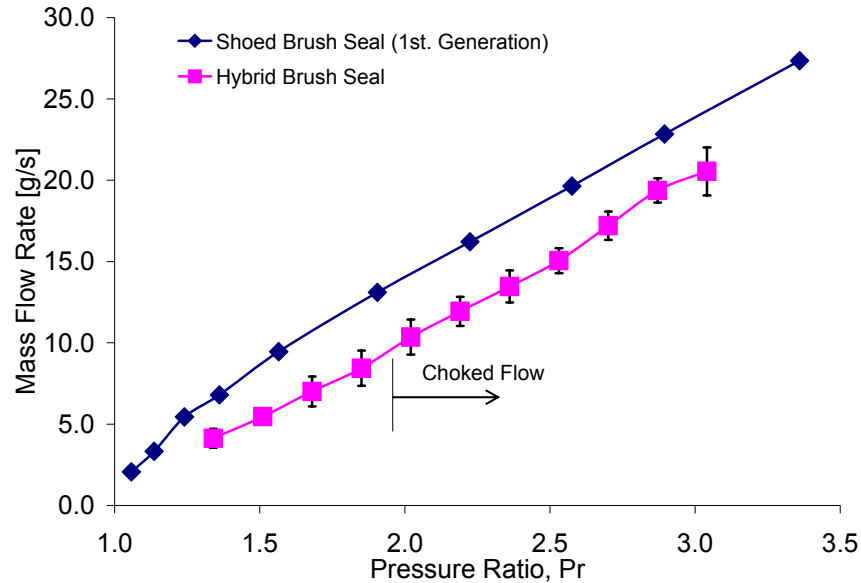
## Experimental Results and Discussion

Table 3 displays the mean (average) values of the recorded flow rate across the brush seal for the corresponding pressure ratio,  $P_r = (P_s/P_d)$ . The measurements at each pressure ratio are consistent for the eight trials with minimal variation. The figures following Table 3 compare the leakage flow rate values obtained for the currently tested brush seal and to the ones reported by San Andrés [23] for the 1<sup>st</sup> generation shoed brush seal.

**Table 3 Leakage rates for hybrid brush seal**

<b>Pressure Ratio</b>	<b>Volumetric Flow Rate</b>	<b>Mass Flow Rate</b>	
		<b>[g/s]</b>	<b>[lb/s]</b>
$P_r$ [-]	[SCFM]		
1.3	7.127	4.134	0.009
1.5	9.409	5.458	0.012
1.7	12.08	7.007	0.015
1.9	14.55	8.438	0.019
2.0	17.84	10.35	0.023
2.2	20.58	11.94	0.026
2.4	23.21	13.46	0.030
2.5	25.95	15.05	0.033
2.7	29.65	17.20	0.038
2.9	33.39	19.37	0.043
3.0	35.42	20.54	0.045

Figure 12 depicts the measured mass flow rate versus pressure ratio for the 1<sup>st</sup> generation shoed brush seal and hybrid brush seal. Recall that the SBS has an inner diameter of 162.9 mm and radial interference fit of 0.44 mm. The HBS shows a superior sealing performance over its predecessor, reducing overall leakage about 36% over the test pressure range. This sealing improvement can be associated with the current brush seal increased stiffness and the ability of the pads (shoes) to better withstand axial and twisting motions due to the pressure differential. The flow is choked for  $P_r = 2.0$  to 3.0 the, indicating that mass flow rate (leakage) increases linearly with increasing supply pressure. For the HBS data, Figure 12 includes error bars defining 95% confidence intervals.



**Figure 12 Air flow rate (leakage) versus supply to discharge pressure ratio ( $P_r$ ) for 1<sup>st</sup> generation shoed brush seal and current hybrid brush seal**

Refs. [11,13] present models to predict leakage across conventional brush seals. Additional leakage models are readily available in the technical literature and in some cases, predictions correlate well with experimental values. In addition, these models rely heavily on empirical parameters derived from experiments, often proprietary. However, limitations linked to their inability to reproduce the complex behavior of the flow as it passes through the bristle pack and adjacent structures (i.e. front and back plate) makes leakage prediction models extremely sensitive to changes in the empirical parameters used. Chew and Hogg [13] acknowledge that the flow through a bristle pack is not fully understood, and urge further study to obtain good correlations between predictions and experimental data. Recall that leakage rate across a brush seal is highly dependent on structural factors such as bristle pack density, fence height, and operating clearance, if any.

Many times, leakage models [13] for brush seals provide good correlation when compared with available test data [14]. Unfortunately, on occasions these predictive tools work only under specific restrictive factors such as: specific pressure range, temperature and rotor speeds; thus limiting their application. In addition, representing

the bristles in a brush seal with simple geometric configurations also limits the effectiveness of the model. Under these circumstances actual measurements and known physical parameters are required. According to a brush seal manufacturer [6], brush seal leakage performance is commonly expressed in terms of an effective clearance,  $C_E$ , representing the equivalent film thickness in a corresponding “one-sharp tooth” labyrinth seal, defined in US units as:

$$c_E = \dot{m} \frac{\sqrt{(T+460)}}{P_s \pi D_j \varphi} \quad (1)$$

Where

$$\varphi = \begin{cases} \sqrt{\frac{g\gamma}{R}} \sqrt{\frac{2}{\gamma-1}} P_R^{-\frac{(\gamma+1)}{\gamma}} \left( P_R^{\frac{(\gamma-1)}{\gamma}} - 1 \right) & P_R \leq P_{choke} \\ \sqrt{\frac{g\gamma}{R}} \sqrt{\frac{2}{\gamma+1}} \left( \frac{2}{\gamma+1} \right)^{\frac{1}{\gamma-1}} & P_R > P_{choke} \end{cases} \quad (2)$$

And

$$P_{choke} = \left( \frac{2}{\gamma+1} \right)^{\frac{-\gamma}{\gamma-1}} = 1.89 \quad (3)$$

In the formula above,

$c_E$	= effective clearance [in]	$P_s$	= supply pressure [psia]
$D_j$	= rotor diameter [in]	$R$	= specific gas constant [lbf ft/lbm R]
$g$	= gravitational acceleration [in/sec <sup>2</sup> ]	$T_u$	= upstream temperature [°F]
$\dot{m}$	= mass flow rate [lbm/s]	$\gamma$	= ratio of gas specific heats
$P_{choke}$	= gas static pressure/stagnation at Mach 1	$\varphi$	= flow function
$P_R^*$	= supply to discharge pressure ratio, (* atmospheric discharge pressure)		

Figure 13 depicts the calculated effective clearance from the leakage data recorded for the shoed brush seal and hybrid brush seal. The derived effective clearances for the brush seals are a fraction of the typical labyrinth seal clearances. The hybrid brush seal shows a lower effective clearance, ~ 30% in average, than that of the 1<sup>st</sup> generation SBS over the entire range of test pressures. Stephen and Hogg [24] report that the diametral clearance (for a labyrinth seal) is typically 1.0 mm or less for HP (high pressure)

conditions, rising to over 2.0 mm for some LP (low pressure) turbine stage sealing applications. The previous values can be regarded as estimates for typical operating clearances in labyrinth seals for steam turbines, although they can vary depending on the application. For the tested supply pressures ( $P_r = 1.3$  to 3.0), the ratio of effective clearance over rotor radius ( $C_E / R_j$ ) ranges from 0.00033 to 0.00064, approximately 1 order of magnitude smaller than the  $C_E / R_j$  ratio for a typical labyrinth seal,  $\sim 0.0002$ , with a similar rotor diameter. Additionally, the Reynolds numbers calculated for these supply pressures, range from 400-2200 (laminar regime).

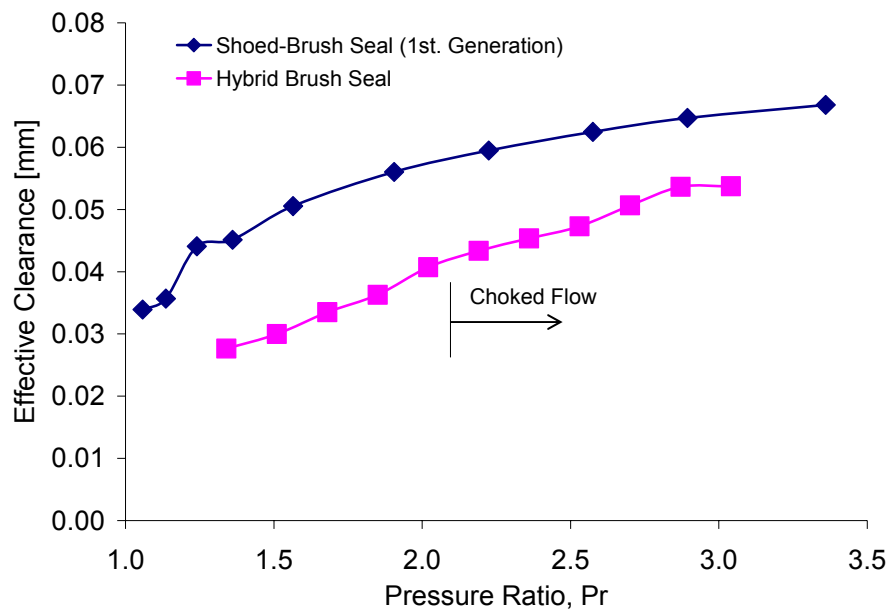


**Figure 13** Calculated effective clearance from leakage data for 1<sup>st</sup> generation shoed-brush seal and hybrid brush seal versus supply to discharge pressure ratios ( $P_r$ )

## CHAPTER V

### IDENTIFICATION OF THE STATIC STRUCTURAL STIFFNESS OF A HBS AT INCREASING SUPPLY PRESSURES

Static load experiments aiming to characterize the static structural stiffness of the HBS are conducted at room temperature (23°C) in the non-rotating test rig configuration described previously. The static loading tests consist of non-tapping and tapping conditions on the test disk. As the test seal is subjected to a force (push or pull), the bristles bend and rub against each other and the bristles facing the back and front plates also rub these surfaces. Bristle surface condition, bristle distribution and packing density contribute to the generation of dry friction resulting from the bristle-to-bristle and bristle-to-back plate interactions. The presence of dry friction in the HBS is evidenced by a stick-slip phenomenon at low loads. Tapping on the disk (having an interference fit to the rotor) relaxes the contact forces between the bristles and adjacent structures (back and front plate); thus diminishing the effects of dry friction and allowing the disk to move further until reaching its actual equilibrium position. In the non-tapping tests, no perturbation is introduced in the seal during the load application.

The static stiffness for the hybrid brush seal at increasing air pressure differentials is estimated from a linear curve fit of the recorded load versus deflection tests. Difference in structural stiffness magnitudes obtained from the tapping and non-tapping conditions confirm the presence of dry friction in the seal during the loading and unloading process. Results show that stiffnesses identified for the tapping condition are more representative of the operating seal stiffness. A description of the experimental procedure follows. Note, static deflection measurements are conducted for loading and unloading conditions.



## Experimental Procedure

The experiments consist in loading the shaft along the horizontal direction with calibrated weights through a cable and pulley system and recording the shaft deflection as the disk presses against the seal. Displacements along two orthogonal directions ( $X$  and  $Y$ ) are measured using eddy current sensors. Figure 14 shows a schematic top view of the test setup for the static load measurements. This figure displays the direction of the applied static load and the coordinate system for the recorded disk displacements.

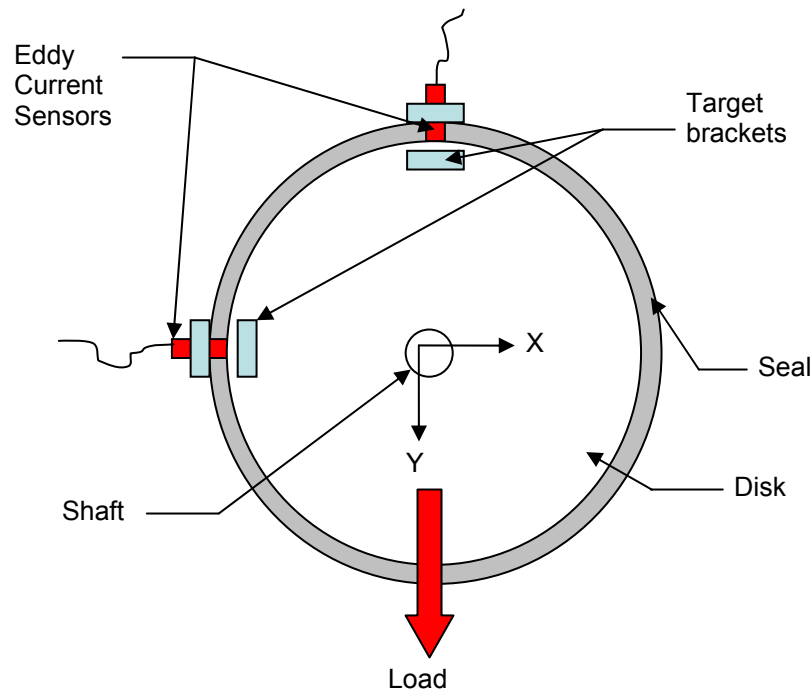


**Figure 14 Schematic view of set up for static load tests**

The test starts by slightly tapping the interference disk with a calibrated hammer to set the initial central equilibrium position of the disk. This initial tapping is done before starting each loading trial at a different supply to discharge pressure ratio, ( $P_r = P_s / P_d$ ). Tapping facilitates the seal deflection by breaking the contact forces and allowing the sliding of the bristles.

The static loading under tapping conditions consists of three simple steps: statically applying a calibrated weight, tapping the seal to overcome the dry friction forces,

recording the displacements. This procedure is then repeated for each subsequent weight. The unloading process follows the same methodology. For the static loading under non-tapping conditions, no perturbation is introduced after each weight is applied. The pulling loads ranged from 10 to 118 N for non-tapping and 10 to 67 N for the tapping condition. The loading range for the tapping condition is smaller than the non-tapping condition given that less weight is required to initiate seal motion.

### Experimental Results and Discussion

Before installing the brush seal, pull load tests render the static stiffness of the shaft and disk assembly, representing the baseline parameters of the test rig. Table 4 displays the theoretical and experimental static stiffness for the shaft/disk assembly only. The equivalent system stiffness can be expressed in terms of the static load deflection shape,

$\psi(z) = \frac{(3Lz^2 - z^3)}{2L^3}$ , for a cantilever beam [25], as

$$K_{eq} = K_{shaft} + K_s \left( \frac{\psi(L_s)}{\psi(L_f)} \right)^2 \quad (4)$$

where the shaft stiffness is calculated from  $K_{shaft} = \int_0^L EI \left( \frac{\partial^2 \psi(z)}{\partial z^2} \right)^2 dz$ ,  $E$  and  $I$  are the shaft material Young modulus and area moment of inertia, respectively. The theoretical identified shaft stiffness is used for identification of the HBS stiffness.

**Table 4 Static stiffness for shaft-disk assembly, experimental and theoretical (non-rotating test rig configuration)**

Stiffness Values	SI Unit	English Units
Experimental, $K_{ex}$	47.4 kN/m	270 lbf/in
Theoretical, $K_{shaft}$	52.7 kN/m	311 lbf/in

Figure 15 shows equivalent seal deflection along the principal direction (along direction of the applied load) for (A) non-tapping and (B) tapping conditions without external pressurization, i.e.  $P_r = 1.0$ . For the non-tapping case the seal begins to show considerable deflection after 60 N. For the tapping case the seal deflects at a lower load, i.e. 10 N. The perturbation on the disk allows the seal to overcome the dry friction effects much faster. Seal hysteresis shown by the area between the loading and unloading section of the non-tapping curve evidences the prevalent friction effects present in the brush seal.

Appendix A contains figures depicting the seal deflections for increasing supply pressures, i.e. pressure ratios  $P_r$  from 1.3 to 3.0, for the non-tapping and tapping testing conditions. For the tapping conditions, the equivalent system stiffness,  $K_{eq}$ , is obtained from a linear curve fit of the load (loading portion of the curve) versus deflection measurements for each pressure ratio condition. The seal stiffness ( $K_s$ ) follows from Eq. (4) after subtraction of the shaft stiffness from  $K_{eq}$ . However, for the non-tapping tests, since the load versus deflection is not unique showing a pronounced hysteresis, a representative equivalent stiffness is derived from the ratio of the maximum load difference divided by the maximum displacement recorded, see Figure 15(A).

The seal deflections along the cross-directions ( $90^\circ$  away from the load direction) are at least one order magnitude lower than the principal deflections and do not follow a specific pattern (non-linear).

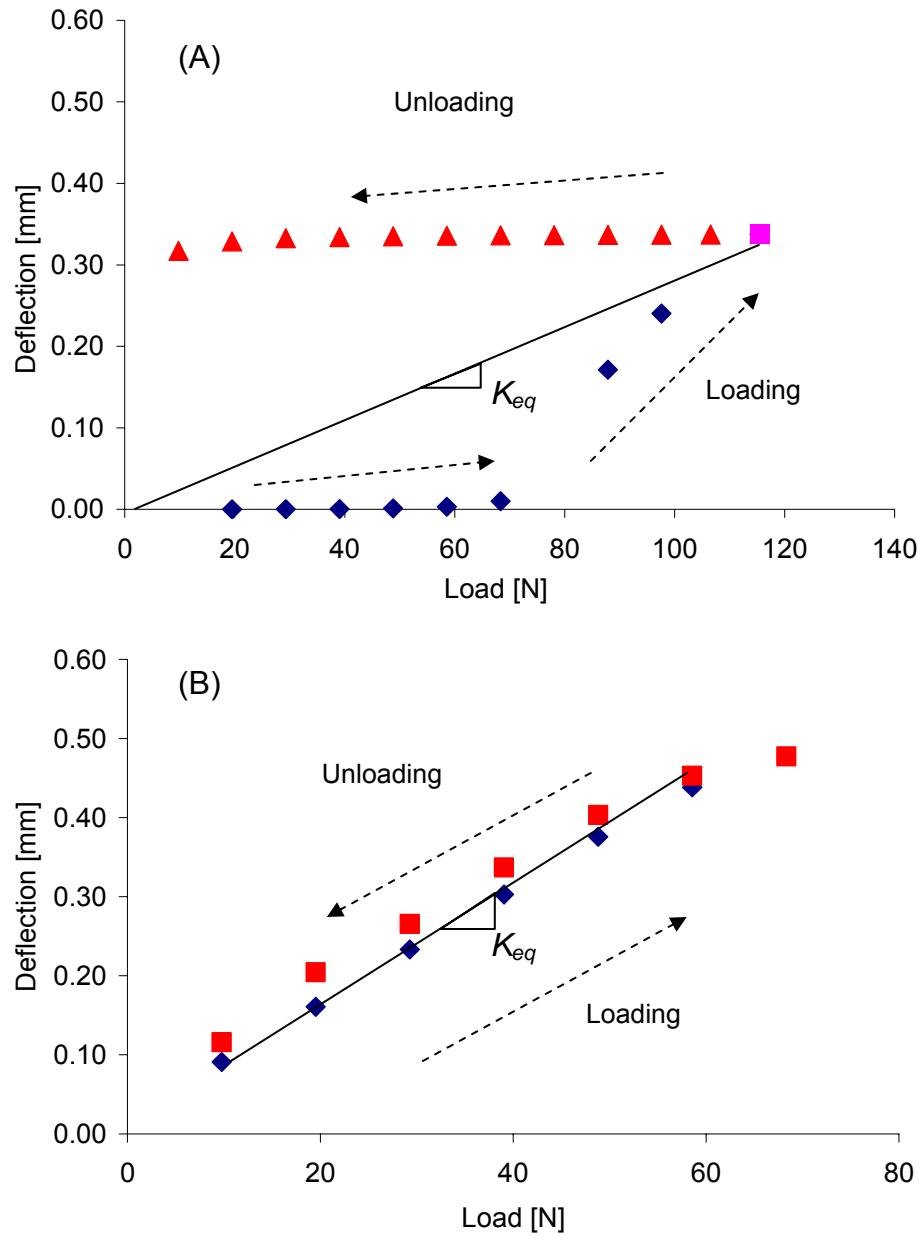
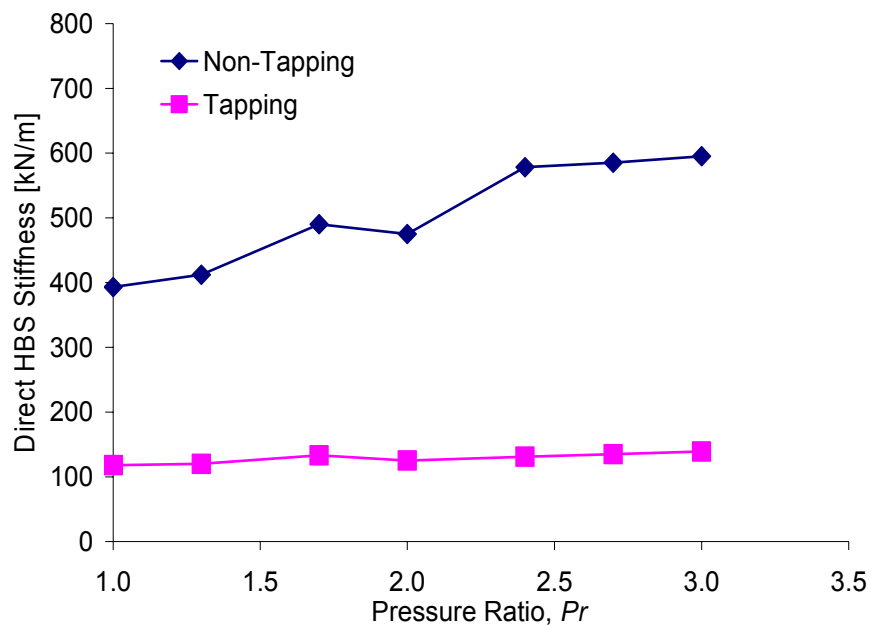


Figure 15 Seal direct deflection versus applied load at pressure ratio  $P_r=1.0$  for (A) non-tapping and (B) tapping testing condition. Lines for extraction of static stiffness shown

Figure 16 shows the brush seal direct stiffness for increasing pressure ratios for the non-tapping and tapping conditions. The direct stiffness derived from tapping tests remains nearly constant throughout the test pressure ratios (~15 % increase). The brush seal stiffens for the non-tapping condition increasing significantly with increasing pressures (~34 % increase). As the supply pressure increases, dry friction effects become larger due to the increase in the normal contact forces between the seal elements and the larger contact with the front and back plate. Table 5 displays the numerical values graphed in Figure 16 for both static test conditions.



**Figure 16 Direct static stiffness of hybrid brush seal for non-tapping and tapping conditions at increasing pressure ratios ( $P_r$ )**

**Table 5 System static stiffness and hybrid brush seal direct stiffness for increasing pressure ratios ( $P_r$ ). Non-tapping and tapping testing condition**

Pressure Ratio	Non Tapping		Tapping	
	Equivalent System Stiffness, $K_{eq}$	Hybrid Brush Seal Direct Stiffness*, $K_s$	Equivalent System Stiffness, $K_{eq}$	Brush Seal Direct Stiffness*, $K_s$
$P_r$	kN/m [lbf/in]	kN/m [lbf/in]	kN/m [lbf/in]	kN/m [lbf/in]
1.0	342 [1952]	393 [2242]	140 [798]	118 [674]
1.3	356 [2035]	412 [2355]	141 [805]	120 [684]
1.7	413 [2360]	490 [2796]	151 [860]	133 [759]
2.0	403 [2301]	475 [2716]	145 [826]	125 [712]
2.4	478 [2732]	578 [3302]	150 [854]	131 [751]
2.7	484 [2762]	585 [3343]	152 [868]	135 [770]
3.0	491 [2803]	595 [3398]	155 [888]	139 [796]

\*:Recall  $\left(\frac{\psi(L_s)}{\psi(L_r)}\right)^2 = 0.73$  for non-rotating test rig configuration

## CHAPTER VI

### SINGLE PAD STIFFNESS PREDICTION MODEL AND OVERALL STIFFNESS FOR A HBS

The static structural stiffness of a HBS at  $P_r = 1.0$  is predicted using a modified version of the stiffness prediction model introduced by Delgado *et al.* [19] to predict the overall static stiffness of a 1<sup>st</sup> generation shoed brush seal (SBS). The seal overall static stiffness (radial direction) is found by assembling the individual stiffness of each pad. Measured static stiffness in [18] obtained from static load tests validate the original version of the stiffness prediction model.

The original model only accounts for the effects of the bristle pack. In the modified version, the stiffness of the cantilever beam elements is added to the bristle pack stiffness to obtain the overall HBS stiffness, considering that the cantilever elements and the bristle pack act as springs in parallel. The cantilever beams are modeled, following the analysis in [19], as fixed-fixed beam elements.

The model is based in the following assumptions:

- No side pressurization
- Bristles are treated as pinned to a pad
- Beam elements are fixed to the pads
- The curvature of the pad is considered insignificant, thus the pad is treated as straight
- No interaction (contact and friction) among bristles is accounted for
- No interaction between adjacent pads
- Stiffness is independent of pressure gradient across seal

Figure 17 show a schematic view of the pad and bristle pack assembly used for this model.

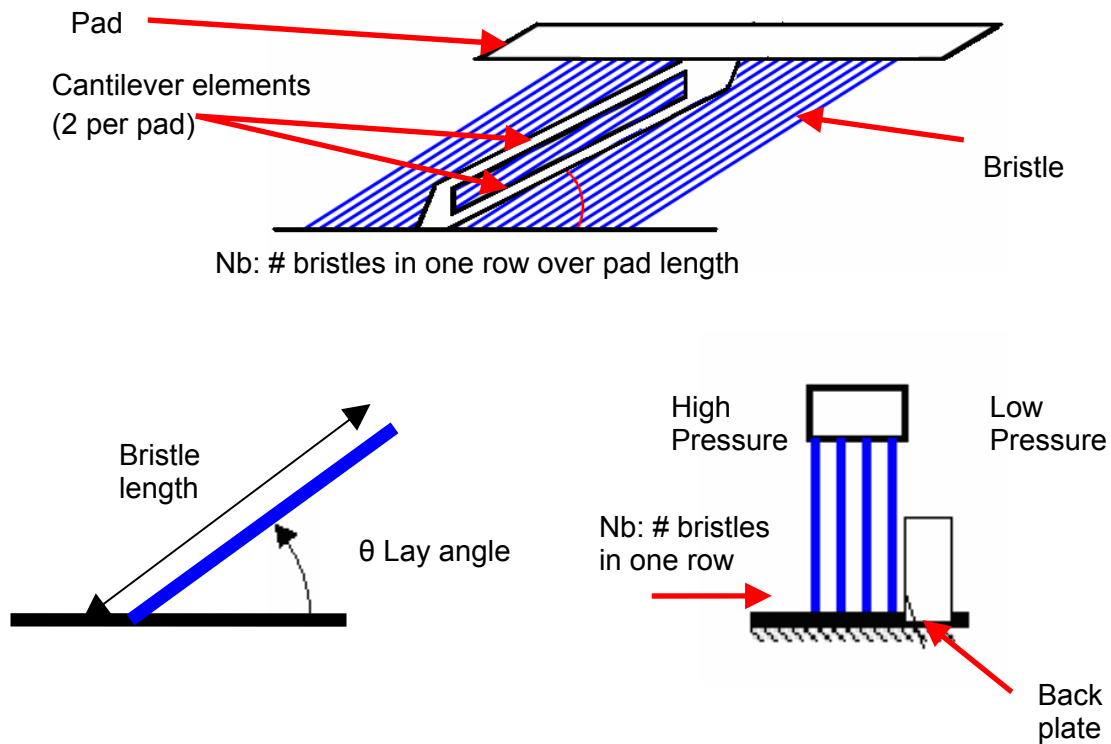


**Figure 17 Schematic view of the HBS pad for stiffness prediction**

### Computational Programs

The computational programs use MATHCAD® and MS EXCEL® interfaces. Figure 18 displays the visual interface with the seal (bristles and pad) geometry and properties and output results for the seal static stiffness and pad stiffness matrix (i.e. for the condition with no shaft rotation and  $P_r = 1.0$ ). Table 1 lists the input data used for the computational program. For these conditions the overall HBS stiffness prediction is 135.8 kN/m (~775.5 lbf/in) as shown in Figure 25. The prediction is within 15 % of the stiffness identified from static load tests with no pressure differential across the seal at  $P_r = 1.0$ .



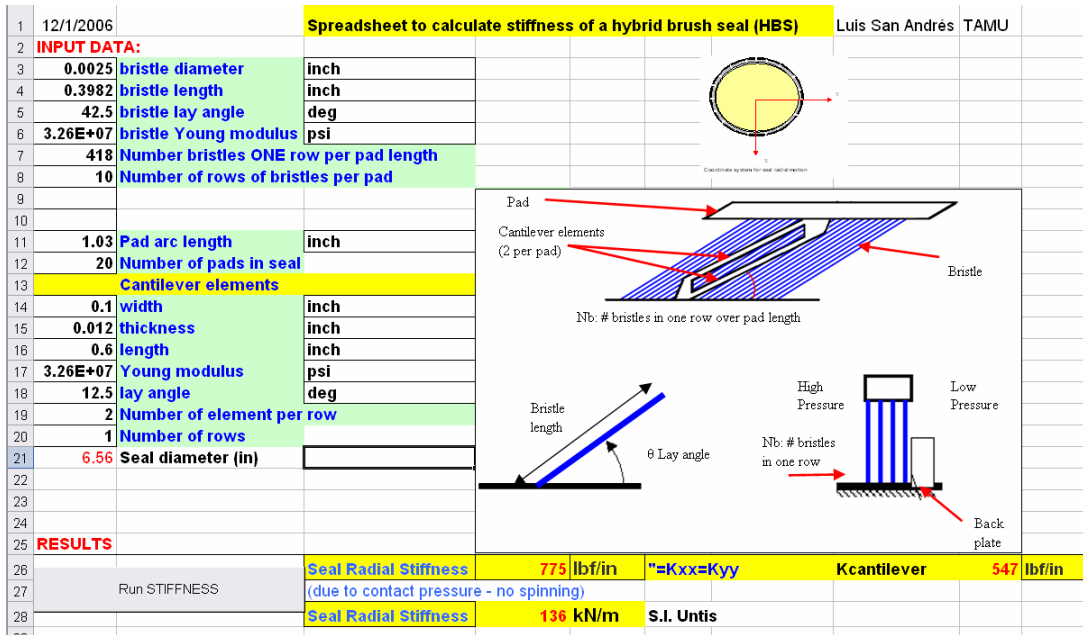


Figure 18 Visual graphical user interface for calculation of HBS static stiffness

## CHAPTER VII

### BREAK-AWAY TORQUE ESTIMATION FOR A HBS UNDER STATIC CONDITION FOR INCREASING SUPPLY PRESSURES

The static break away torque is measured with the rotor in a centered position with respect to the seal for increasing supply pressures. This break away torque is necessary to overcome dry friction between seal pads and the rotor surface and initiate rotation. Experimental results show an inversely proportional relationship between torque and increasing supply pressures under static conditions (i.e. no rotation). Results show that break-away torque drops drastically as a function of supply pressure and rotor speed.

#### Experimental Procedure for Static Torque Measurements

A simple test procedure is followed to characterize the torque of a HBS under static conditions for increasing pressure ratios,  $P_r = \frac{P_s}{P_d} = 1.0$  (no external pressurization), 1.7 and 2.4. The rotor assembly (shaft and disk), with the HBS in place, is rotated in the direction of the lay angle with a torque wrench. The static torque is recorded at the instant disk rotation initiates.

#### Experimental Results and Discussion

Figure 19 shows the static torque versus pressure ratio for a HBS under static conditions. At  $P_r = 1.0$  (no external pressurization) the HBS experiences a relative high resistance to rotation when compared to the pressurized cases. The results presented in this figure correspond to average values from five trials, error bars for the current measurements are small and cannot be observed in the figure. The torque is primarily affected by the radial interference fit of the seal. As the pressure increases from  $P_r = 1.0$  to 1.7, the torque drops approximately 75%. These results show that the contact force between the shaft and the seal pads is eliminated. A minute step machined on the HBS

pads (upstream section) allows the generation of hydrostatic pressure film as the air flows across the HBS; consequently the pads separate from the surface of the rotor prior to shaft rotation.

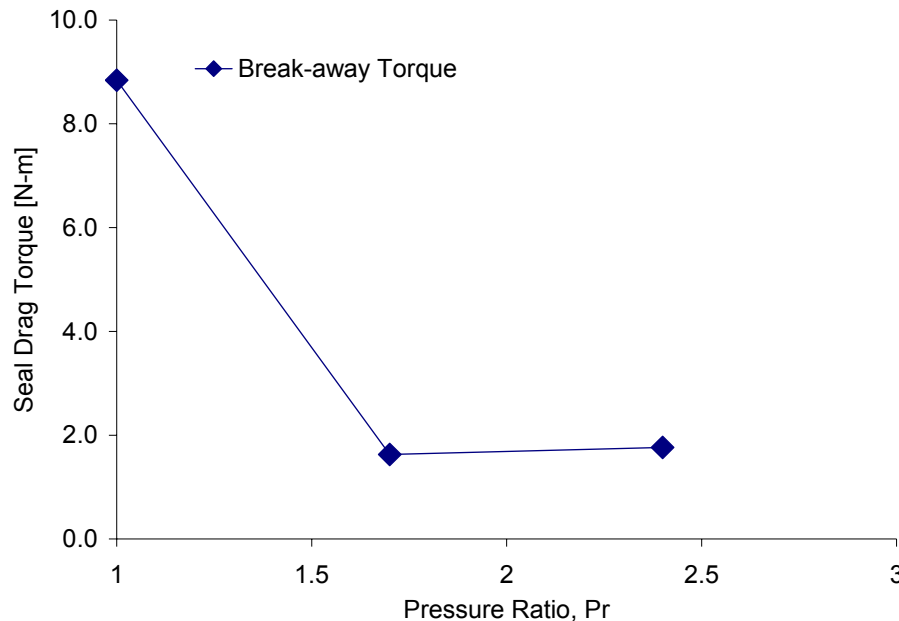


**Figure 19 Break-away torque versus supply pressure to discharge pressure ratio ( $P_r$ ) for a hybrid brush seal (HBS) under static conditions**

The HBS pad design for a HBS (see Fig. 4) suggests that as high pressure air flows across the rotor/seal interface pad-lift off will occur, even without shaft rotation. In terms of leakage performance, this finding implies that most of the air is flowing underneath the pads instead of the bristle pack. Indeed, a visual inspection using a colored-dye to track the path of the air across a HBS reveals that most of the air leaks through the interface between the rotor and seal pads, regardless of the existing interference fit between these two elements.

## CHAPTER VIII

### IDENTIFICATION OF HBS STRUCTURAL STIFFNESS AND EQUIVALENT VISCOUS DAMPING

This section details the identification of the test seal structural stiffness and damping coefficients from unidirectional dynamic load experiments performed on the non rotating test rig described in Chapter III. The tests follow the experimental procedure detailed in [20].

#### **Experimental Procedure**

First, the supply pressure ( $P_s$ ) is manually adjusted to a desired value. This pressure is measured at the inlet of the cylindrical steel vessel using a calibrated pressure sensor. Once the supply pressure is set, the electromagnetic shaker excites the test seal with single-frequency loads from 20-110 Hz (5 Hz increments) and at three amplitudes (55N, 63N, and 66N). The excitation load magnitudes are maintained constant throughout the test frequency range inducing periodic motions on the system. The tests are conducted for three absolute supply pressures ( $P_s = 169, 238$  and  $307$  kPa). Recall, that pressure ratio ( $P_r$ ) is defined as supply pressure ( $P_s$ ) over discharge pressure ( $P_d$ ), ( $P_r = \frac{P_s}{P_d}$ ). The supply pressure is continuously monitored during the forced excitation cycles. After a dynamic loading test at a specific supply pressure is completed, the air inlet is shut off prior to readjusting the supply pressure for the next test. Table 6 presents the flow conditions across the HBS.

**Table 6 Flow conditions for dynamic load tests on a hybrid brush seal**

<b>Fluid: air</b>	SI Unit	US Unit
Absolute supply pressure (upstream), $P_s$	169 to 307 kPa	19.7 to 44.5 psia
Absolute discharge pressure (downstream), $P_d$	101 kPa	14.5 psia
Temperature upstream, $T_u$	69 to 71 °F	20.5 to 21.7 °C

The lowest excitation load (55 N) is set to be large enough to induce motions of the disk and test seal, and the largest load (63 N) is limited by the largest amplitude of motion allowed by the seal (~0.50 mm radially). Figures 20 and 21 show the waterfall plots of the displacement and acceleration response of the seal under 55 N and 66 N dynamic force excitations, respectively. Each graph depicts the amplitude and frequency of motion along the vertical and horizontal scales, respectively. The abscissa represents the variations in excitation frequency, 20 Hz to 110 Hz. The analysis of the test results indicate that for loads less than 55N, the seal motions correspond to a nonlinear and non repeatable stick-slip regime, most difficult to characterize. In the stick-slip regime the dry friction effects within the seal components is evidenced by the presence of larger super harmonic components (3X, 5X). As the load amplitude increases the seal response transitions into a macro-slip regime of motion, which allows the quantification of the seal energy dissipation performance in terms of physical parameters. Similar behavior is experienced for the externally pressurized cases.

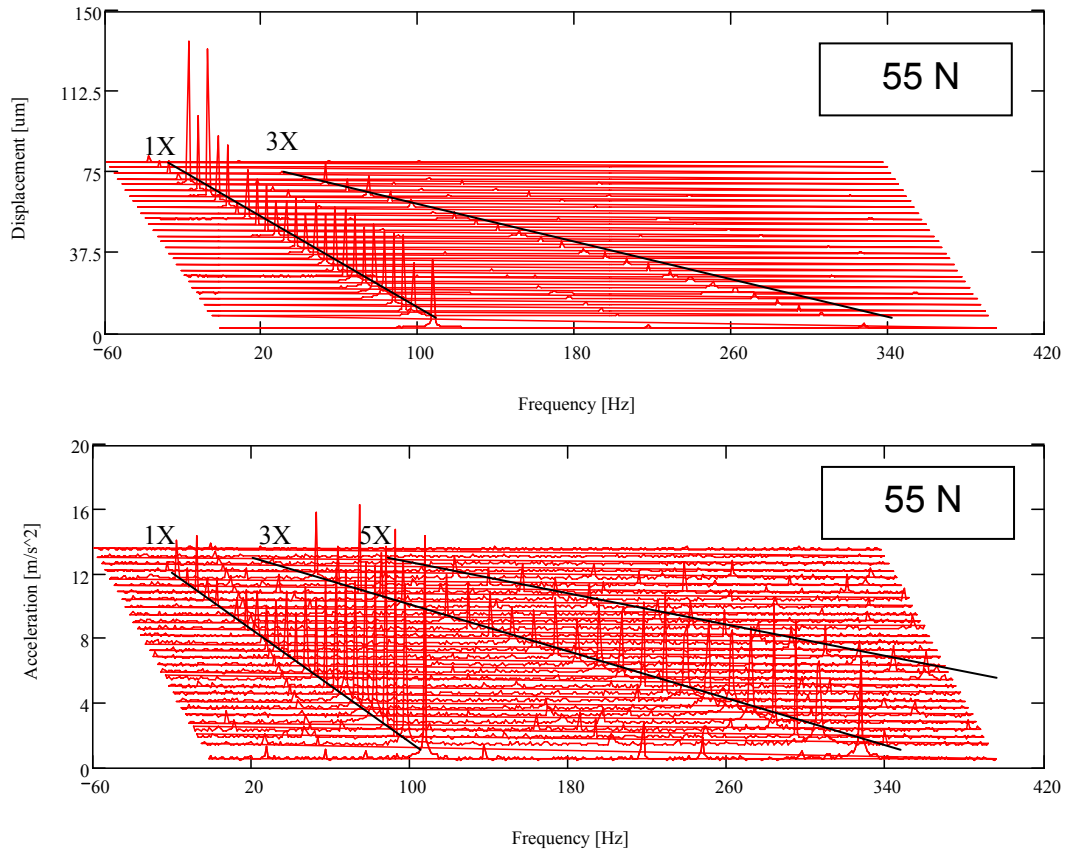


**Figure 20** Waterfall of recorded disk (seal) displacement and accelerations due to an external harmonic load (55 N). Frequency range (20 Hz- 110 Hz). Pressure ratio  $P_r=1.0$

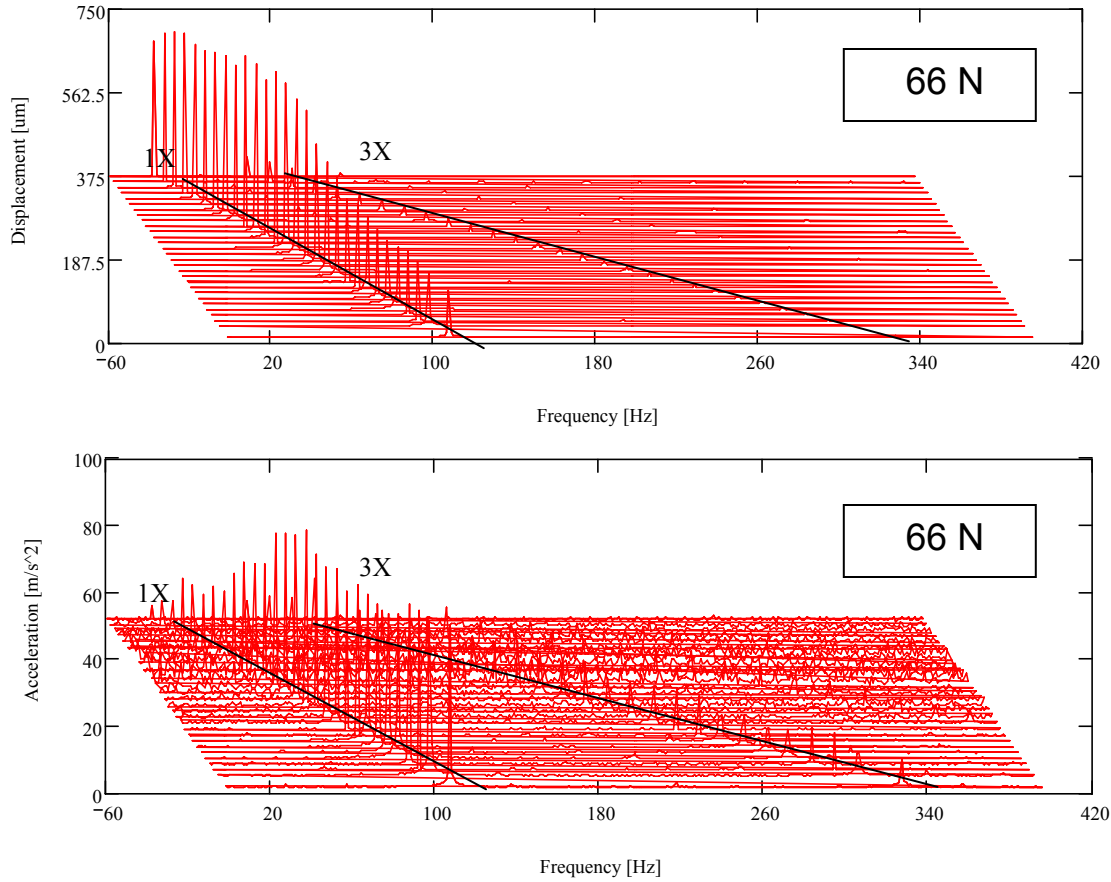


**Figure 21** Waterfall of recorded disk (seal) displacement and accelerations due to a external harmonic load (63 N). Frequency range (20 Hz- 110 Hz). Pressure ratio  $P_r=1.0$

### Parameter Identification Method

The parameter identification method follows the procedure introduced by Delgado and San Andrés [20]. The equation of motion of the test system subjected to a unidirectional dynamic load is

$$M_{eq} \ddot{x} + K_{eq} x + C_{eq} \dot{x} = F_{ext} \quad (5)$$

with  $(M_{eq}, K_{eq}, C_{eq})$  as the system equivalent mass, stiffness and viscous damping coefficients, respectively.  $F_{ext}$  and  $x$  represent the applied external excitation force and linear displacement of the equivalent system, respectively. Figure 22 shows a schematic

view of the test rig and its equivalent mechanical system. Considering that the seal is not located at the same axial location of the sensors and applied force, the equivalent system parameters at location  $L_f$  are derived from potential and kinetic energy principles. The equivalent system stiffness is expressed in terms of the static load deflection shape,  $\psi(z) = \frac{(3Lz^2 - z^3)}{2L^3}$ , for a cantilever beam [25], as

$$K_{eq} = K_{shaft} + K_s \left( \frac{\psi(L_s)}{\psi(L_f)} \right)^2 \quad (6)$$

where the shaft stiffness is calculated from  $K_{shaft} = \int_0^L EI \left( \frac{\partial^2 \psi(z)}{\partial z^2} \right)^2 dz \approx 52 \text{ kN/m}$ , which was previously identified for the static loading tests.  $E$  and  $I$  are the shaft material Young modulus and shaft area moment of inertia, respectively. Recall, that the test rig configuration without shaft rotation is used in these measurements.

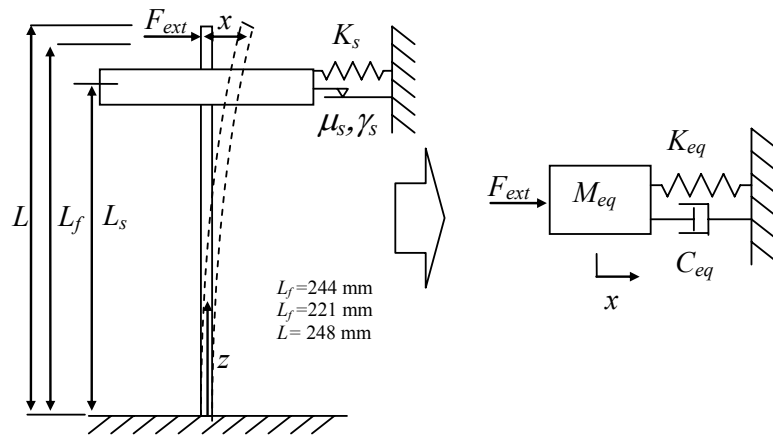


**Figure 22 Schematic view of test system and representation of equivalent mechanical system**

From the system potential and kinetic energies, the equivalent mass ( $M_{eq}$ ) is identified as,



$$M_{eq} = M_d \left( \frac{\psi(L_s)}{\psi(L_f)} \right)^2 + M_{shaft\ equiv.} \quad (7)$$

where  $M_D$  is the aluminum disk mass (1.47 kg);  $M_{shaft\ equiv} = \int_0^L \rho A \psi(z)^2 dz \approx 0.08$  kg.  $\rho$

and  $A$  denote the shaft density and cross-sectional area, respectively.

Expressing the applied force and ensuing displacements in terms of its main frequency component (i.e.  $\bar{x} = x e^{i\omega t}$  and  $\bar{F} = F_{ext} e^{i\omega t}$ ), Eq. (5) becomes

$$Z = \frac{\bar{F}}{\bar{x}} = (K_{eq} - \omega^2 M_{eq}) + i \omega C_{eq} \quad (8)$$

where  $Z$  is a complex impedance function. The test equivalent stiffness ( $K_{eq}$ ) and mass ( $M_{eq}$ ) coefficients can be directly extracted from the real part of  $Z$ .

The dynamic response of the hybrid brush seal involves relative motions of the seal components and bending of the bristles and the slender EDM beams supporting the pads. Thus, the energy dissipation of the test seal is modeled in terms of dry friction coefficient ( $\mu$ ) and a loss factor coefficient ( $\gamma$ ). The energy dissipated by such damping mechanisms in one period of motion is defined as [25]

$$E_{dis} = \gamma_{eq} \pi K_{eq} |\bar{x}|^2 + 4\mu |\bar{F}| |\bar{x}| \quad (9)$$

where  $\gamma_{eq}$  and  $\mu$  represent an equivalent structural loss coefficient and dry friction coefficient, respectively. The brush seal loss coefficient ( $\gamma$ ) can be expressed in terms of the equivalent structural loss coefficient as

$$\gamma = \gamma_{eq} \frac{K_{eq}}{K_s} \left( \frac{\psi(L_f)}{\psi(L_s)} \right)^2 \quad (10)$$

The loss factor ( $\gamma$ ) and dry friction coefficient ( $\mu$ ) are obtained by equating the energy dissipated to the work exerted on the system

$$W = \oint F_{ext} \dot{x} dt \quad (11)$$

with a least square curve fit. The equivalent viscous damping follows from equating the estimated dissipated energy by dry friction and structural damping to the energy dissipated by viscous damping.

$$C_{eq} = \frac{\gamma_{eq} K_{eq}}{\omega} + \frac{4\mu|\bar{F}|}{\pi\omega|\bar{x}|} \quad (12)$$

A curve fit of the real part of the dynamic impedance

$$(K_{eq} - \omega^2 M_{eq}) = \text{Re}(Z) = \text{Re}(\bar{F} / \bar{x}) \quad (13)$$

yields the equivalent mass and stiffness coefficients of the test system. The results of the identified system coefficients follow.

### **Experimental Results and Discussion**

Tables 7 and 8 list the stiffness, mass and energy dissipation coefficients obtained from the parameter identification procedure for the equivalent system and HBS, respectively. The results show that the direct stiffness increases with increasing supply pressure (~35% for pressure ratios: 1.0 to 3.0). The magnitudes of the stiffness coefficients for the equivalent mechanical system and HBS reproduce closely values obtained from static loading tests under tapping conditions.

**Table 7 Identified test system equivalent parameters from dynamic load tests (Load 66 N & 63 N, 20 Hz to 110 Hz) for increasing pressure ratios ( $P_r$ ). Non-rotating test rig configuration**

Pressure ratio*	Equivalent system			
	$P_r = 1.0$	$P_r = 1.7$	$P_r = 2.4$	$P_r = 3.0$
Stiffness [kN/m], $K_{eq}$	120 ( $\pm 6$ )	147 ( $\pm 7$ )	155 ( $\pm 8$ )	155 ( $\pm 8$ )
Mass [kg.], $M_{eq}$	1.11 ( $\pm 0.03$ )	1.13 ( $\pm 0.03$ )	1.18 ( $\pm 0.03$ )	1.16 ( $\pm 0.03$ )
$R^2$ (correlation factor)				
Dynamic stiffness ( $K_{eq} - M_{eq}\omega^2$ )	0.97	0.98	0.98	0.97
Dry Friction coefficient, $\mu$	0.66	0.51	0.64	0.69
Loss Factor coefficient, $\gamma$	0.27	0.26	0.18	0.14

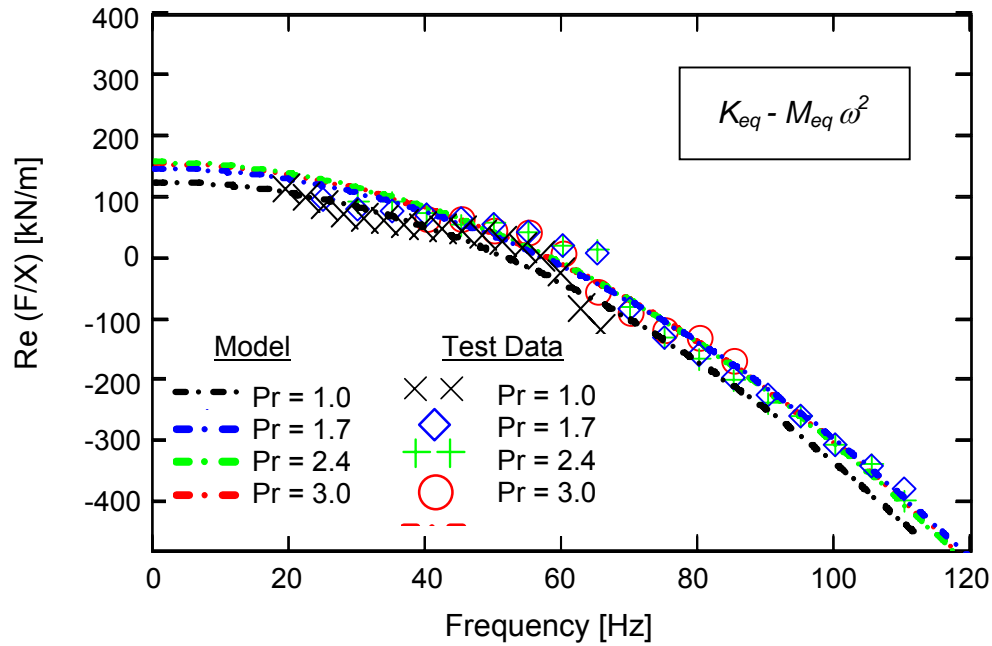
\*: atmospheric discharge pressure

**Table 8 Identified hybrid brush seal (HBS) parameters from dynamic load tests (Load 66 N & 63 N, 20 Hz to 110 Hz) for increasing pressure ratios ( $P_r$ ). Non-rotating test rig configuration**

Pressure ratio*	Hybrid Brush Seal			
	$P_r = 1.0$	$P_r = 1.7$	$P_r = 2.4$	$P_r = 3.0$
Stiffness [kN/m]	93 ( $\pm 5$ )	130 ( $\pm 6$ )	141 ( $\pm 7$ )	141 ( $\pm 7$ )
Dry Friction coefficient, $\mu$	0.66	0.51	0.64	0.69
Loss Factor coefficient, $\gamma$	0.42	0.40	0.27	0.22

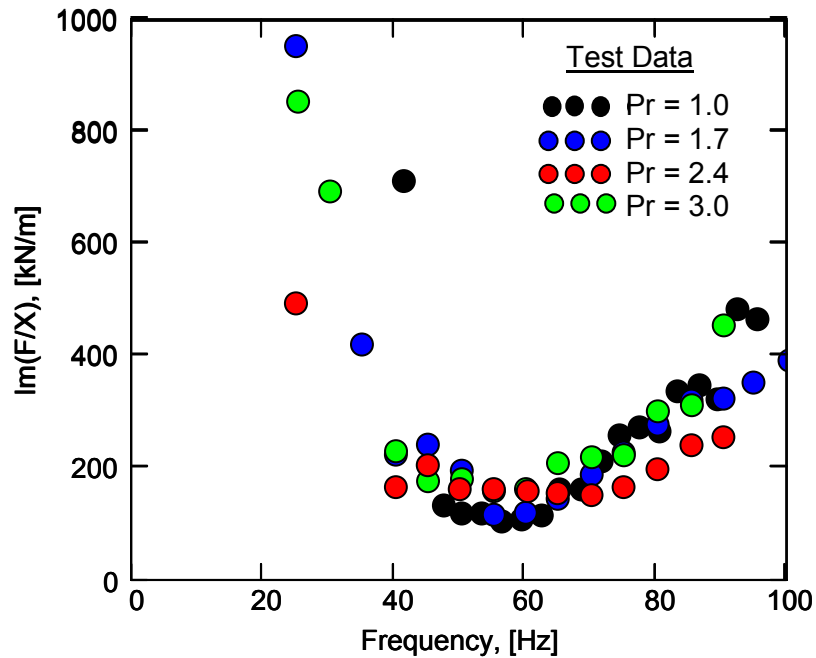
\*: atmospheric discharge pressure

Figure 23 depicts the real part of the test system impedance  $\text{Re}(\bar{F}/\bar{x})$  obtained from dynamic load tests for an excitation load of 63 N. The model reproduces the test data very well, showing a minimal increase in system stiffness with increasing pressure ratios: 1.0 to 3.0. This increment is negligible when compared to similar experimental results obtained by Basu *et al* [12] in which the stiffness of a conventional brush seal increased by about six times for a pressure differential of 307 kPa (30 psig). As mentioned earlier, a lower pressure-induced radial stiffness reduces the likeliness of bristle “hang up” i.e. after rotor radial excursions the bristles do not return to their initial position, temporarily increasing the leakage area across the seal.



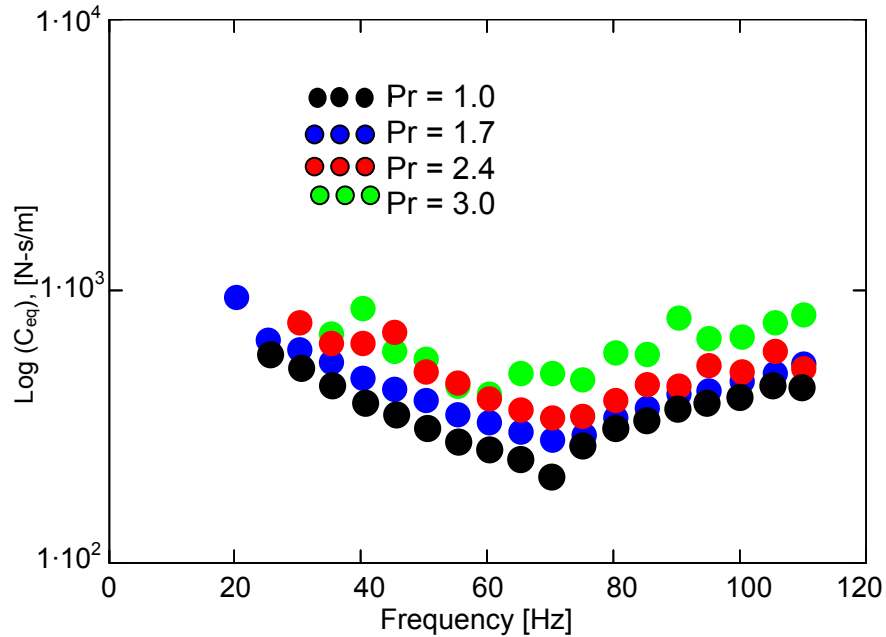
**Figure 23 Identified system dynamic stiffness versus excitation frequency. Load magnitude = 63 N, for increasing supply pressure to discharge pressure ratios ( $P_r$ ) and no shaft rotation**

Figure 24 shows the imaginary part of the test system impedance  $\text{Im}(\bar{F}/\bar{x})$  versus excitation frequency for a periodic load of 63N from  $P_r = 1.0$  to 3.0. Test data shows no significant variation as the supply pressure increases across the HBS. The values decrease with excitation frequency, reaching a minimum at the test system natural frequency ( $\sim 58$  Hz) and thus indicating that the seal damping is due to a contribution of Coulomb damping and structural damping. Furthermore, at the natural frequency of the system the seal mostly provides structural (hysteretic) damping.



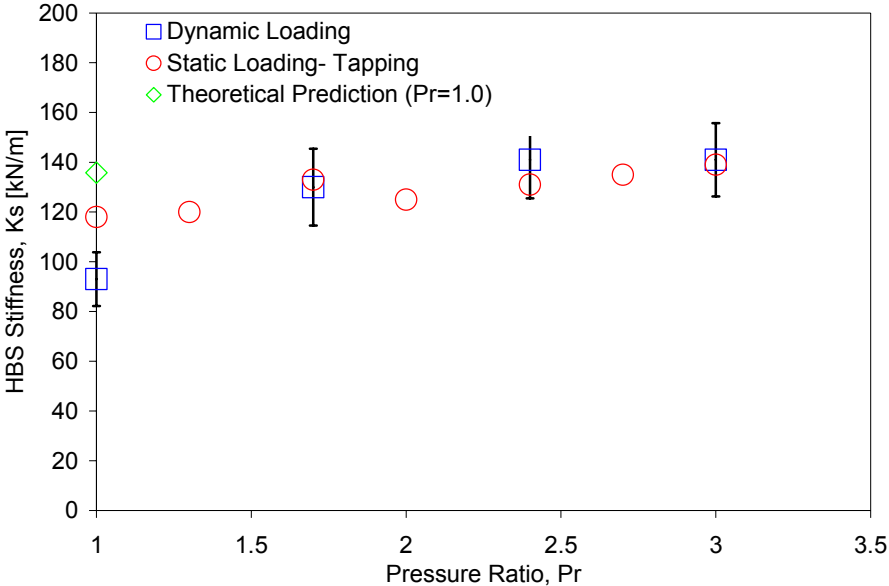
**Figure 24** Imaginary part of the test system versus excitation frequency. Load magnitude = 63 N, for increasing supply pressure to discharge pressure ratios ( $P_r$ ) and no shaft rotation

Figure 25 shows the identified equivalent *viscous* damping coefficient. Largest values of equivalent viscous damping occur at low frequencies, steadily decreasing as the test system approaches its natural frequency ( $\sim 58$  Hz). This behavior is typical of a system having mainly Coulomb and structural damping [26]. Results show that equivalent system damping increases marginally with increasing supply pressure.



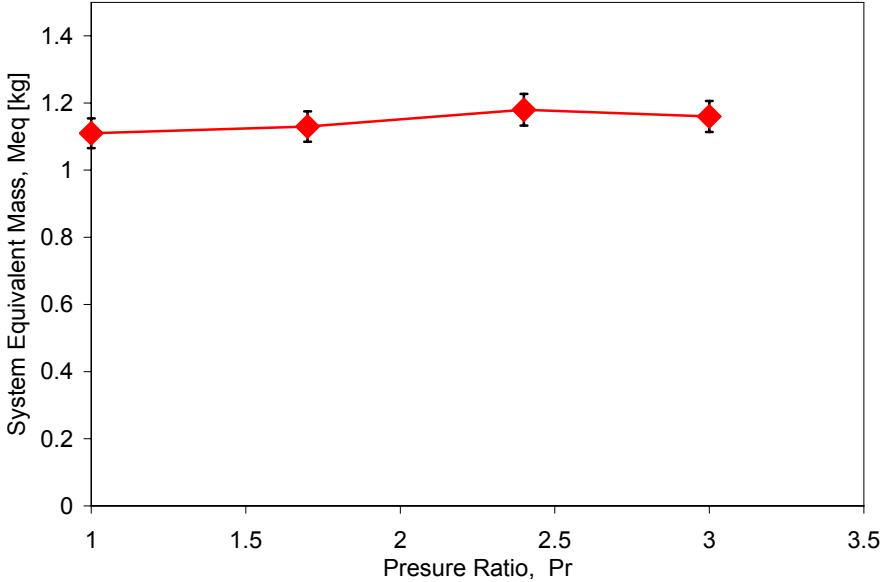
**Figure 25** Equivalent viscous damping versus excitation frequency. Load magnitude = 63 N, for increasing supply pressure to discharge pressure ratios ( $P_r$ ) and no shaft rotation

Figure 26 depicts the HBS direct stiffness identified from the static (tapping case) and dynamic load tests at increasing supply pressures. The stiffnesses obtained from the dynamic load tests for the range of supply pressures are comparable to the stiffness values obtained by the static load tests under tapping conditions. The figure includes error-bars for the identified stiffnesses at each supply pressure. Appendix E presents the uncertainty analysis for the seal stiffness values obtained.



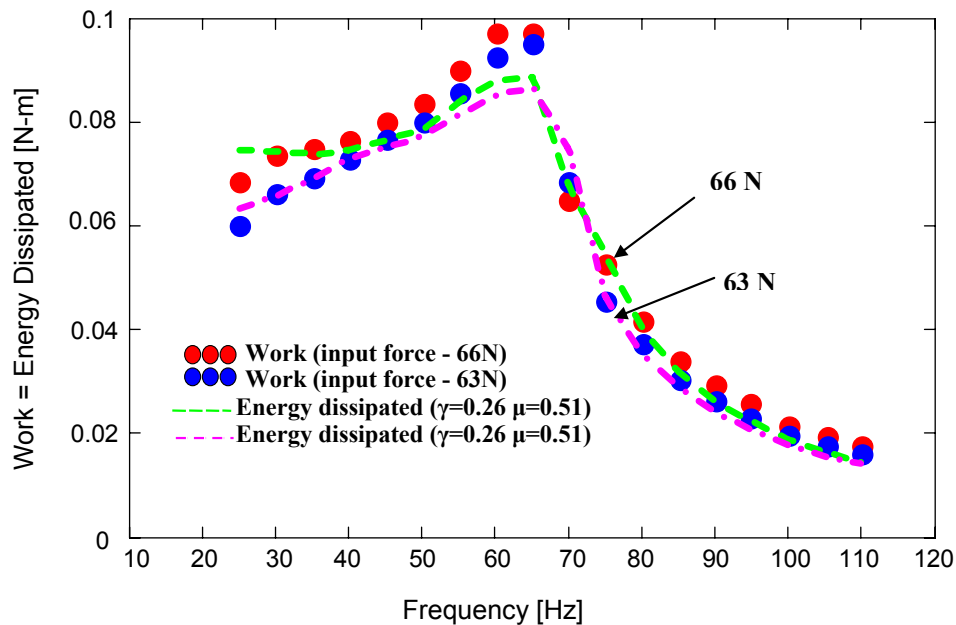
**Figure 26** Direct stiffness of hybrid brush seal identified from static (tapping) and dynamic load tests versus supply pressure to discharge pressure ratio ( $P_r$ )

Figure 27 shows the system equivalent mass coefficient ( $M_{eq}$ ) for the different supply pressures tested. The results indicate that the equivalent “vibrating” mass at the location of the excitation force remains nearly constant for increasing supply pressure.



**Figure 27** System equivalent mass for hybrid brush seal versus supply pressure to discharge pressure ratio ( $P_r$ )

Figure 28 shows the work input to the system and the estimation of the energy dissipated using the identified coefficients ( $\gamma$ ,  $\mu$ ). At  $P_r=1.7$  the physical model slightly underestimates the measured work input that results from excitation frequency with 63N and 66 N. Figures 29 and 30 depict the work and energy dissipation curves for  $P_r = 2.4$  and 3.0, respectively. For these last two figures the parameter identification yields consistent results, meaning that the model accurately estimates the energy dissipated with respect to the work input into the equivalent mechanical system.



**Figure 28** Work=energy dissipated by test system versus frequency for one period of motion. Loads 63 N and 66 N on frequency range 20-110 Hz. No shaft rotation. Pressure ratio,  $P_r=1.7$

Figures 29 and 30 show an irregular pattern at low frequencies (i.e. below test system natural frequency  $\sim 58$  Hz). This is due to an increase in the threshold force necessary to traverse from a stick-slip regime to a macro-slip regime. As the supply pressure rises, the contact force between the bristles increases and the load required to induce motions in the macro-slip regime is larger.



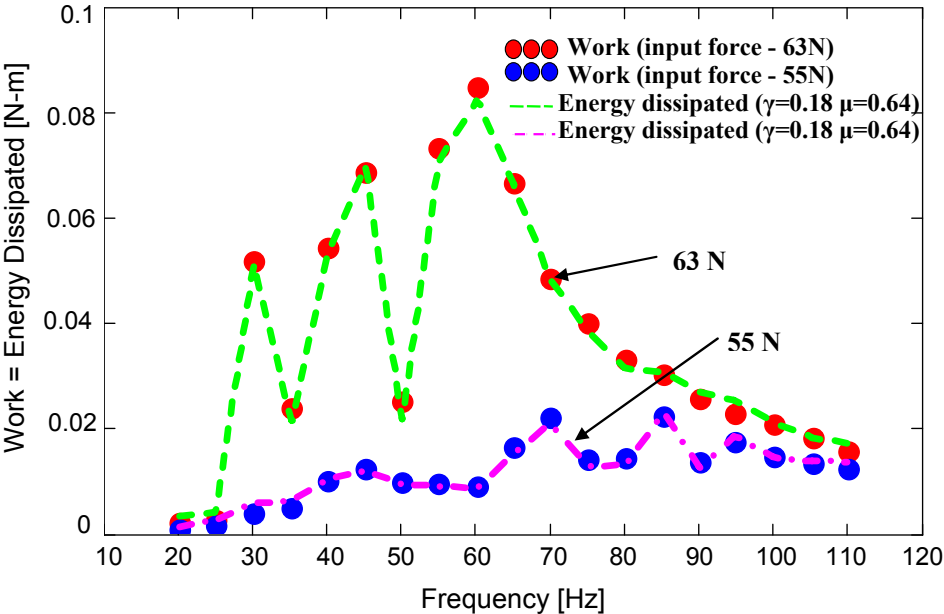


Figure 29 Work=energy dissipated by test system versus frequency for one period of motion. Loads 55 N and 63 N on frequency range 20-110 Hz. No shaft rotation. Pressure ratio ,  $P_r = 2.4$

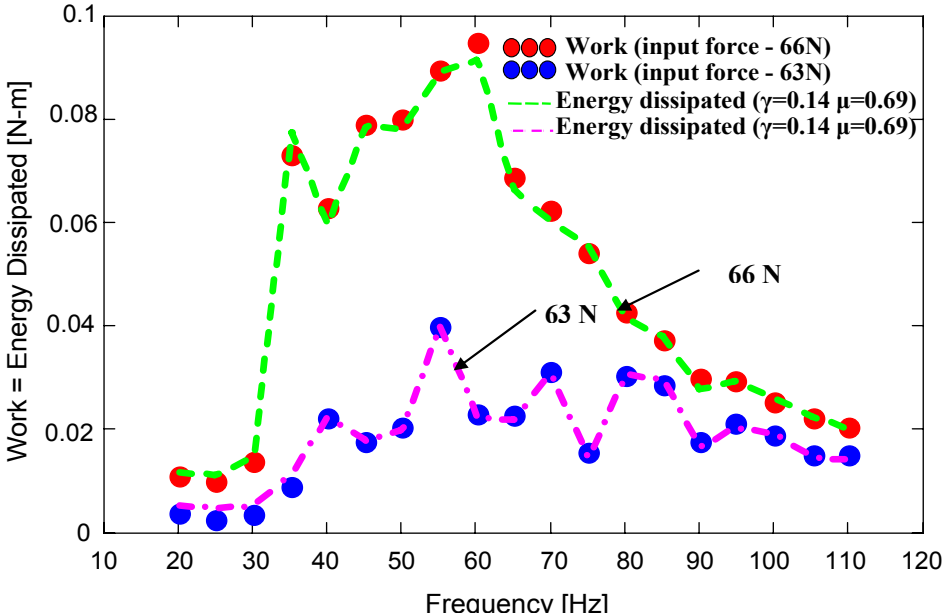
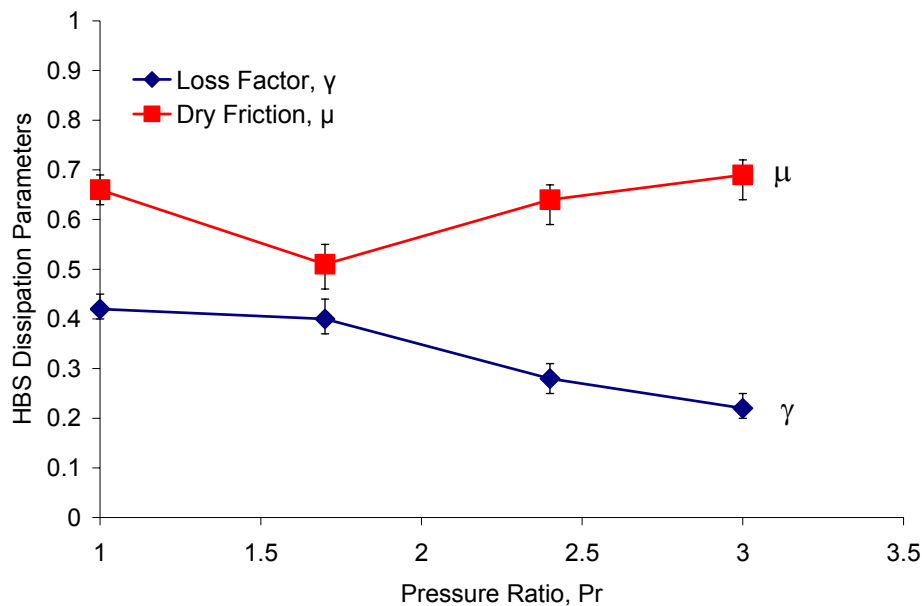


Figure 30 Work=energy dissipated by test system versus frequency for one period of motion. Loads 63 N and 66 N on frequency range 20-110 Hz. No shaft rotation. Pressure ratio ,  $P_r = 3.0$

Figure 31 illustrates the variation of the identified HBS loss factor ( $\gamma$ ) and dry friction ( $\mu$ ) coefficients for increasing pressure ratios. The dry friction coefficient ( $\mu$ ) decreases from  $P_r = 1.0$  to  $P_r = 1.7$  and increases for the higher pressure ratios (2.4 and 3.0). The reduction of the dry friction coefficient while applying a pressure differential of 10 psi (69 kPa,  $P_r = 1.7$ ) is attributed to the partial hydrostatic liftoff of the pads and reduction of the contact forces in between the bristles. On the other hand, as the pressure differential across the seal is further increased, the bristle-to-bristle and bristle-to-back plate contact force increase (compacting the bristle matrix), thus increasing the frictional dissipation and counteracting the friction reduction effect from the partial lift-off of the pads and the initial separation of the bristles. The loss factor ( $\gamma$ ) shows a decreasing trend as the supply pressure increases. This reduction may be associated to the repositioning (movement) of the bristles respect to each other, and the stiffening effect due to the pressure differential that pushes the bristle pack against the backplate.



**Figure 31 Loss factor ( $\gamma$ ) and dry friction ( $\mu$ ) coefficients for hybrid brush seal versus supply pressure to discharge pressure ratio ( $P_r$ )**

## CHAPTER IX

### LEAKAGE OF A HBS UNDER DYNAMIC LOADING CONDITION

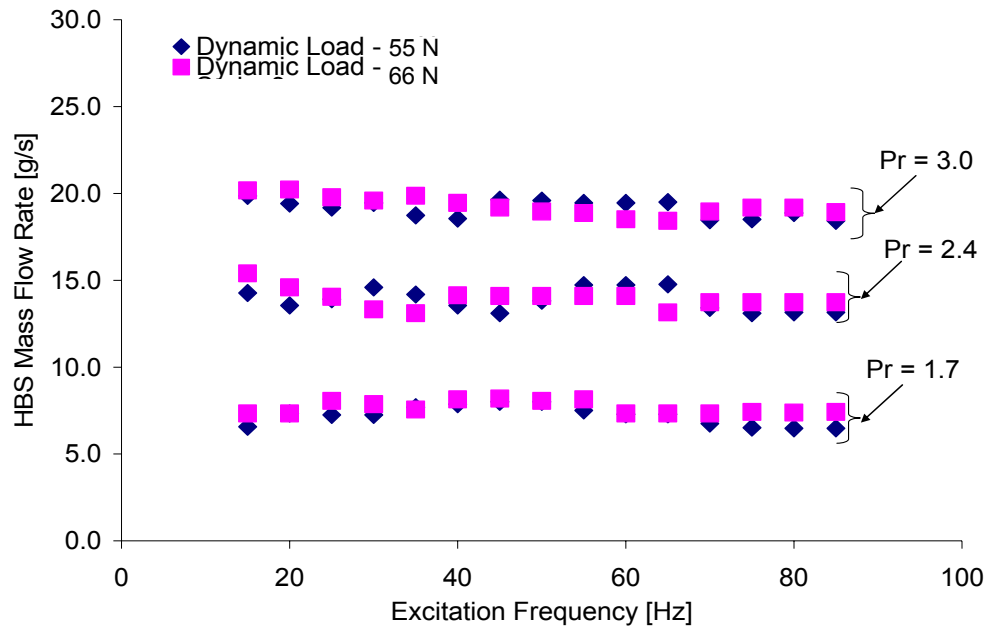
This chapter presents HBS leakage measurements while being excited by single-frequency unidirectional loads and for increasing supply pressures. The following leakage measurements were recorded while conducting the dynamic load tests. Dynamic leakage measurements are compared to static leakage measurements presented in Chapter IV. The tests are conducted without rotor spinning.

#### Experimental Procedure

A turbine flowmeter registers the leakage as described in Chapter IV for three supply pressures ( $P_s = 169, 238$  and  $307$  kPa), while applying the periodic excitation load following the procedure detailed in Chapter VIII.

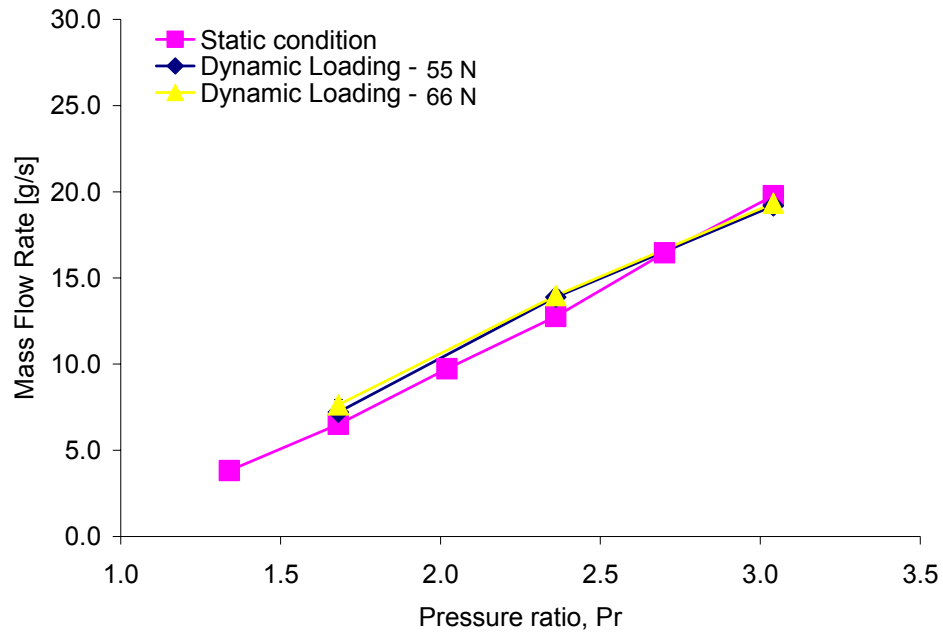
#### Experimental Results and Discussion

Figure 32 shows the mass flow rate versus the excitation frequency input into the test seal for two loads (55 N and 66 N) and for  $P_r = 1.7, 2.4,$  and  $3.0$ . The periodic excitation loads are kept constant throughout the test frequency range. Seal leakage remains constant for 55 N and 66 N throughout the test frequency range for each supply to discharge pressure ratio, therefore demonstrating that secondary flow across the HBS is not affected by the excitation frequency or load amplitude, but only by the pressure differential across the seal. A 66 N load induces HBS radial displacements of approximately 0.510 mm (0.020 in.) as it passes through the natural frequency (~58 Hz) of the equivalent test system without affecting its sealing performance or the seal structural integrity.



**Figure 32 HBS mass flow rate (leakage) versus excitation frequency (15 – 90 Hz) for increasing supply pressure to discharge pressure ratios ( $P_r$ ) no shaft rotation and upstream air temperature of 23°C**

Based on the results from the previous figure, the HBS mass flow rate can be expressed as a function of pressure ratio by averaging the measured leakage over the test frequency range. Figure 33 shows the average mass flow rate versus supply pressure to discharge pressure ratio for three conditions: static conditions and dynamic loading at 55 N and 66 N. The leakage curve under static conditions corresponds to the experimental results previously presented in Chapter IV. Secondary flow rate across a HBS shows no significant difference between static and dynamic loading conditions for increasing pressure ratios. The results indicate that the HBS will retain its superior sealing capacity under actual operating conditions; for example with large rotor excursions. The uncertainty associated with averaging leakage values from the test frequency range for 55 N and 66 N loads is rather low, for this reason error bars are not visible in this figure.



**Figure 33 HBS mass flow rate (leakage) versus supply pressure to discharge pressure ratio ( $P_r$ ) for single frequency excitation loads (55N and 66N), no shaft rotation and upstream air temperature of 23°C (frequency average)**

Figure 34 shows the predicted (single tooth labyrinth seal) effective clearance versus pressure ratio for a hybrid brush seal subjected to single-frequency dynamic loading excitation. The calculated effective clearance values obtained for 55 N and 66 N are compared to the ones obtained for leakage under static conditions. Results show that effective clearance for a HBS does not vary when subjected to an externally vibrating source, as demonstrated in Figure 32 as well.

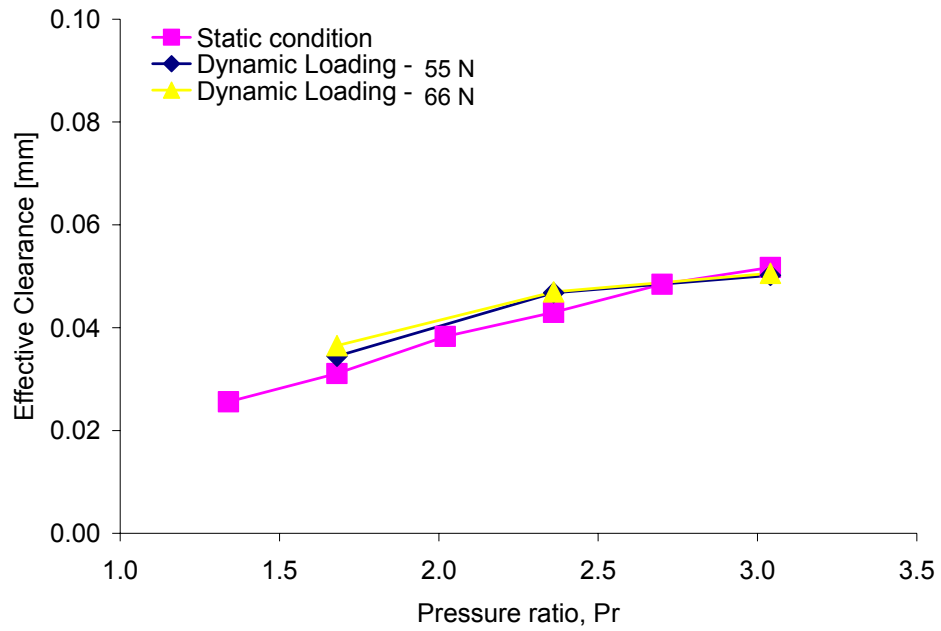


**Figure 34 Effective HBS clearance versus supply pressure to discharge pressure ratio ( $P_r$ ) for single frequency excitation loads (55N and 66N), no shaft rotation and upstream air temperature of 23°C**

## CHAPTER X

### LEAKAGE OF A HBS AT LOW ROTOR SPEEDS

#### Experimental Procedure

Figure 35 is a photograph of the test rig configuration used for the test with shaft rotation aiming to characterize the test seal leakage behavior and estimate the power loss and drag torque. The rotating tests are performed for a rotational speed ( $\Omega$ ) range of 400 to 1,300 rpm for three supply pressures ( $P_s = 169, 238$  and  $307$  kPa).  $P_r = 1.0$  indicates the seal is operating under *dry conditions*, with no external air pressurization. A turbine flowmeter located upstream of the test seal registers the leakage for three supply pressures ( $P_s = 169, 238$  and  $307$  kPa), at increasing rotor speed.

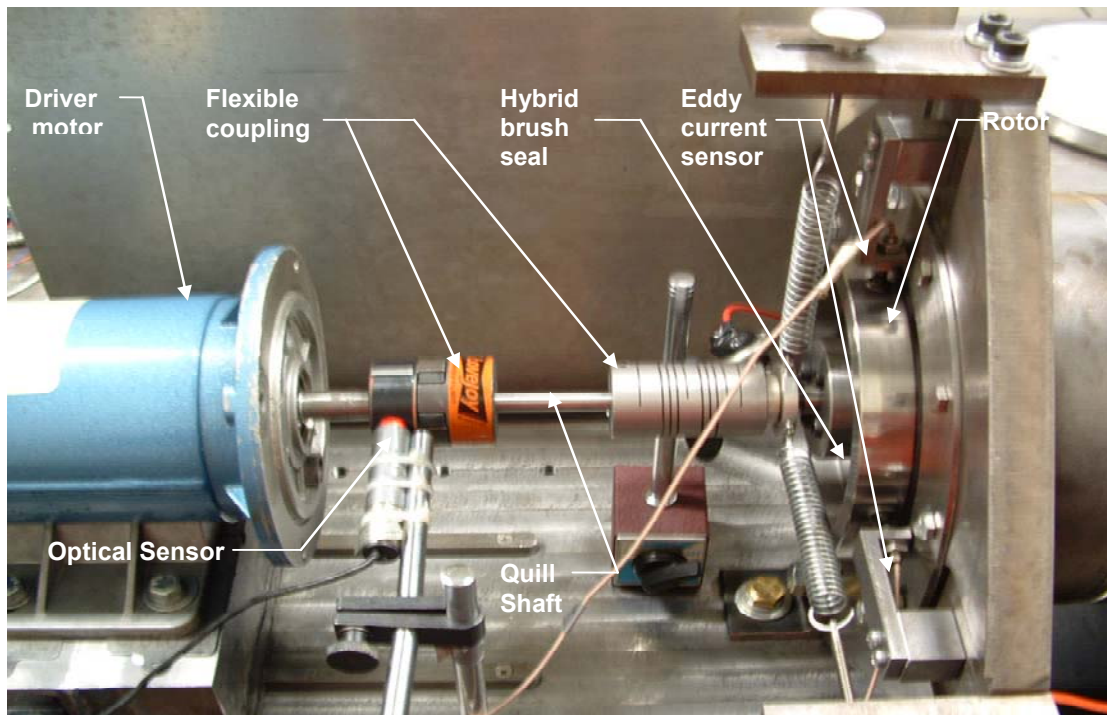
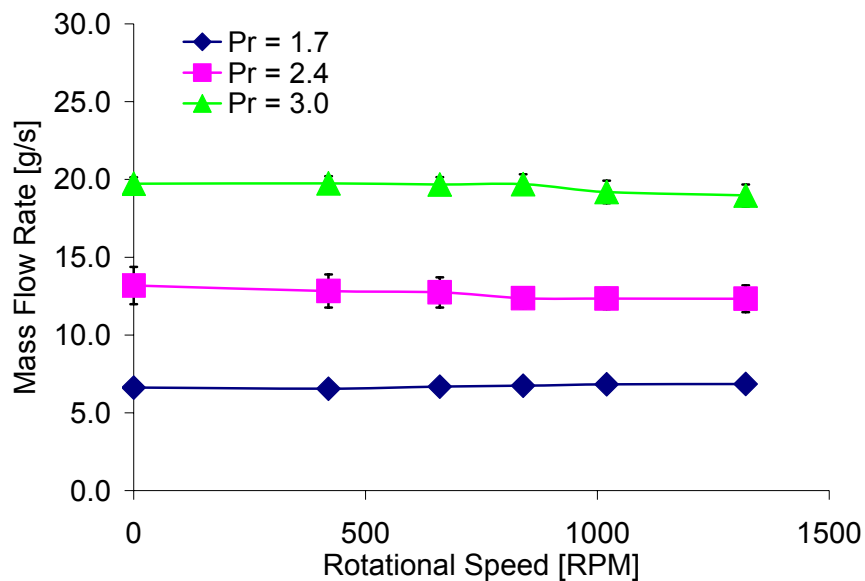


Figure 35 Photograph of rotordynamic test rig for a hybrid brush seal (HBS)

## Experimental Results and Discussion

Figure 36 displays the measured mass flow rate versus rotor speed for increasing pressure ratios ( $P_r = 1.7, 2.4, 3.0$ ). The initial leakage rate (at 0 rpm) for each supply pressure ( $P_s$ ) remains constant up to the maximum rotor speed tested, 1,300 rpm (21.6 Hz). Results indicate that HBS leakage rate over the test speed range is only dependent on the pressure differential across the seal.



**Figure 36 HBS mass flow rate (leakage) versus rotational speed for increasing supply pressure to discharge pressure ratio ( $P_r$ ) at an upstream air temperature of 23°C**

Figure 37 shows the measured mass flow rate versus pressure ratio ( $P_r$ ) for a HBS with air supplied at 23°C for three shaft speeds (0, 600 and 1,300 rpm). This figure shows that leakage rates for a HBS at 600 and 1,300 rpm are similar (i.e. less than 4% at  $P_r = 3.0$ ) to the ones measured with no rotation.



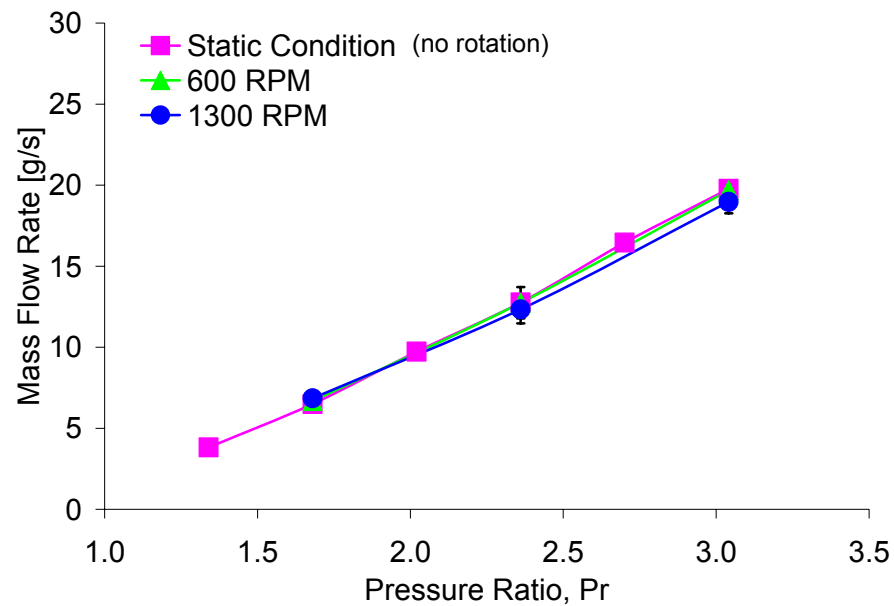


**Figure 37 HBS mass flow rate (leakage) versus supply pressure to discharge pressure ratio ( $P_r$ ) for static condition (no rotation) and shaft speeds (600 and 1,300 RPM)**

Figure 38 shows the test seal effective clearance versus pressure ratio ( $P_r$ ) for the HBS at 0, 600 and 1,300 rpm. The seal effective clearance for 600 and 1300 rpm is similar to the effective clearance predicted for leakage under no rotation, with maximum clearance just over 0.05 mm at  $P_r = 3.0$ . Typical operating clearances (diametral) for a labyrinth seal range from 1.0 to 2.0 mm [24], about 20 times higher than the calculated effective clearance for a HBS.

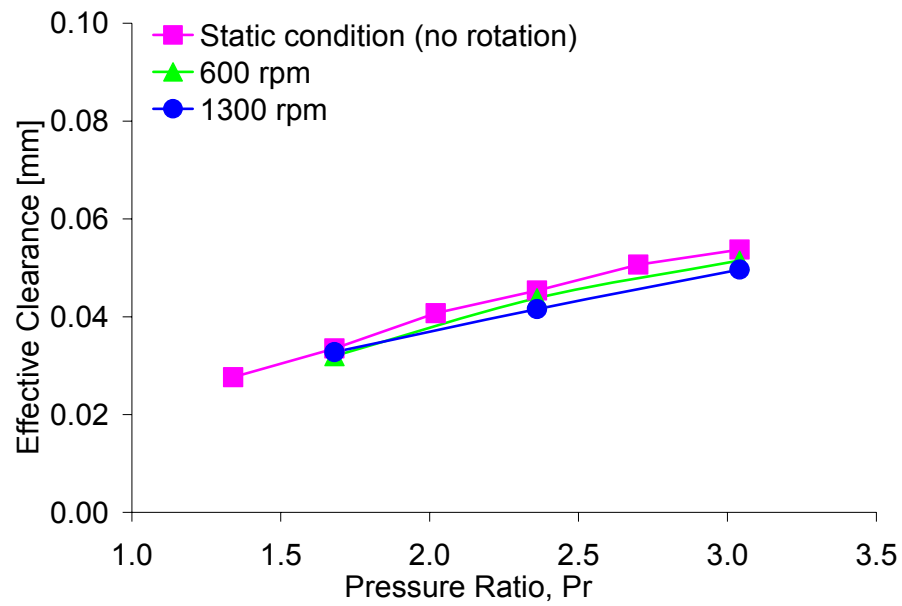


**Figure 38 Effective HBS clearance versus supply pressure to discharge pressure ratio ( $P_r$ ) for static condition (no rotation) and shaft speeds (600 and 1,300 RPM)**

## CHAPTER XI

### POWER LOSS AND DRAG TORQUE OF A HBS AT LOW ROTOR SPEEDS

In turbomachinery components such as bearings and seals, estimation of power loss and drag torque once the rotor spins is crucial to characterize their efficiency and performance under a variety of operating conditions (e.g. pressure and speed variations). HBS power loss and drag torque provide valuable insight on the interaction of pads and the rotor surface as the supply pressure increases. A description of the test procedure to estimate power loss and drag torque follows.

#### **Experimental Procedure**

The tests are performed on the rotating test rig (see Fig. 35) for a shaft speed ( $\Omega$ ) range of 400 to 1,300 rpm and three supply pressures ( $P_s = 169, 238$  and  $307$  kPa). Initially, the supply pressure  $P_s$  (upstream of the seal) is set manually until the desired pressure ratio is reached. Discharge pressure,  $P_d$ , is atmospheric 101 kPa (14.7 psia). In the case of  $P_r = 1.0$ , the seal is operated with no external pressurization.

The rotor speed ( $\Omega$ ) is increased to the maximum test speed (i.e. 1,300 rpm)<sup>2</sup> and then reduced to each target speed to avoid premature degradation of the rotor due to the friction between the seal pads and rotor when operating without external pressurization<sup>3</sup>, i.e.  $P_r = 1.0$ . An optical sensor measures the speed of the rotor. Multimeters display the voltage and current supplied to the motor by a DC source at each target speed to estimate the power, ( $P_e$ ) supplied to the motor. After the last voltage and current readings are recorded the motor is brought to rest and the supply pressure is shutoff. Drag torque is

---

<sup>2</sup> Drive motor power restriction

<sup>3</sup> Appendix F presents an evaluation of the rotor and seal conditions after completing the tests with shaft rotation.

estimated by dividing the electrical power supplied by rotational speed, i.e.  $T_d = \frac{P_e}{\Omega}$ .

Five trials were conducted and results correspond to average values of these trials.

The initial baseline power loss and torque are estimated prior to the installation of the HBS in the test rig. For this case the only source of friction drag arises from the roller bearings located at the base of the rotor assembly, see Fig. 9, and the motor rolling elements.

### **Experimental Results and Discussion**

Figure 39 shows the HBS power loss versus rotor speed for increasing pressure ratios with the baseline values (motor drag and disk windage) already subtracted. Test seal power losses are higher at  $P_r = 1.0$  due to the high contact forces (rubbing) at the rotor/seal interface. At the maximum shaft speed the power loss for no pressurization is about half a horsepower. Power losses for the HBS decrease about 90% from  $P_r = 1.0$  to 1.7 for the test speed range. Results for break-away torque presented in Chapter VII demonstrate that contact forces between the HBS pads and rotor are nearly eliminated as the supply pressure increases. HBS pads experience a “hydrostatic lift off” due to air passing across the seal reducing the initial dry friction at the seal/rotor interface. Consequently, the power loss for a HBS drops as a function of increasing supply pressure.

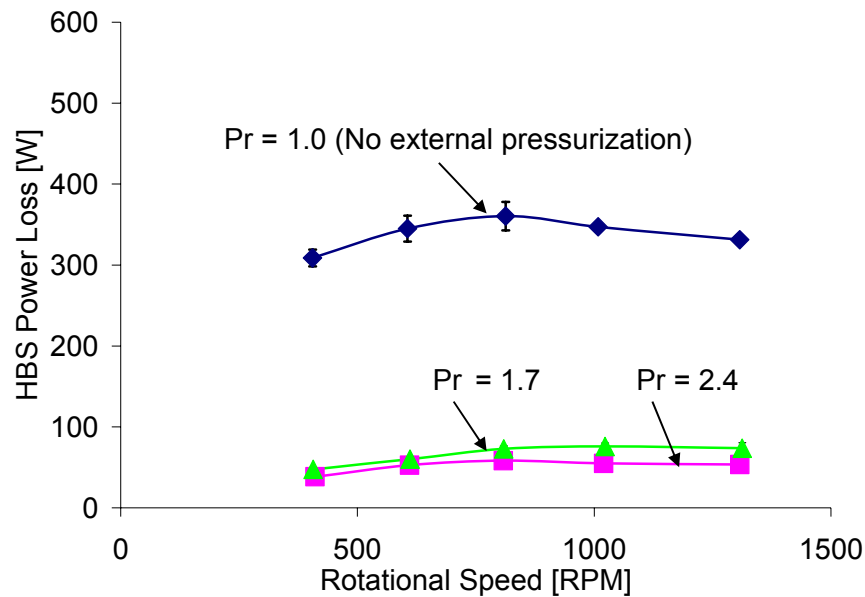


**Figure 39 Hybrid brush seal power loss versus rotational speed for increasing supply pressure to discharge pressure ratios ( $P_r$ )**

Figure 40 shows the estimated HBS drag torque versus rotor speed for increasing pressure ratios after subtracting the baseline values (motor drag and disk windage) obtained from spinning the rotor without the HBS in place. Baseline values are about one order of magnitude (i.e.  $\sim 0.37$  N-m) lower than the drag torque generated by the HBS. The break-away torque (with no external pressurization) is dominated by the dry friction resulting from the interference fit between the seal pads and the rotor. The drag torque decreases over 75% from  $P_r = 1.0$  to 1.7 for the test speed range. Analogous to the power loss measurements, drag torque results indicate that air passing across the HBS reduces the contact forces between the rotor and seal pads generating a hydrostatic gas film even before rotation starts. This effect is further enhanced by the hydrodynamic action due to rotor spinning. It is believed that this phenomenon will be more noticeable at higher rotational speeds. There is no significant change in drag torque from  $P_r = 1.7$  and 2.4, given that pads have already lifted-off the rotor surface with the initial external pressurization.

Note that at the end of the fifth trial at  $P_r = 1.0$ , there is a temperature increase of about  $15^\circ\text{C}$ , i.e. from  $23^\circ\text{C}$  to  $38^\circ\text{C}$ , at the rotor/seal interface at the maximum rotor speed ( $\sim 1300$  rpm). Conversely, for  $P_r = 1.7$  and  $2.4$ , the operating temperature at the rotor/seal interface remained constant ( $\sim 24^\circ\text{C}$ ) during the experiments; implying no intermittent contact between the rotor and seal pads.

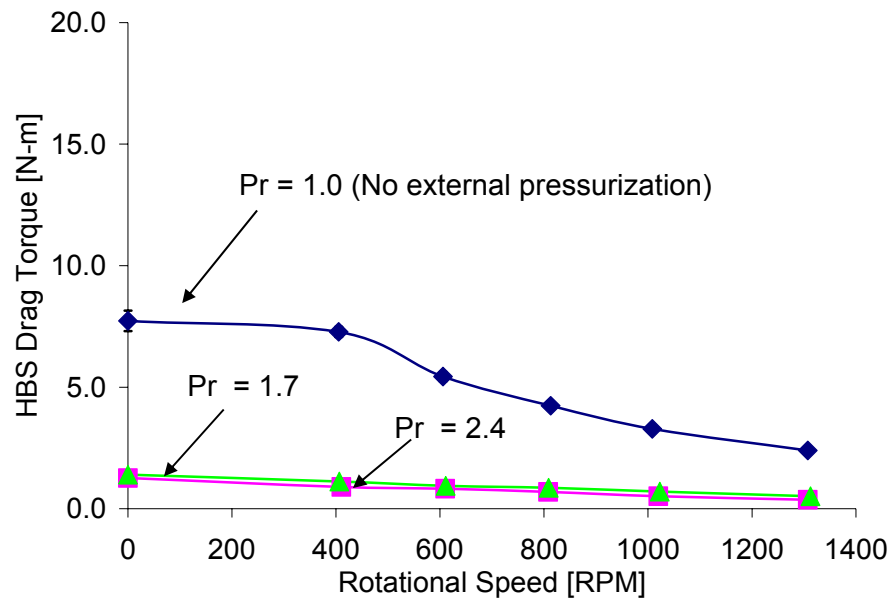


**Figure 40 Hybrid brush seal drag torque versus rotational speed for increasing supply pressure to discharge pressure ratios ( $P_r$ )**

## CHAPTER XII

### IDENTIFICATION OF ROTORDYNAMIC FORCE COEFFICIENTS OF A HBS FOR INCREASING SUPPLY PRESSURES

The experimental procedure and parameter identification method to estimate the rotordynamic force coefficients of a HBS follows. Identification of rotordynamic coefficients, specifically stiffness and damping, provide accurate estimation of the rotor-seal system forced response under various operating conditions (pressure, temperature, shaft speed).

#### **Experimental Procedure**

Prior to initiating the rotordynamic experiments, the supply pressure ( $P_s$ ) is manually adjusted to a desired value, similar to dynamic loading experiments. This pressure is measured at the inlet of the cylindrical steel vessel using a calibrated pressure sensor. Once the supply pressure is set, the motor is turned on, and the shaft speed adjusted to the desired value, 600 and 1,200 rpm, are considered.

Next, as the shaft spins at a constant speed, the electromagnetic shaker excites the test seal with a single frequency load (22N) from 20-80 Hz (3 Hz increments). The excitation load magnitude is maintained constant throughout the test frequency range. This procedure is followed for absolute supply pressures of 169 and 238 kPa (24.7 and 34.7 psia). Recall, that pressure ratio ( $P_r$ ) is defined as supply pressure ( $P_s$ ) over discharge pressure ( $P_d$ ), ( $P_r = \frac{P_s}{P_d}$ ). Figure 41 shows the reference coordinate system used for the rotordynamic tests. The  $X$ -direction is collinear with the periodic excitation load.

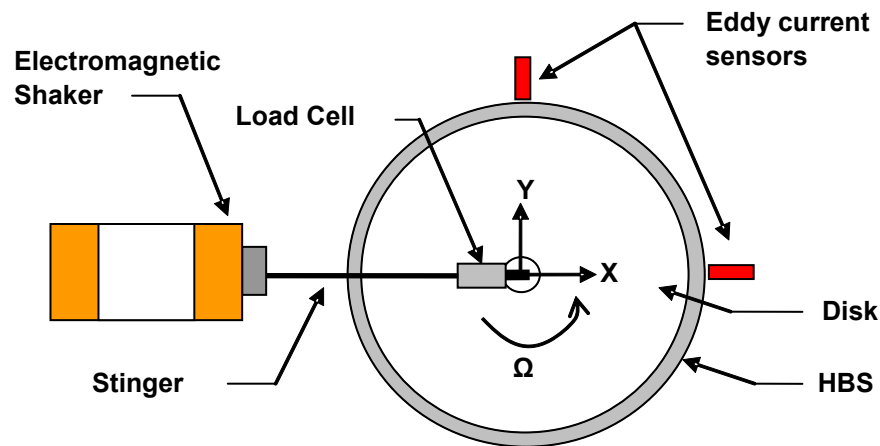


**Figure 41 Reference coordinate system for rotating tests with periodic external loading**

### Parameter Identification Method

The following model for identifying rotordynamic force coefficients in a HBS is based on the following assumptions:

- Rotor gyroscopic effects are negligible for the test rotor speeds selected (600 and 1,200 rpm)
- Rotor cross displacements ( $Y$ -direction) are much smaller than principal displacements ( $X$ -direction)
- Rotordynamic coefficients are identified for seal deflections measured at excitation frequencies ( $\omega$ )  $\neq$  rotor speed ( $\Omega$ )
- Seal is centered

Figure 42 depicts the waterfall plot for the system response in the  $X$  and  $Y$  directions. The system is excited with a periodic load of 22 N at a supply pressure of 167 kPa and constant shaft speed of 600 rpm (10 Hz). The rotor response is well defined for the range of frequencies tested. The response amplitude due to the unidirectional excitation increases as it approaches the test system natural frequency, i.e.  $\sim 32$  Hz. The system response in the  $Y$ -direction is much smaller (i.e. at least one order of magnitude) than that in the  $X$ -direction; thus indicating a minimal cross-



coupling effect. Similar behavior is shown at 1,200 rpm and 238 kPa absolute supply pressure.

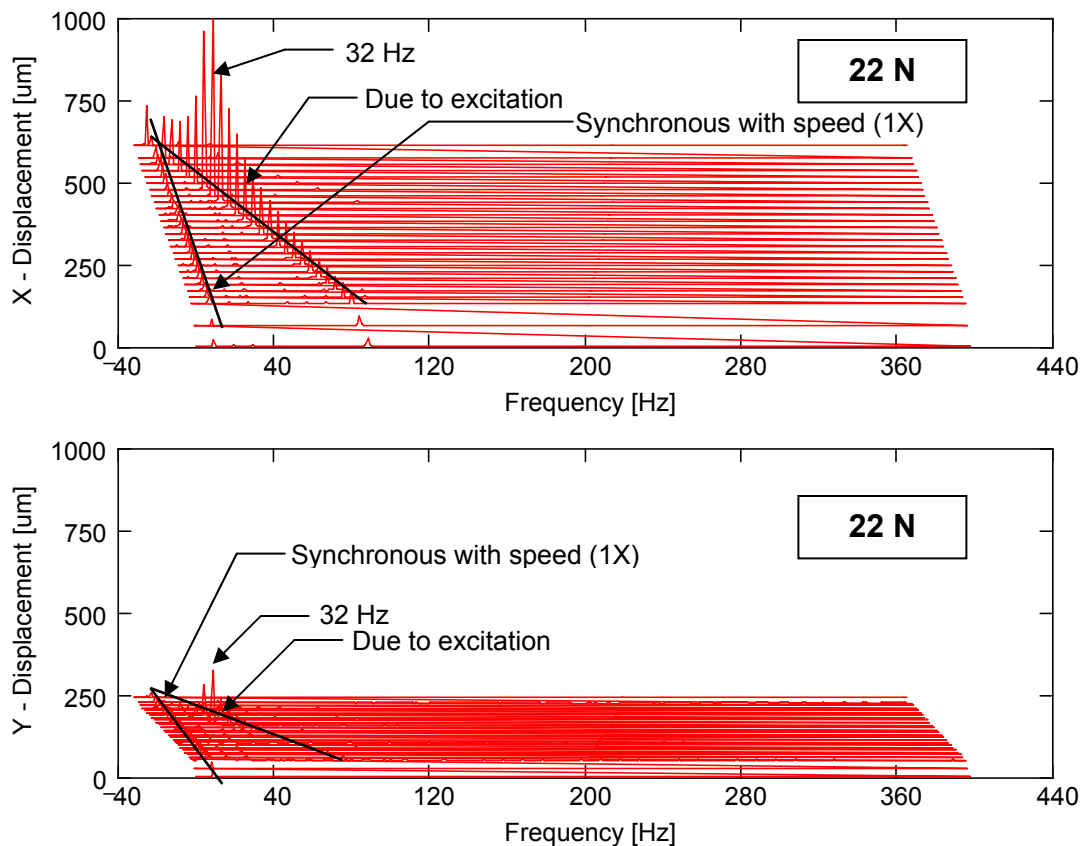


**Figure 42 Waterfalls of rotor displacements (X,Y) resulting from a periodic excitation load (22 N). Excitation frequency range of 20-90 Hz,  $P_r = 1.7$  and rotor speed: 600 rpm (10 Hz)**

A simple rotordynamic analysis of the test system performed in XLTRC<sup>2</sup> (rotordynamics software) shows that the dynamic forced response of the system is not significantly affected by gyroscopic effects at the test rotational speeds. Figure 43 shows the XLTRC<sup>2</sup> structural model of the cantilevered test rotor with an added stiffness (value used was obtained from static load test at  $P_r = 1.0$ ) at the seal location.

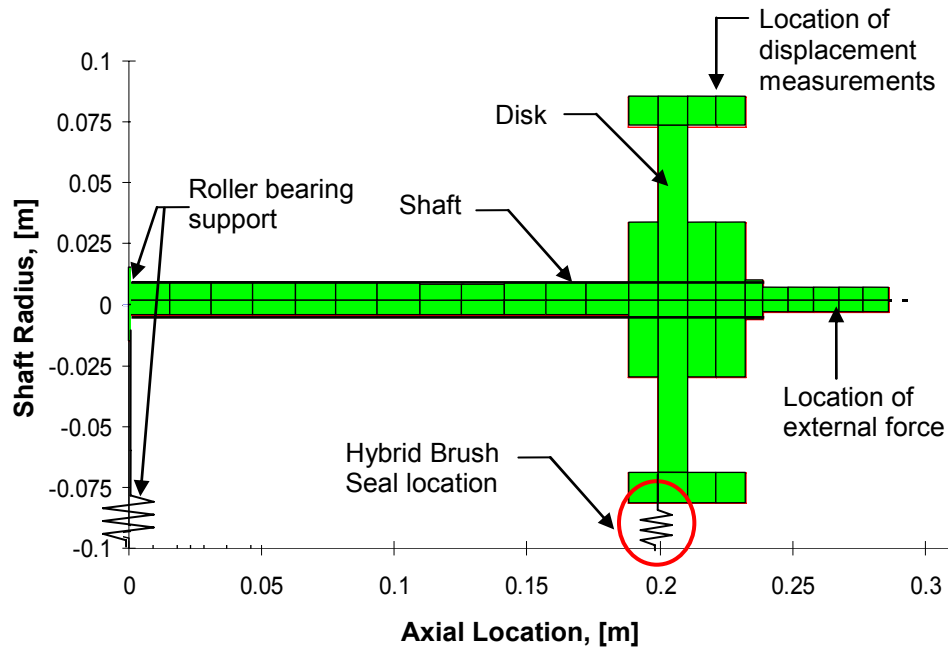


**Figure 43 Structural rotor model with location of HBS**

Table 9 shows the predicted natural frequencies (forward and backward modes) for the test system at increasing rotor speeds. The results show that the natural frequency of interest, i.e. first natural frequency (fundamental elastic mode), is not greatly influenced (less than 5% increase) by gyroscopic effects arising from the rotor geometry at the selected rotor speeds. Furthermore, Figure 42 shows small cross-coupling effects over the range of excitation frequency for the selected rotor speed. These findings allow reducing the degrees of freedom of the test system and enable the development of a simple model to identify the rotordynamic coefficients of the HBS.

**Table 9 Predicted natural frequencies (Forward and Backward) for test rotor with HBS in place (\*)**

Rotor Speed [RPM]	1 <sup>st</sup> Backward Nat. Frequency, [Hz]	1 <sup>st</sup> Forward Nat. Frequency, [Hz]	2 <sup>nd</sup> Forward Nat. Frequency, [Hz]	3 <sup>rd</sup> Forward Nat. Frequency, [Hz]
0	30.5	30.5	146	1351
600	29.7	31.4	154	1351
1200	28.8	32.2	163	1351

\* Predictions obtained with an assumed HBS stiffness equal to 118 kN/m (stiffness value from static loading tests - tapping condition).

Based on the afore mentioned assumptions, it is plausible to identify the HBS rotordynamic force coefficients by implementing an identification procedure similar to the one used for the dynamic load tests without shaft rotation. A brief description of the identification method follows.

The seal parameters are estimated from seal displacements induced by unidirectional single frequency forcing functions while the shaft spins at a constant rotational speed ( $\Omega$ ). The equations of motion of the test system are

$$\begin{bmatrix} M_{xx} & M_{xy} \\ M_{yx} & M_{yy} \end{bmatrix} \begin{Bmatrix} \ddot{x} \\ \ddot{y} \end{Bmatrix} + \begin{bmatrix} K_{xx} & K_{xy} \\ K_{yx} & K_{yy} \end{bmatrix} \begin{Bmatrix} x \\ y \end{Bmatrix} + \begin{bmatrix} C_{xx} & C_{xy} \\ C_{yx} & C_{yy} \end{bmatrix} \begin{Bmatrix} \dot{x} \\ \dot{y} \end{Bmatrix} = \begin{pmatrix} F_x \\ 0 \end{pmatrix} + \begin{pmatrix} F_{ix} \\ F_{iy} \end{pmatrix} \quad (14)$$

where  $\{M_{\alpha\beta}, K_{\alpha\beta}, \text{ and } C_{\alpha\beta}\}_{\alpha\beta=x,y}$  are the system mass, stiffness and damping coefficients, respectively.  $F_x$  represents the external excitation force (loading in the  $X$ -direction only) applied at frequency  $\omega$ .  $F_{ix}$  and  $F_{iy}$  are the imbalance forces having a fundamental frequency coinciding with the shaft speed,  $\Omega$ .

Rotordynamic coefficients in Eq. (14) are estimated from the applied force and resulting displacements ( $X$  and  $Y$  directions) measured at frequencies  $\omega \neq \Omega$ . Consequently, expressing Eq. (14) in terms of the components with the main excitation frequency (i.e.  $\bar{x} = xe^{i\omega t}$ ,  $\bar{y} = ye^{i\omega t}$  and  $\bar{F} = Fe^{i\omega t}$ ) yields

$$Z_{xx} \cdot \bar{x} + Z_{xy} \cdot \bar{y} = \bar{F}_x \quad (15)$$

$$Z_{yx} \cdot \bar{x} + Z_{yy} \cdot \bar{y} = 0 \quad (16)$$

where  $Z_{\alpha\beta} = \{K_{\alpha\beta} - M_{\alpha\beta}\omega^2 + iC_{\alpha\beta}\omega\}_{\alpha\beta=x,y}$  represent the test system impedances. For small rotor displacements about a seal centered position it is reasonable to assume that  $Z_{xx} = Z_{yy}$  and  $Z_{xy} = -Z_{yx}$ . Based on these assumptions, the direct and cross-coupling coefficients are readily identified using the amplitude and phase information from the transfer function corresponding to the response of the system at the frequency of interest ( $\omega \neq \Omega$ ).

From Eq. (16), the cross-coupled impedance  $Z_{xy}$  is expressed in terms of  $Z_{yy}$  as

$$Z_{yx} = -Z_{yy} \frac{\bar{y}}{\bar{x}} \quad (17)$$

with  $Z_{xy} = -Z_{yx}$ , the direct impedance  $Z_{xx}$  becomes

$$Z_{xx} = \frac{\bar{F}_x \cdot \bar{x}}{(\bar{x}^2 + \bar{y}^2)} \quad (18)$$

Results show that cross-coupled force coefficients identified from rotordynamic tests under pressurized conditions will be predominantly due to fluid film forces within the seal induced by shaft rotation, i.e.  $Z_{xy} = -Z_{yx}$ .

### Experimental Results and Identified Rotordynamic Force Coefficients

Table 10 shows the direct stiffness ( $K_{xx}$ ) and mass ( $M_{xx}$ ) coefficients for the test system and corresponding HBS stiffness ( $K_s$ ) for increasing supply pressures and rotor speeds identified from the real part of  $Z_{xx} = \frac{\bar{F}_x \cdot \bar{x}}{(\bar{x}^2 + \bar{y}^2)}$ . The identified HBS stiffness

varies with increasing rotor speed and supply pressure. Results show that the direct dynamic system stiffness ( $K_{xx} = K_{yy}$ ) and the resulting HBS stiffness ( $K_s$ ) decrease approximately 15% as the rotor speed increases from 600 to 1,200 rpm for  $P_r = 1.7$ , and 5% for  $P_r = 2.4$ . Stiffness variations as a function of rotor speed indicate that cross-coupling effects in the HBS are not due to structural factors, but to hydrodynamic fluid film forces.

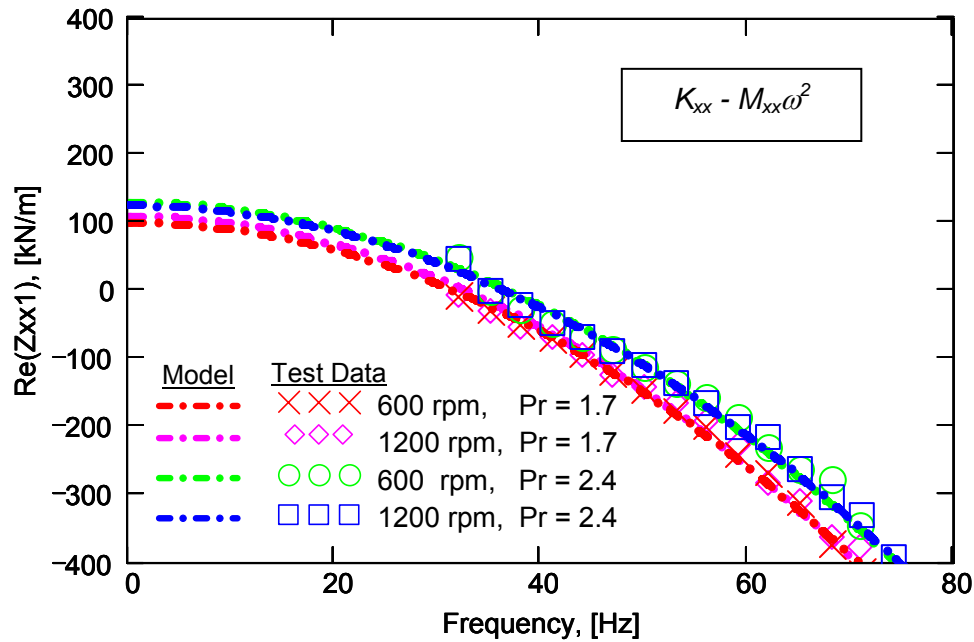
Additionally, the dry friction ( $\mu$ ) and loss factor ( $\gamma$ ) coefficients identified from the imaginary part of the test data and the energy dissipation method described in Chapter VIII show little variation with rotor speed for  $P_r = 1.7$  and 2.4. The direct stiffness coefficients identified from the rotating tests show a similar increasing trend with pressure (for both shaft speeds, i.e. 600 and 1,200 rpm) when compared to the equivalent system stiffness identified from the dynamic load tests without rotation, see Table 7.

**Table 10 Identified test system direct force coefficients from rotordynamic tests (Load 22 N, 20 Hz to 80 Hz, rotating test rig configuration) for increasing pressure ratios ( $P_r$ )**

	Direct-coefficients				
	$Z = \frac{\bar{F}_x}{\bar{x}} *$	$Z_{xx} = \frac{\bar{F}_x \cdot \bar{x}}{(\bar{x}^2 + \bar{y}^2)}$			
Pressure ratio	$P_r=1.0$	$P_r=1.7$		$P_r=2.4$	
Rotor Speed [rpm], $\Omega$	0	600	1200	600	1200
Stiffness [kN/m], $K_{xx}$	120	108	98	130	124
Mass [kg.], $M_{xx}$	1.11	2.62	2.54	2.43	2.39
$R^2$ (correlation factor)	0.97	0.98	0.98	0.98	0.98
Dynamic stiffness ( $K_{xx} - M_{xx}\omega^2$ )					
Natural Frequency [Hz], $\omega$	52.3	32.5	31.1	36.6	36.3
HBS stiffness[kN/m], $K_s$	93	103	89	135	128
HBS Dry Friction coefficient, $\mu$	0.66	0.39	0.36	0.37	0.38
HBS Loss Factor coefficient, $\gamma$	0.42	0.29	0.26	0.33	0.34

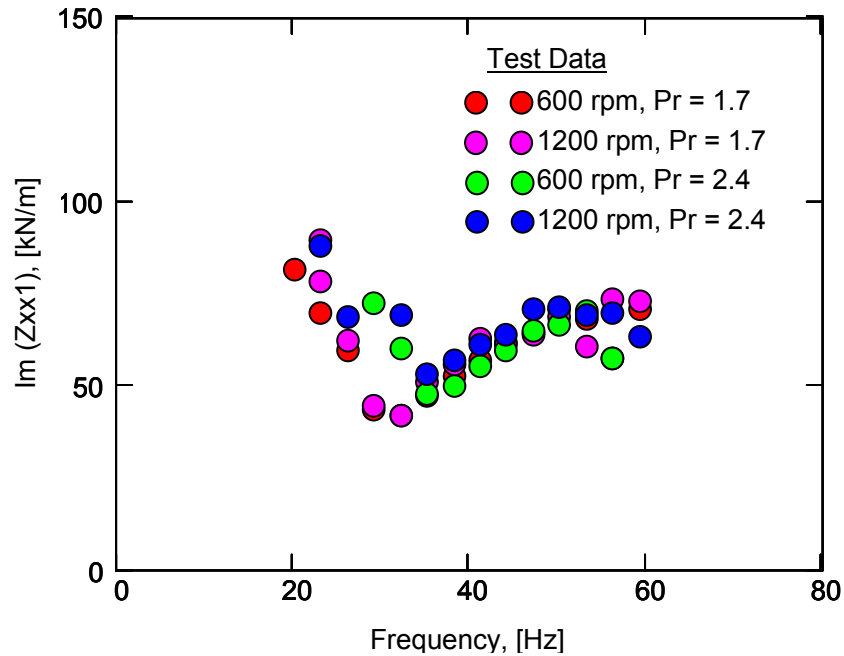
\* Coefficients identified from tests performed in non-rotating test rig.

Figure 44 depicts the real part of the test system impedance  $\text{Re}(Z_{xx})$  obtained from rotordynamic tests for an excitation load of 22 N. This figure illustrates the good correlation between test data (force and displacement) and the curve fit generated by the identified force coefficients from Table 10.



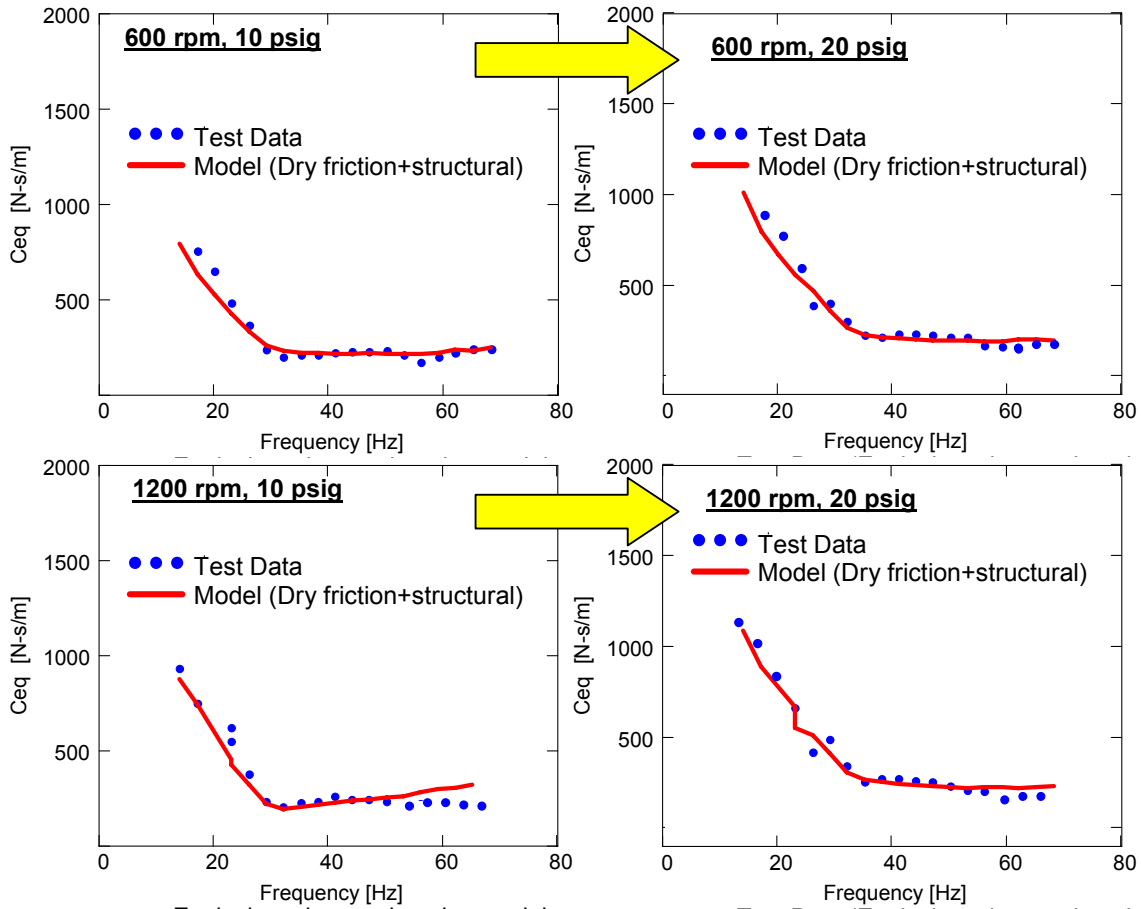
**Figure 44 Identified system rotordynamic stiffness versus frequency. Load magnitude = 22 N, for increasing supply pressure to discharge pressure ratios ( $P_r$ ) and rotor speeds**

Figure 45 depicts the imaginary part for the test system impedance,  $\text{Im}(Z_{xx})$ , versus excitation frequency for an excitation load of 22N and increasing supply to discharge pressure ratios and rotor speeds. Results from the dynamic load tests without shaft rotation show that the HBS damping is due to a contribution of Coulomb damping and structural damping represented by a dry-friction coefficient ( $\mu$ ) and loss factor ( $\gamma$ ), respectively (see Figures 24 and 25). Similarly, for the dynamic load tests with shaft rotation the imaginary part of the impedance decreases to a minimum at the natural frequency ( $\sim 32$  Hz). The imaginary part shows no considerable variation for both pressure ratios and rotor speed conditions tested.



**Figure 45 Imaginary part of system impedance versus excitation frequency. Load magnitude = 22 N, for increasing supply pressure to discharge pressure ratios ( $P_r$ ) and rotor speeds**

Dry-friction coefficient ( $\mu$ ) and loss factor ( $\gamma$ ) are derived following the same procedure presented for dynamic load tests without shaft rotation. Figure 46 shows the relation between the test data and the results from the combined dry-friction and structural model. The identified equivalent viscous damping behaves similar for all four cases, decreasing to a minimum value at the test system natural frequency ( $\sim 32$  Hz) and then remaining approximately constant for the remaining excitation frequency range. Analogous to the results obtained from the dynamic load tests without shaft rotation, the results from Figure 46 are typical for a structure with dry friction damping.



**Figure 46 Test data and identified equivalent viscous damping for increasing rotor speeds (600 and 1200 rpm) and increasing pressure ratios ( $P_r = 1.7$  and 2.4)**

Table 11 shows the identified cross-coupled force coefficients ( $K_{xy} = -K_{yx}$ ) from rotordynamic tests at increasing supply pressures. Results indicate that the cross-coupled mass values are nearly 0 kg and in some instances slightly negative; thus indicating that the equivalent cross-coupled dynamic stiffness is independent of excitation frequency. By modifying the rotordynamic identification model (i.e. assuming a 0 kg cross-coupled mass) the cross-coupled stiffnesses for  $Z_{xy} = -Z_{yx}$  is approximated by an average stiffness value throughout the test frequency range, see Figure 47. Cross-coupled stiffness drops approximately 50% as the rotor speed increases from 600 to 1,200 rpm for both test supply pressure conditions. In addition, identified cross-coupled stiffness values are



considerably smaller (up to one order of magnitude) than the identified direct coefficients.

**Table 11 Identified test system cross-coupled force coefficients from rotordynamic tests (Load 22 N, 20 Hz to 80 Hz, rotating test rig configuration) for increasing pressure ratios ( $P_r$ )**

Cross-coefficients				
$Z_{xy} = -Z_{yx} = Z_{xx} \frac{\bar{y}}{\bar{x}}$				
(non-structural cross-coupling)				
Pressure ratio*	$P_r=1.7$		$P_r=2.4$	
Rotor Speed [rpm], $\Omega$	600	1200	600	1200
Stiffness [kN/m], $K_{xy}$	8.8	15	2.7	6.6
Mass [kg.], $M_{xy}$	0	0	0	0
$R^2$ (correlation factor)				
Dynamic stiffness ( $K_{xy} - M_{xy}\omega^2$ )	0.12	0.10	0.20	0.12

Figure 47 shows the real part of the cross-coupled impedances values shown in Table 11. As mentioned previously, the mass coefficients are zero for all test conditions, and cross-coupled stiffness is averaged value along identification frequency range. For this specific rotordynamic analysis assuming small rotor motions about a centered seal the force coefficients are  $Z_{xy} = -Z_{yx}$  (non-structural cross-coupling).

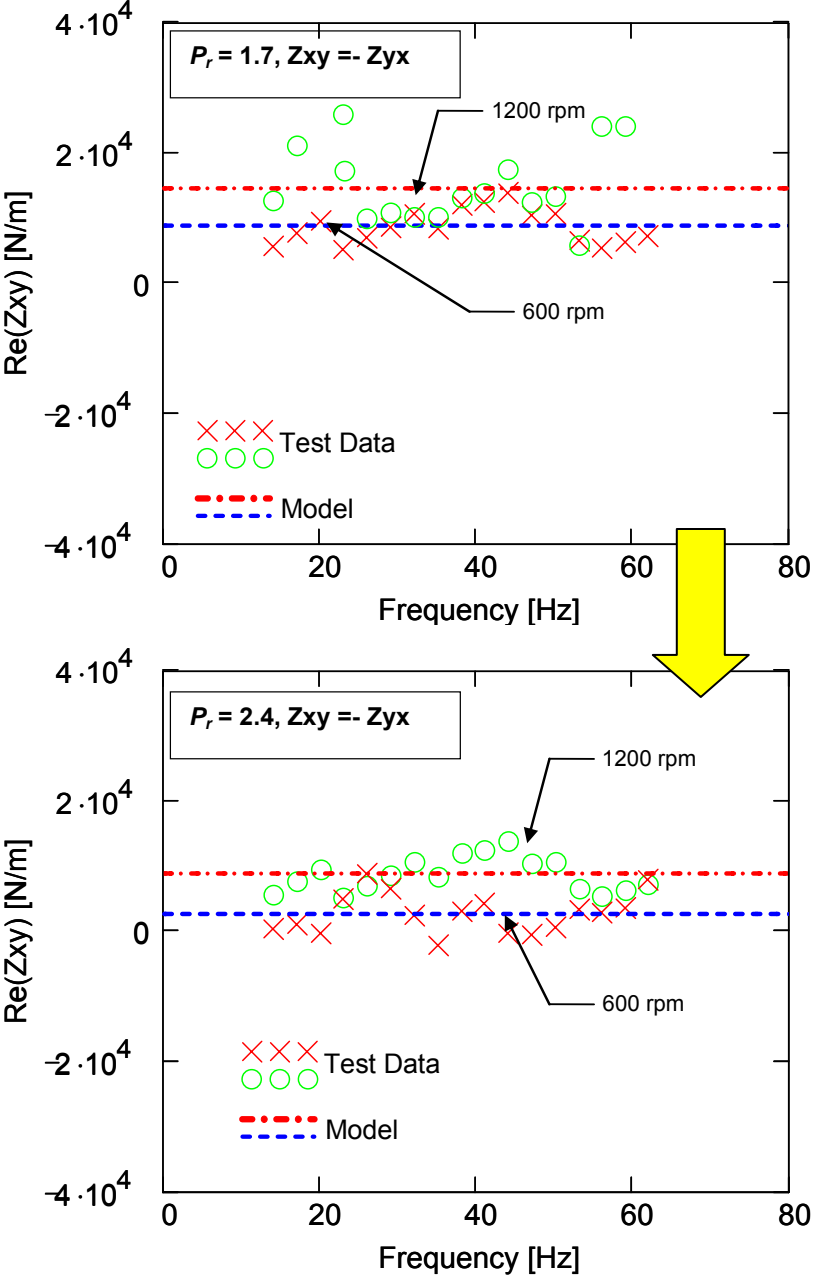


Figure 47 Average cross-coupled stiffness ( $K_{xy}$ ) for increasing rotor speeds (600 and 1,200 rpm) and increasing supply to discharge pressure ratios,  $P_r$

## CHAPTER XIII

### PREDICTIONS OF ROTORDYNAMIC FORCE

#### COEFFICIENTS OF A HBS

Rotordynamic force coefficients for a HBS are obtained using a computational model, TPGASBEAR®, developed by Delgado et al. [19]. The code finds the static and dynamic forced response of flexibly mounted, multiple pads gas bearings or gas seals. A visual graphic interface in MSEXCEL® sets and controls the input data and output values.

The non-synchronous force coefficients (stiffness and damping) are predicted for a range of excitation frequencies ( $\omega$ ) while keeping a constant rotor speed ( $\Omega$ ) and supply pressure. The force coefficients predictions assume the HBS is at a centered position. For this condition, the principal force coefficients are identical, and cross-coupled coefficients are anti-symmetric, e.g. the stiffness coefficients  $K_{sxx} = K_{syy}$  and  $K_{sxy} = -K_{syx}$ , respectively. In addition, the visual interface creates graphs of the results, i.e. stiffness and damping coefficients versus excitation frequency.

Figure 48 shows the schematic view and reference coordinate system for the multiple pads seal model used by the program.

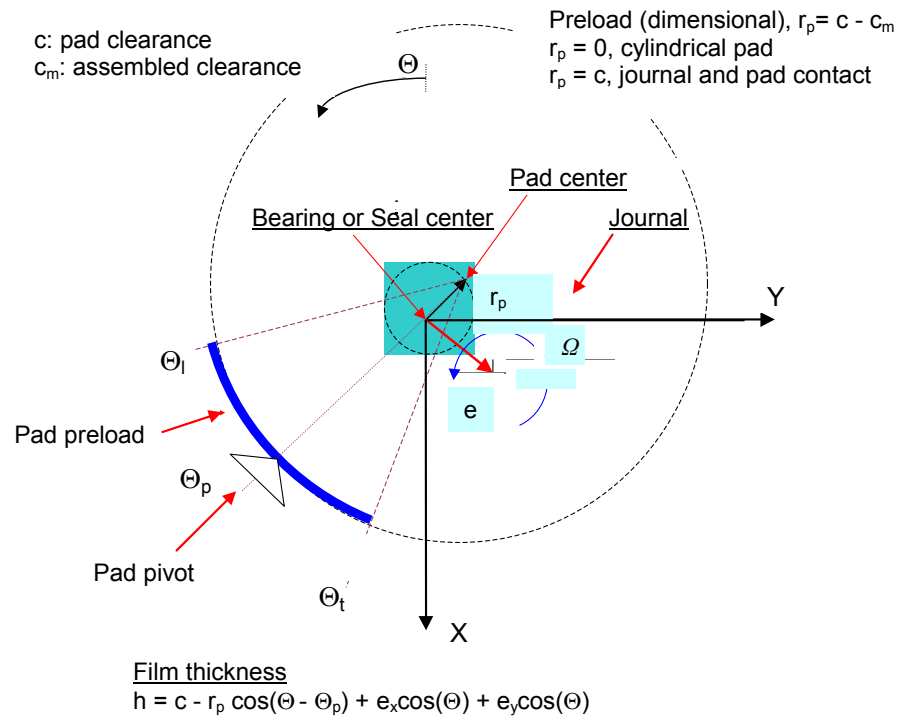


**Figure 48 Schematic view and reference coordinate of multiple pad seal [19]**

Figure 49 depicts the visual graphic interface of the computer program with the seal input values and fluid properties, as well as the predicted force coefficients.

<b>XLTPGASBEAR™ Spreadsheet for hydrodynamic tilting pad GAS bearings &amp; seals</b>								
Version 1.0, Copyright 2002 by Texas A&M University. All rights reserved. Dr. Luis San Andres								
Title:	GAS SEAL BEARING							
PHYSICAL Units	S.I.	L/D	0.02660084					
<b>ISOTHERMAL MODEL</b>		<b>CONVERGENCE PARAMETERS</b>						
Rotor Diameter	0.1671	meters	Max Iterations - film lands	500				
Axial Length	0.0044	meters	error pressure film lands	0.0000001				
Radial Clearance	5.00E-06	meters	Pad length	0.026				
Number of pads on bearing	20		GRID RATIO (circ/Axial)	3.69				
Pad 1 - arc length	18.00		No. Circ. Grid Points	17				
Pad 1 -leading edge	171.00		No. Axial Grid Points	11				
Preload	0.00		X Static Eccentricity Ratio	0				
Pad 1 - offset (% arc length)	0.50		Y Static Eccentricity Ratio	0				
<b>Fluid Properties</b>		<b>Frequency Analysis Option</b>						
Gas Constant	286.7	J/kg-C	Constant Shaft Rpm	600 rpm				
Supply Temperature	25	C	Nonsynchronous Analysis					
Viscosity at TS, Pexit	1.85E-02	c-Poise						
Density at TS, Pexit	1.20E+00	kg/m3						
loss factor	0.55	For HBS structural damping						
Fixed Eccentricity	Select Analysis Type							
<b>Tilting Pads</b>		<b>OPTION - TILTING PAD?</b>						
1.34E-03	Pad mass	kg						
7.69E-06	Pad Inertia	kg-m2						
<b>PAD Stiffness Matrix</b>		<b>PAD Stiffness (Imaginary) Matrix</b>						
Moment	1	0	0					
normal F	0	1.10E+04	0					
transverse F	0	0	1.00E+00					
Moment	0.55	0	0					
normal F	0	6050	0					
transverse F	0	0	0.55					
P Supply bars	P Exit bars	Load-X N	Load-Y N	Speed rpm	Kxx N/m	Kxy N/m	Cxx N-s/m	Cxy N-s/m
1.70E+00	1.00E+00	0	0	999	6.74E+04	1.97E+03	7.17E+02	1.48E+01
1.70E+00	1.00E+00	0	0	1498	8.13E+04	2.63E+03	4.61E+02	8.20E+00
1.70E+00	1.00E+00	0	0	1997	8.77E+04	3.30E+03	3.36E+02	3.47E+00
1.70E+00	1.00E+00	0	0	2496	9.13E+04	3.79E+03	2.65E+02	1.56E+00
1.70E+00	1.00E+00	0	0	2995	9.38E+04	3.35E+03	2.19E+02	6.17E+00
1.70E+00	1.00E+00	0	0	3494	9.60E+04	1.96E+03	1.87E+02	7.31E+00
1.70E+00	1.00E+00	0	0	3993	9.76E+04	8.09E+02	1.62E+02	5.80E+00

**Figure 49 Visual graphical user interface for calculation of rotordynamic force coefficients [19]**

Figure 50 shows the predicted HBS stiffness coefficients ( $K_{sxx} = K_{syy}$ ) versus excitation frequency (20-100 Hz) at constant rotor speed of 600 and 1,200 rpm, and two supply to discharge pressure ratios,  $P_r = 1.7$  and 2.4. The radial clearance input into the code corresponds to the effective clearance derived from the measured seal leakage, see Chapter IV. Predictions indicate that increasing the supply to discharge pressure ratio,  $P_r = P_s / P_d$ , has a negligible effect on the HBS direct stiffness,  $K_{sxx}$ . The direct seal stiffness remains approximately constant,  $K_{sxx} \sim 110$  kN/m, along the excitation frequency range. The magnitude of  $K_{sxx}$  is comparable to the measured seal structural stiffness,  $K_s$  ( $\sim 103$  kN/m), thus denoting dominance of the pads compliance effect with respect to the gas film thickness (i.e., the gas film is much stiffer than HBS pads). The predicted cross-coupled stiffness ( $K_{sxy} = -K_{syx}$ ) is at least one or two orders of magnitudes

less than the direct stiffness, thus not shown for clarity. For reference, the dashed line represents the HBS seal stiffness (frequency independent),  $K_s \sim 108$  kN/m, identified from the rotordynamic test results at  $P_r = 1.7$ . The direct HBS stiffness,  $K_{sxx}$ , drops approximately 10% as the speeds increases to 1,200 rpm while showing no dependence on the excitation frequency. The test results validate the code predictions for operation at rotor speeds of 600 and 1,200 rpm.

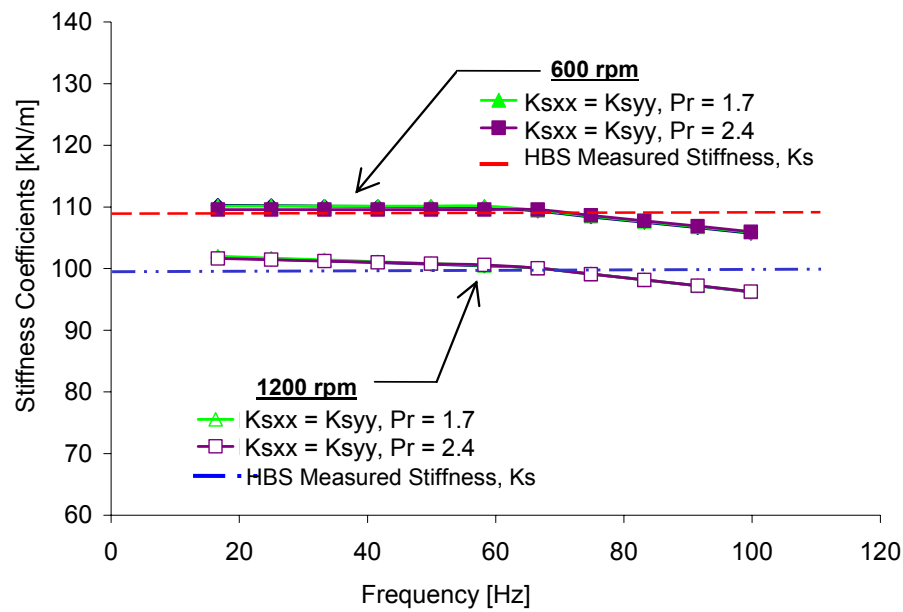


**Figure 50 Predicted non-synchronous HBS stiffness coefficients versus excitation frequency at two supply to discharge pressure ratios,  $P_r = 1.7$  and 2.4. Rotor speed: 600 rpm (10Hz) and 1200 rpm (20Hz)**

Figure 51 shows the predicted HBS viscous damping coefficients versus ( $C_{sxx} = C_{syy}$ ) excitation frequency and for a constant rotor speed, 600 and 1,200 rpm, and two supply-to-discharge pressure ratios,  $P_r = 1.7$  and 2.4. The computational model implements a user-given loss factor coefficient ( $\gamma$ ). The loss factor coefficient largely determines the HBS viscous damping. Predictions indicate that the HBS direct damping coefficients,  $C_{sxx} = C_{syy}$ , decay with increasing excitation frequency.  $C_{sxx}$  increases as a function of increasing structural loss factor coefficient ( $\gamma$ ); which accounts for the hysteretic effect of the bristle bed. This figure also includes the equivalent viscous damping ( $C_{eq} \sim C_{sxx}$ ) derived using the test data obtained from the rotordynamic experiments. The loss factor ( $\gamma$ ) and dry friction ( $\mu$ ) identified from  $C_{eq}$  range between 0.20 to 0.45 and 0.35 to 0.69, respectively. The magnitude of the HBS equivalent viscous damping decays rapidly as it reaches the natural frequency of the system ( $\sim 32$  Hz). This behavior is typical of systems with dry friction; therefore implying that at the natural frequency the loss factor coefficient ( $\gamma$ ) contributes to the vast majority of the seal damping  $C_{eq}$  remains approximately constant from 35 to 60 Hz. The magnitude of the predicted HBS direct damping coefficients,  $C_{sxx} = C_{syy}$ , at 1,200 rpm are approximately equivalent to those predicted for the 600 rpm rotor speed. The viscous damping coefficients predicted for both rotor speeds, show minimal dependence on increasing pressure ratio.

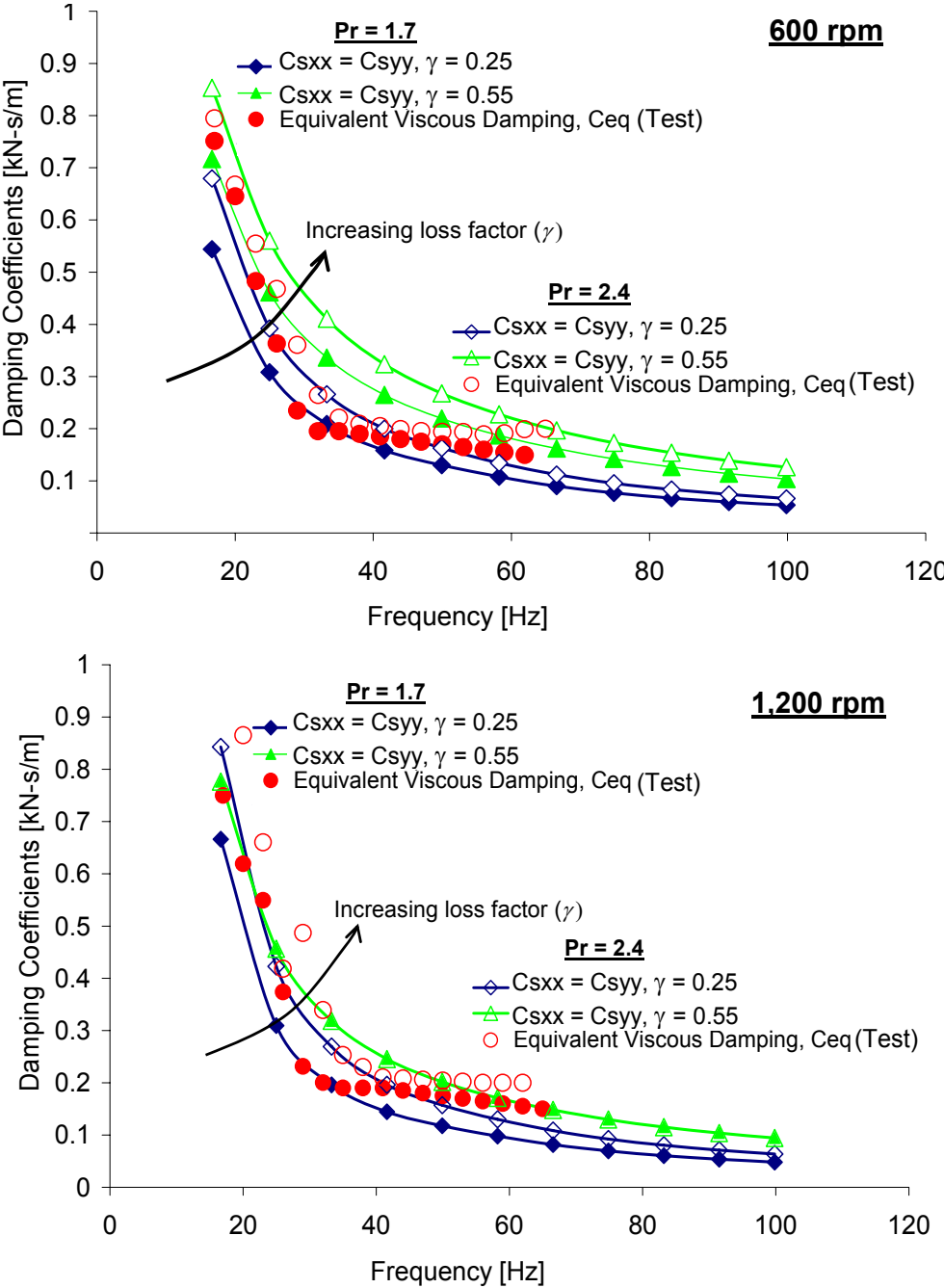


Figure 51 Predicted HBS viscous damping coefficients versus excitation frequency. Rotor speeds: 600 (10Hz) and 1,200 rpm (20Hz) and supply to discharge pressure ratio,  $P_r = 1.7$  and 2.4



## CHAPTER XIV

### CONCLUSIONS AND RECOMMENDATIONS

The hybrid brush seal [21] represents a 2<sup>nd</sup> generation of shoed-brush seals. Hybrid brush seals offer advantages when compared to labyrinth seals in terms of leakage, power loss and dynamic forced performance [6]. In addition, the HBS design is intended to overcome the main deficiencies found in conventional brush seals; such as excessive rotor and seal wear due to sustained contact between these two components, low pressure differential sealing capacity and unidirectional rotation.

This thesis presents laboratory results that quantify the leakage, power loss performance, and characterize the static and dynamic forced behavior of a HBS. The results provide physical insight on this novel sealing technology, validate predictive engineering models, and further the knowledge available for this component.

Power loss and drag torque measurements performed on a HBS at low rotor speeds (<11 m/s at 1,300 rpm) reveal a significant dependence on the pressure differential across the seal. Maximum power loss (~350W) for the test seal occurs at  $P_r = 1.0$  (no external air pressurization). This is due to the contact forces (rubbing) between the rotor and seal pads prior to pressurization. The power loss show no major variation with rotor speed. As the supply pressure increases, i.e. at  $P_r = 1.7$ , power loss drops about 90% evidencing the presence of a hydrodynamic pressure film between the seal pads and the rotor, therefore eliminating the contact forces prevalent between these components at  $P_r = 1.0$ . Consequently, drag torque decreases substantially (~75%) from  $P_r = 1.0$  to  $P_r = 1.7$ . As mentioned previously, frictional forces prevalent at  $P_r = 1.0$  between seal pads and rotor are nearly eliminated due to the lift off effect experienced by the pads as the supply pressure and rotor speed increases. Most importantly, the break away (static) torque drops by more than 50% as the HBS is pressurized, thus indicating that seal pads liftoff prior to actual shaft rotation. The hydrostatic lift-off effect is further enhanced by the hydrodynamic action caused by rotor spin. Thus, when pressurized, the HBS drag

torque is lowest at rotor startup and steady operating conditions, a finding in direct opposition to that of typical brush seals. Additionally, the operating temperature at the rotor/seal interface remains almost constant ( $\sim 24^{\circ}\text{C}$ ) during tests with shaft rotation (power loss and drag torque measurements) under pressurized conditions ( $P_r = 1.7$  and  $2.4$ ) demonstrating the rotor and seal pads are not in contact.

Flow rate measurements reveal a better sealing performance of the HBS with respect to the 1<sup>st</sup> generation shoed-brush seal. HBS leakage decreased approximately 36% overall of the test supply pressure range. A reduction in the empirically calculated effective clearance (represents a single tooth laby seal) of the hybrid brush seal reveals its enhanced sealing capability when compared to the typical diametral clearance of labyrinth seal [24]. Additionally, the EDM spring lever elements that connect the pads to the seal casing in a HBS effectively restrict the axial tilting motions of the pads preventing sudden changes in the flow area; which will consequently increase leakage rates.

Static load tests at increasing supply pressures allow characterizing the static structural stiffness of the HBS. Two test procedures were followed for the static load tests: tapping and non-tapping. Tapping is necessary to overcome the seal inherent dry-friction due to the relative motion among the seal components; thus relaxing the contact forces and allowing the seal to deflect during the loading and unloading process. For the non-tapping condition, results indicate that the HBS experiences a pronounced hysteresis effect as determined by the difference in results from the loading and unloading process. The results evidence the presence of dry friction effects between the seal components (bristles, pads, back and frontplate). Static structural stiffness identified for the non-tapping case increases almost 34% for the test pressure range. On the other hand, static seal stiffness obtained for the tapping condition increases about 15%; making these results more representative of the actual test seal static stiffness. The static seal stiffness derived from the tapping conditions is similar for both the loading and unloading cases (eliminating hysteretic effect). Additionally, a modified version of a computational program in [19] is used to predict the structural stiffness of the seal. The prediction is

within (15 %) of the radial stiffness of the HBS at a  $P_r = 1.0$ . The EDM structures connecting the pads to the seal casing account for (70 %) of the overall HBS stiffness.

Single frequency dynamic load tests (without shaft rotation) allow identification of the seal structural stiffness and equivalent viscous damping coefficients as a function of the pressure differential across the seal and under non-rotating conditions. The seal stiffnesses determined by the dynamic load tests for the test pressure range are within 18% (overall) of those identified from static load testing with tapping; thus indicating that resulting stiffnesses are representative to the operating seal stiffness. Mechanical energy dissipation parameters are identified for increasing supply pressures. The dry friction coefficient ( $\mu$ ) increases slightly as the pressure differential across the seal increases (5 % from  $P_r = 1.0$  to  $P_r = 3$ ). The increase of the dry friction coefficient is directly related to the increase of the contact forces between the seal components induced by the pressure differential across the seal. On the other hand, the loss factor coefficient ( $\gamma$ ) (material hysteresis) decays as the pressure ratio increases. This behavior is attributed to the repositioning of the bristles and the stiffening effect due to the pressure differential across the seal (i.e. blowdown effect).

Experiments were conducted to identify the rotordynamic force coefficients of a HBS subjected to unidirectional single frequency forcing functions while rotating at a constant speed under pressurized conditions. The model identifies the force coefficients in the frequency domain using force and displacement magnitudes measured during the testing process. The model assumes that the rotor gyroscopic effects for the test speeds are negligible, and that the direct deflections (i.e. in the direction of the force) about a centered seal are much larger than the cross deflections. Both assumptions are verified experimentally. The direct system stiffness coefficients ( $K_{xx}$ ) decreases about 15% and 5% with increasing rotor speed, 600 to 1,200 rpm, for  $P_r = 1.7$  and 2.4, respectively. The predicted HBS direct stiffness ( $K_{sxx}$ ) for 600 and 1,200 rpm correlates well (less than 5% lower) with the seal stiffness ( $K_s$ ) identified from rotordynamic tests at increasing pressure ratios. Predictions indicate that  $K_{sxx}$  (~110 kN/m) is approximately equal to the measured seal structural stiffness,  $K_s$  (~103 kN/m), implying that the gas film thickness

is much stiffer (order of magnitudes larger) than the compliant HBS pads and bristle matrix. The seal cross-coupled stiffness ( $K_{sxy} = -K_{syx}$ ) is at least one order of magnitude smaller than the seal direct stiffness ( $K_{sxx}$ ). The cross-coupled mass is negligible. The seal predicted direct damping coefficients ( $C_{sxx}$ ) are approximately equal to the equivalent viscous damping ( $C_{eq} \sim C_{sxx}$ ) derived from the test data for  $\gamma = 0.25$  to  $0.55$ . The seal viscous damping coefficient ( $C_{sxx}$ ) diminishes as a function of increasing excitation frequency, reaching a minimum value at the natural frequency of the test system ( $\sim 32$  Hz) with marginal dependence on rotor speed or supply pressure.

According to the seal manufacturer [17] the mechanical integrity and performance of the HBS will not change over time, mainly because the bristles do not wear as the bristles in conventional brush seals do; thus extending the life cycle of a HBS. Due to its robust design, a HBS operating with interference with the rotor can on occasion operate slightly off-centered (may occur during the assembly process) since the pads will lift-off from the surface of the rotor upon pressurization of the HBS and shaft rotation. Therefore, prolonging the life of a HBS by eliminating rotor and seal wear and issues associated with maintaining tight tolerances.

Further testing of the seal at higher gas temperatures and higher rotor speeds is recommended to evaluate the seal performance at conditions closer to the actual operating environment of an engine. A high temperature experimental facility (currently under construction) will allow this characterization of the HBS performance at higher supply pressures and temperatures.

## REFERENCES

- [1] Xi, J., and Rhode, D. L., 2006, "Rotordynamics of Impeller Eye Seals with Wear-Damaged Teeth in Centrifugal Compressors," *Tribol. Trans.* **49**(3), pp. 328-337.
- [2] Benckert, H. and Wachter, J., 1980, "Flow Induced Spring Coefficients of Labyrinth Seals for Applications in Turbomachinery," NASA CP2133.
- [3] Childs, D., and Vance, J.M., 1997, "Annular Gas Seals and Rotordynamics of Compressors and Turbines" *Proceedings of the 26<sup>th</sup> Turbomachinery Symposium*, Houston, TX, pp.201-220.
- [4] Proctor, M.E., and Delgado, I.R., 2004, "Leakage and Power Loss Tests Results for Competing Turbine Engine Seals," NASA TM-2004-213049.
- [5] Dogu, Y., and Aksit, M.F., 2006, "Brush Seal Temperature Distribution Analysis," *ASME J. of Eng. Gas Turbines Power*, **128** (3), pp.599-609.
- [6] Justak, J.F., and Crudgington, P.F., 2006, "Evaluation of a Film Riding Hybrid Seal," AIAA Paper No. 2006-4932.
- [7] Chupp, R.E., Hendricks, R.C., Lattime, S.B., and Steinetz, B.M., 2006, "Sealing in Turbomachinery," *AIAA J. of Prop. Power*, **22**(2), pp. 313-349.
- [8] Soto, E., and Childs, D., 1999, "Experimental Rotordynamic Coefficient Results for: (a) A Labyrinth Seal with and without Shunt Injection and (b) A Honeycomb Seal," *ASME J. of Eng. Gas Turbines Power*, **121**, pp.153-159.
- [9] Chupp, R.E., and Dowler, C.A., 1993, "Performance Characteristics of Brush Seals for Limited-Life Engines," *ASME J. of Eng. Gas Turbines Power*, **115**, pp.390-396.
- [10] Ferguson, J.G., 1988, "Brushes as High Performance Gas Turbine Seals," ASME Paper No. 88-GT-182.
- [11] Chupp, R.E., and Holle, G.F., 1996, "Generalizing Circular Brush Seal Leakage through a Randomly Distributed Bristle Bed," *ASME J. Turbomach.* , **118**, pp.153-161.
- [12] Basu, P., Datta, A., and Loewenthal, R., Short, J., 1994, "Hysteresis and Bristle Stiffening Effects in Brush Seal," *J. of Propul. Power*, **10**(4), pp.569-575.
- [13] Chew, J.W., and Hogg, S.I., 1997 "Porosity Modeling of Brush Seals," *J. Tribol.*, **119** (4), pp. 769-775.
- [14] Carlile, J.A., Hendricks, R.C., and Yoder D.A., 1993, "Brush Seal Leakage Performance with Gaseous Working Fluids at Static and Low Rotor Speeds Conditions," *ASME J. of Eng. Gas Turbines Power*, **115**(2), pp. 397-403.

- [15] O'Neill, A.T., Hogg, S.I., Withers, P.A., Turner, M.T., and Jones, T.V., 1997, "Multiple Brush Seals in Series," ASME Paper No. 97-GT-194.
- [16] Conner, J.K., and Childs, D., 1993, "Rotordynamic Coefficient Test Results for a Four-Stage Brush Seal," AIAA J. Prop. Power, **9**, pp.113-119.
- [17] Justak, J.F., 2002, "Robust Hydrodynamic Brush Seal," U.S. Patent No. 6,428,009.
- [18] Delgado, A., San Andrés, L., and Justak, J., 2003, "Identification of Stiffness and Damping Coefficients in a Shoed Brush Seal," *Proceedings of the VII Congreso y Exposición de Latinoamericana Turbomaquinaria*, Veracruz, Mexico, October, pp. 1-7.
- [19] Delgado A., San Andrés L., and Justak J.F., 2004, "Analysis of Performance and Rotordynamic Force Coefficients of Brush Seals with Reverse Rotation Ability," ASME Paper No.GT2004-53614.
- [20] Delgado, A., and San Andrés, L., 2007, "Identification of Structural Stiffness and Damping Coefficients of a Shoed-Brush Seal," ASME J. of Vib. Acoust., **129** (5), pp. 648-655.
- [21] Justak, J.F., 2007, "Hydrodynamic Brush Seal," U.S. Patent No. 7,182,345.
- [22] San Andrés, L., Baker, J. and Delgado, A., 2007, "Measurements of Leakage and Power Loss in a Hybrid Brush Seal," *Proceedings of the 6<sup>th</sup> EDF/LMS Poitiers Workshop*, Poitiers, France, November, pp. 10-18.
- [23] Delgado, A. and San Andrés, L., 2005, "Measurements of Leakage, Structural Stiffness and Energy Dissipation Parameters in a Shoed Brush Seal," *Sealing Technology*, **12**, pp. 7-10.
- [24] Stephen, D., and Hogg, S.I., 2003, "Development of Brush Seal Technology for Steam Turbine Retrofit Applications," ASME Paper No.IJPGC2003-40103.
- [25] Ginsberg, J. H., 2001, *Mechanical and Structural Vibrations*, John Wiley & Sons, Inc., NY, pp. 135-139.
- [26] Vance, J. M., 1988, *Rotordynamics of Turbomachinery*, John Wiley & Sons, Inc., New York.
- [27] Coleman, H. W., and Steele, G. W., 1988, *Experimentation and Uncertainty Analysis for Engineers*, John Wiley & Sons, New York. Chap. 1-4.

## APPENDIX A

### STATIC STRUCTURAL STIFFNESS MEASUREMENTS

The figures below depict the seal principal deflection versus static load for pressure ratios ranging from 1.3 to 3.0 under non-tapping and tapping testing conditions. The graphs corresponding to  $P_r = 1.0$ , for both testing conditions are introduced in Chapter V. Figures A1 to A6 establish the deflection pattern for both tapping and non-tapping testing for increasing pressure ratios ( $P_r$ ). In the case of the non-tapping testing the curves reveal a hysteretic effect since the deflection path during the loading process is considerably different than that during the unloading procedure. Also, the system never returns to its initial equilibrium position after the loading and unloading process. This behavior is due to the large friction forces present in the bristle pack, front and back plate. Consequently, the structural stiffness values for the non-tapping conditions are much higher than for those recorded during the tapping case. Importantly enough, the tapping tests yield a stiffness value closer to the seal structural stiffness identified from dynamic load tests.

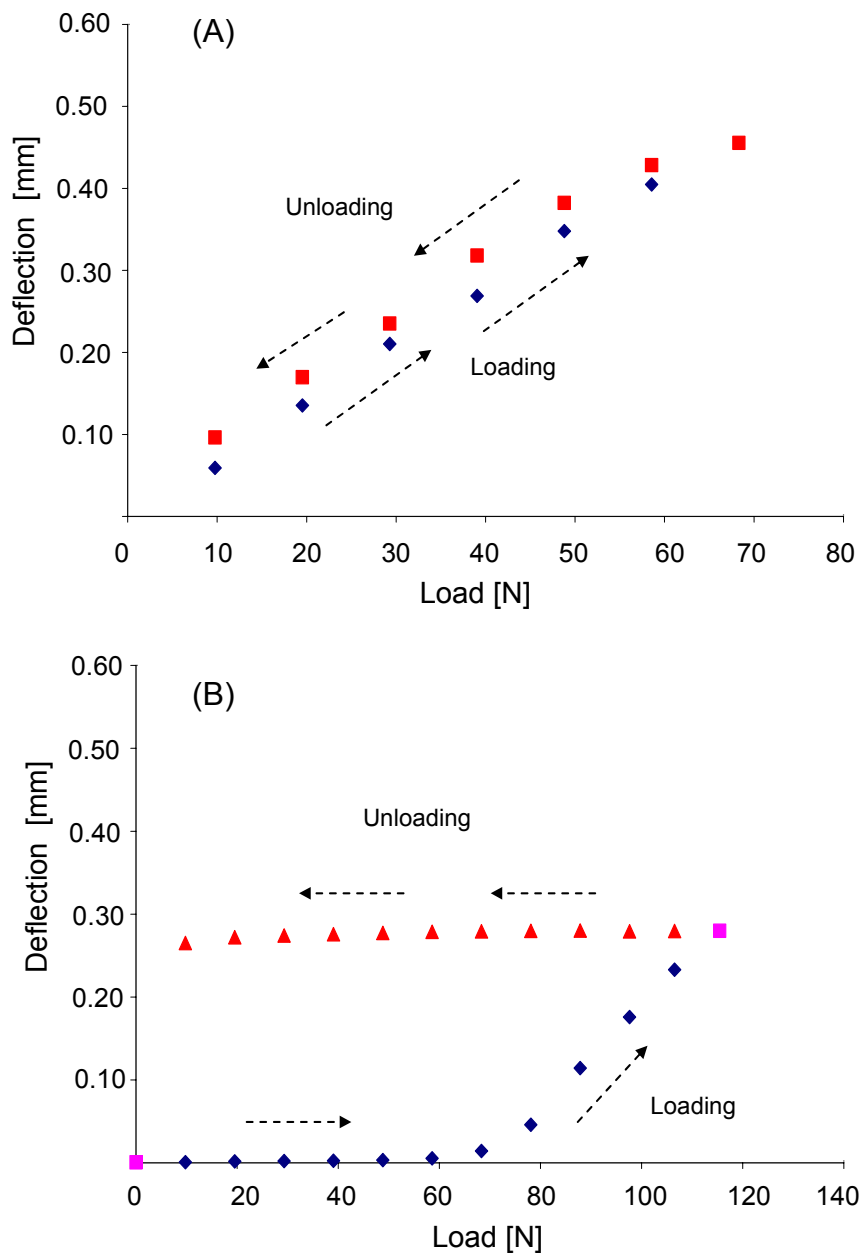


Figure A1 Seal direct deflection versus applied load at pressure ratio  $P_r=1.3$  for (A) tapping and (B) non-tapping testing conditions



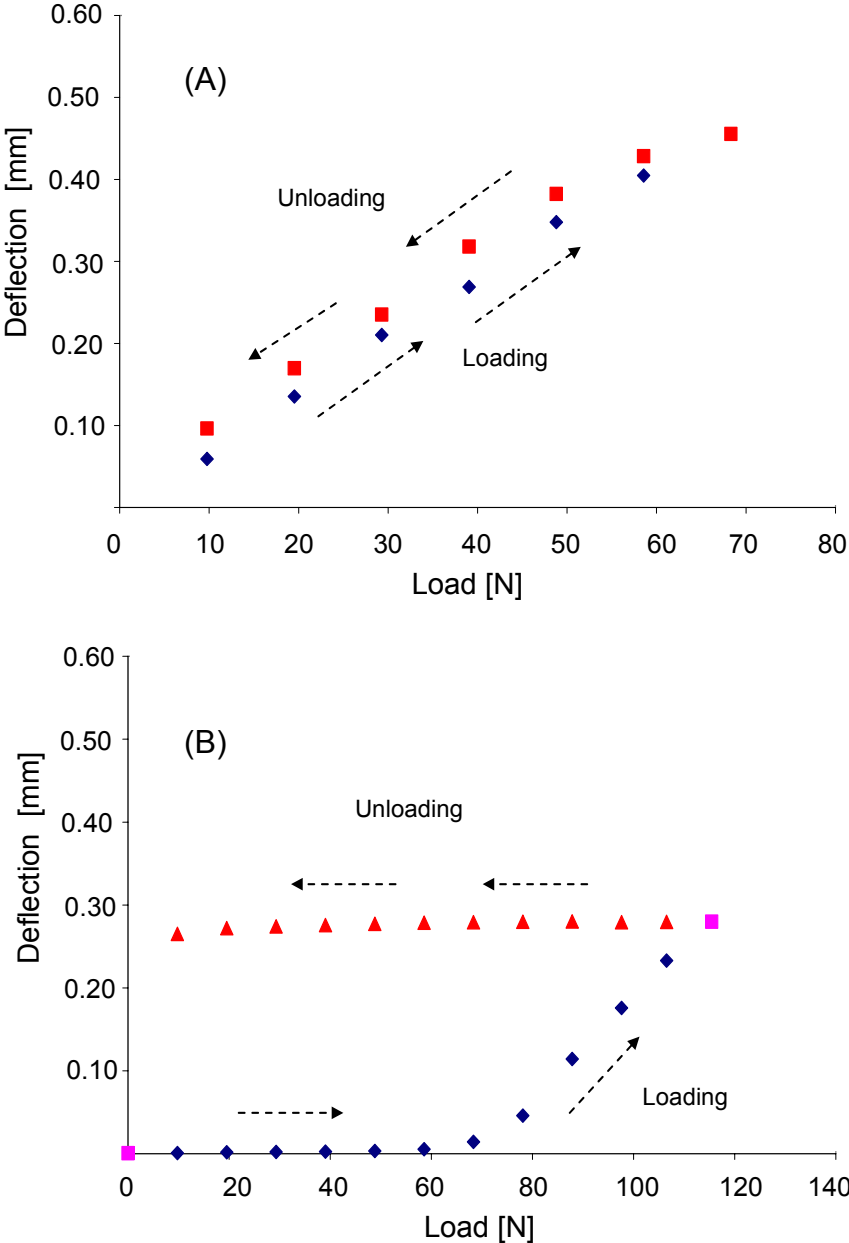


Figure A2 Seal direct deflection versus applied load at pressure ratio  $P_r=1.7$  for (A) tapping and (B) non-tapping testing conditions

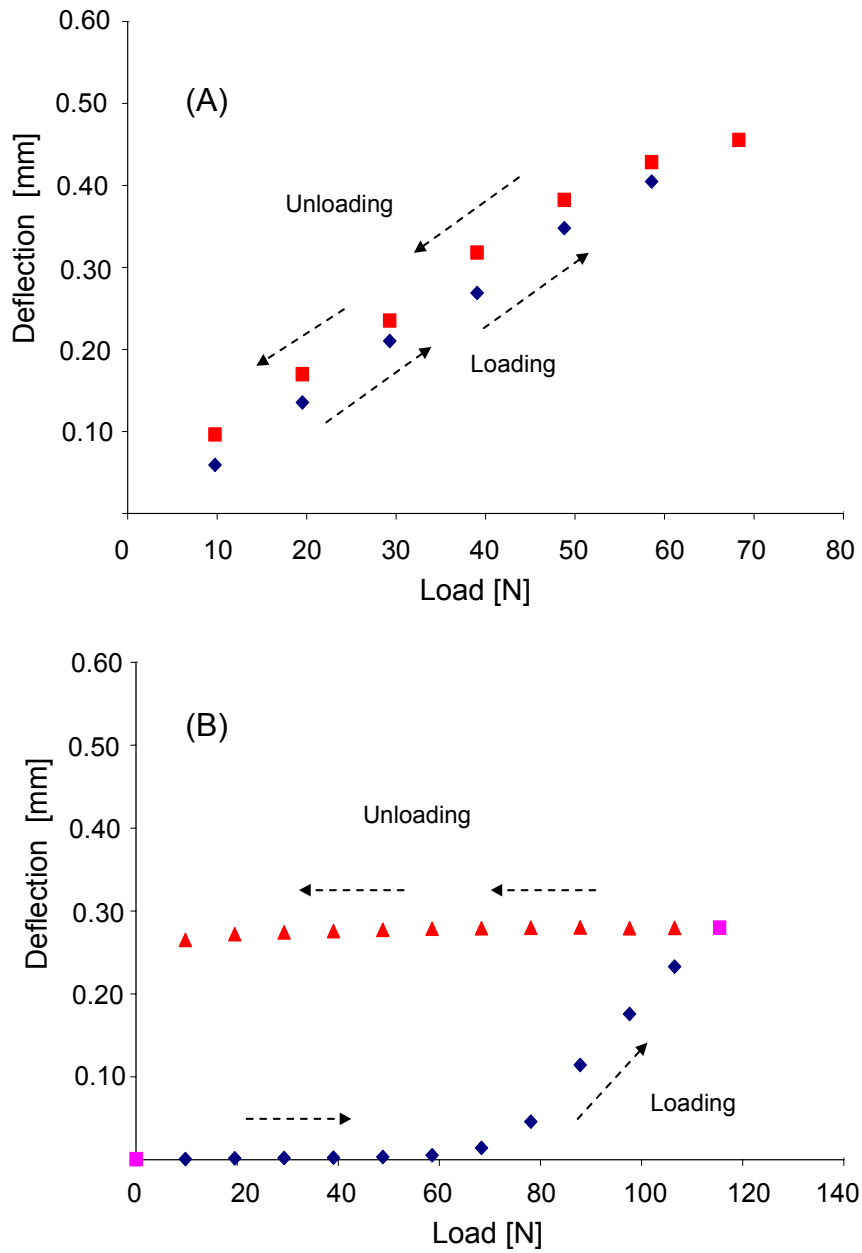


Figure A3 Seal direct deflection versus applied load at pressure ratio  $P_r=2.0$  for (A) tapping and (B) non-tapping testing conditions

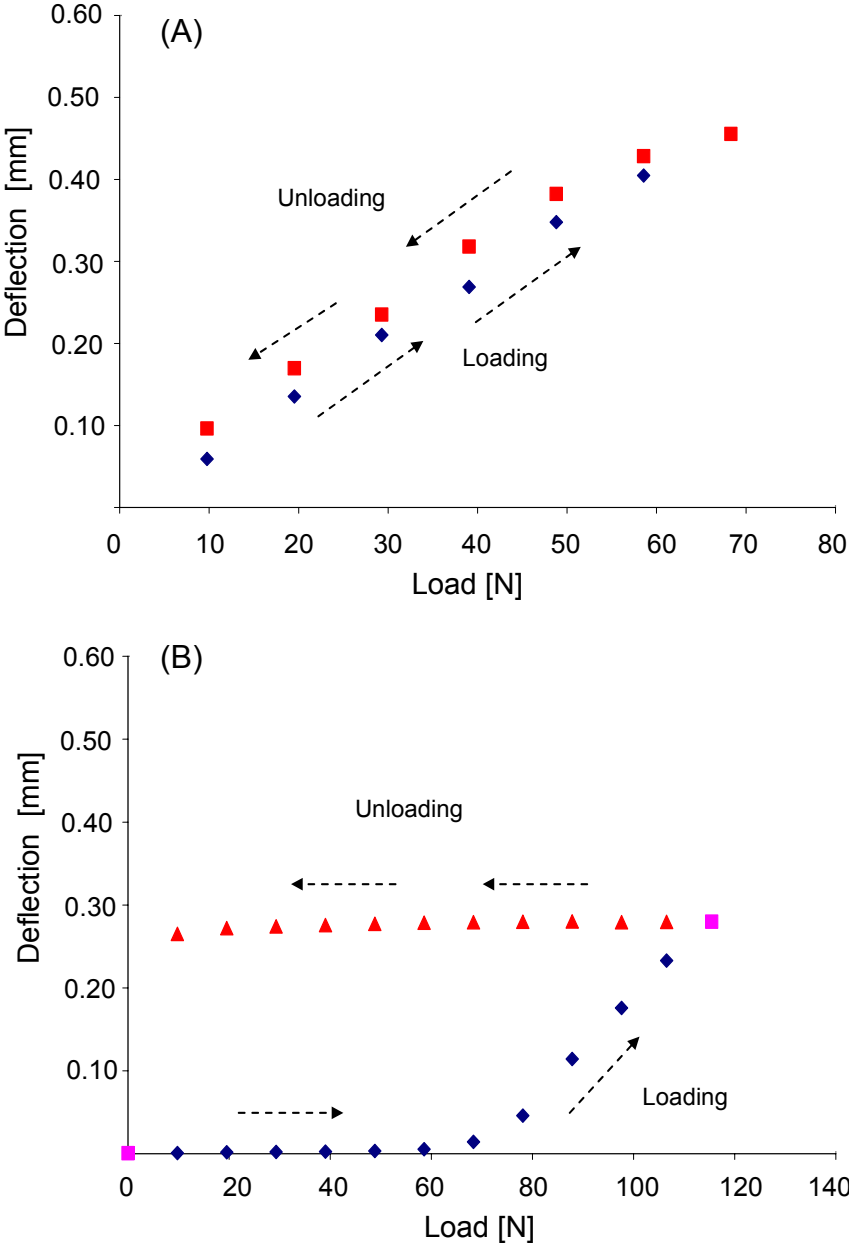


Figure A4 Seal direct deflection versus applied load at pressure ratio  $P_r=2.4$  for (A) tapping and (B) non-tapping testing conditions

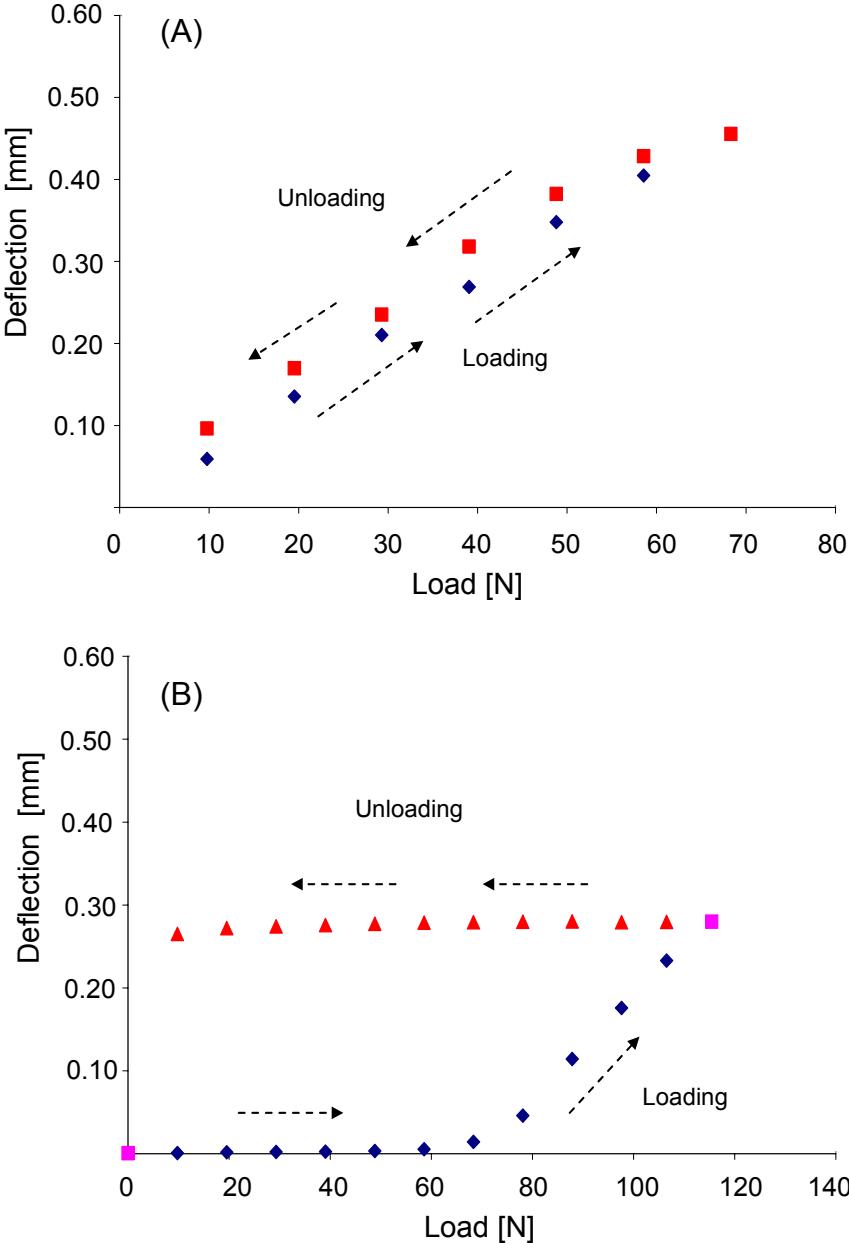


Figure A5 Seal direct deflection versus applied load at pressure ratio  $P_r=2.7$  for (A) tapping and (B) non-tapping testing conditions

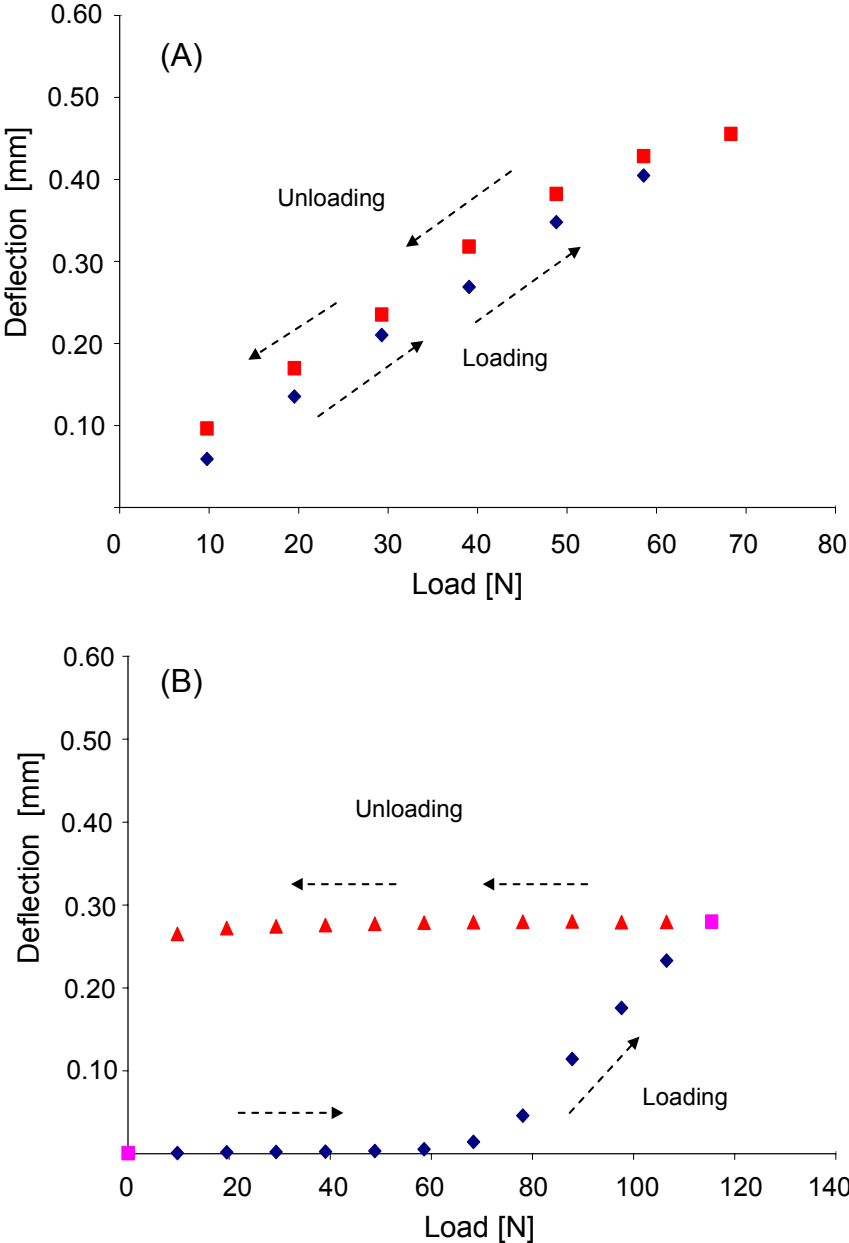


Figure A6 Seal direct deflection versus applied load at pressure ratio  $P_r=3.0$  for (A) tapping and (B) non-tapping testing conditions

## APPENDIX B

### PRECISION OF FLOW RATE MEASUREMENTS

The following derivation determines the precision limit of the mean of a sample of  $N$  flow rates measurements ( $m$ ) drawn from a Gaussian distribution [27]. The mean of a sample population is given by

$$\bar{m} = \frac{1}{N} \sum_{i=1}^N m_i \quad (\text{B.1})$$

The precision index or the sample standard deviation is given by

$$S_m = \left[ \frac{1}{N-1} \sum_{i=1}^N (m_i - \bar{m})^2 \right]^{\frac{1}{2}} \quad (\text{B.2})$$

The precision limit of the mean is calculated with the simple relation

$$P_m = tS_m \quad (\text{B.3})$$

where  $t$  is taken from Ref. [27].

The interval defined by  $\bar{m} \pm P_m$  gives the range within which it is expected, with 95% confidence, the next reading to lie if another one is taken.

**Table B1 Statistical data for measured flow rate under static condition (no shaft rotation) (English Units)**

Pressure Ratio, $P_r$	Flow Rate Mean Values Trial 1-8 [SCFM] $\bar{m}$	Sample Standard Deviation, $S_m$	Precision Limit, $\pm P_m$
1.3	7.12	0.43	1.00
1.5	9.40	0.35	0.82
1.7	12.08	0.67	1.58
1.9	14.54	0.79	1.86
2.0	17.84	0.79	1.85
2.2	20.57	0.65	1.54
2.4	23.21	0.72	1.69
2.5	25.95	0.56	1.32
2.7	29.65	0.64	1.50
2.9	33.38	0.55	1.29
3.0	35.41	1.08	2.54

**Table B2 Statistical data for measured flow rate under static condition (no shaft rotation) (SI Units)**

Pressure Ratio, $P_r$	Flow Rate Mean Values Trial 1-8 [g/s] $\bar{m}$	Sample Standard Deviation, $S_m$	Precision Limit, $\pm P_m$
1.3	4.13	0.25	0.58
1.5	5.45	0.20	0.47
1.7	7.00	0.39	0.92
1.9	8.43	0.46	1.08
2.0	10.34	0.46	1.07
2.2	11.93	0.38	0.89
2.4	13.46	0.42	0.98
2.5	15.05	0.32	0.76
2.7	17.19	0.37	0.87
2.9	19.36	0.32	0.74
3.0	20.54	0.62	1.47

## APPENDIX C

### IDENTIFICATION OF STRUCTURAL PARAMETERS OF ROTOR ASSEMBLY (ROTORDYNAMIC TEST RIG CONFIGURATION) FROM IMPACT TESTS

#### Experimental Set up and Procedure

A set of impact tests (i.e. an average of 5 impacts) performed along the  $X$  and  $Y$  directions on the rotor assembly, i.e. disk and shaft (see Figure 9) serve to identify the structural parameters of the assembly at the location of the seal. An additional set of tests performed on the rotor assembly characterize any change in the structural parameters resulting from connecting the assembly to the driver motor via a flexible coupling and quill shaft. Figure C1 shows a schematic view of the test set up and instrumentation.

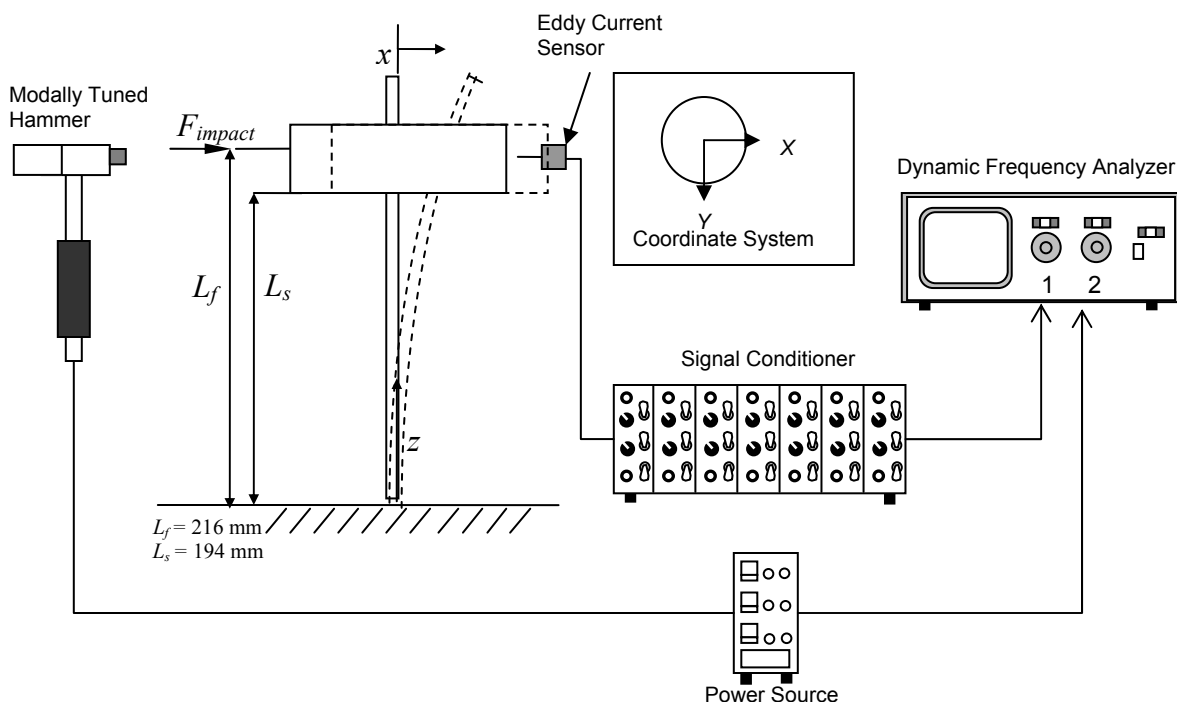


**Figure C1 Test schematic and instrumentation for structural parameter identification of HBS rotor assembly via impact load tests**



Figure C2 shows the 1020 steel disk and shaft prior to assembly. The disk and shaft masses are 3.57 kg and 0.88 kg, respectively.



**Figure C2** Disk and shaft prior to assembly

The instrumentation for the impact tests consists of:

- Two eddy current sensors ( $X, Y$ ) (207.7 mV/mil, 209.1 mV/mil)
- Modally tuned impact hammer (load cell .95 mV/lb) and power source
- Signal conditioner (to eliminate DC offset)
- Two channel frequency analyzer

### **Experimental Results**

Figure C3 depicts the time trace for the load and displacement measured by the eddy current sensor in the  $X$  direction only. Results in the  $Y$  direction are similar to those reported in the  $X$  direction. The response of the system is characterized by an oscillatory response with exponentially decaying amplitude. The assembly exhibits very low structural damping, taking a little over 4 seconds for the oscillations to fully decay.

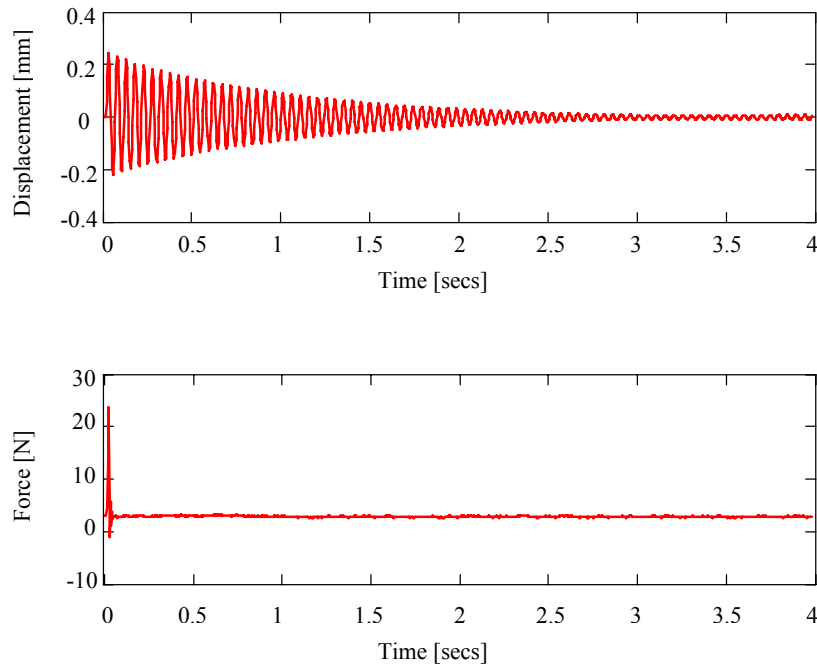


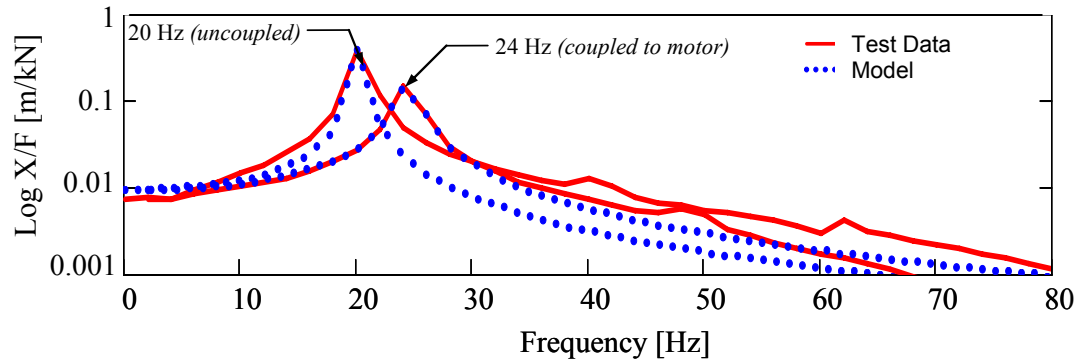
**Figure C3 Impact and displacement time traces for HBS rotor assembly**

A curve fit of the system response transfer function (displacement/force), obtained from averaging 5 impacts, yields the structural stiffness, equivalent mass and damping coefficient of the rotor assembly. A transfer function of the form

$$H(\omega) = \frac{1}{[(K_s^2 - M\omega^2) + (C_s \omega)^2]^{1/2}} = \frac{\bar{x}}{\bar{F}} \quad \text{A.1}$$

represents the dynamic flexibility of a linear system with viscous damping.

Figure C4 shows the transfer functions of the system with and without the flexible coupling and quill shaft attached to the free end of the rotor assembly. There is an increase in damping (~75%) after coupling the assembly to the motor; which results in a smaller amplitude response.



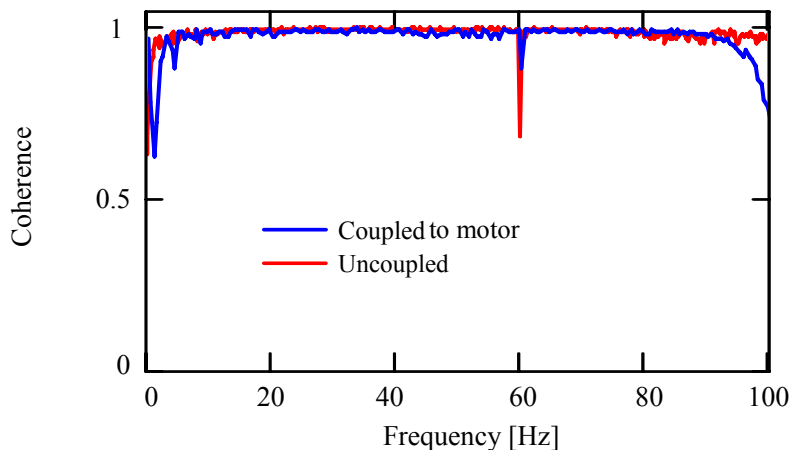
**Figure C4 Transfer function and model fit for rotor assembly uncoupled and coupled to drive motor (Range 0-80Hz)**

Table C1 presents the structural parameters of the rotor assembly identified from the transfer function. The model transfer shows good agreement with the measured data at frequency values close to zero ( $f \rightarrow 0$ ). Recall that the value of the function  $H(0)$  equals the flexibility coefficient ( $K_s^{-1}$ ). The mass estimated from the transfer function corresponds to the equivalent “vibrating” mass at the location of the impact corresponding to a specific vibration mode, (the fundamental mode shape in this case). For both cases the assembly exhibits very little damping on the order of 2% or less which is typical of steel structures [26]. The correlation factor,  $R^2$ , shows the goodness of curve fit of physical model to test data.

**Table C1 Identified parameters from impact tests exerted on rotor assembly (no HBS in place). Uncoupled and coupled to drive motor on rotordynamic test rig configuration**

Units	Parameters	No coupling	Coupled to motor
S.I.	Stiffness, $K_s$ [kN/m]	73( $\pm 4$ )	109( $\pm 7$ )
	Mass, M [kg]	4.4( $\pm 0.3$ )	4.6( $\pm 0.4$ )
	Damping, C [N-s/m]	8.1	32.3
US	Stiffness, $K_s$ [lbf/in]	417( $\pm 25$ )	624( $\pm 37$ )
	Mass, M [lb]	9.7( $\pm 0.5$ )	10.1( $\pm 0.5$ )
	Damping, C [lbs-s/in]	0.046	0.184
	Damping Ratio, $\zeta$	0.007	0.023
	Natural Frequency, $f_n$ [Hz]	20	24
	$R^2$ (correlation factor)	0.99	0.99
	Frequency Range: 1-80 Hz		

Figure C5 shows the coherence for the impact tests performed for both assembly configurations (i.e. without coupling and coupled to the motor). The high coherence values (from 10 to 40 Hz) indicate that transfer functions are valid and correspond to the actual system response due to the impact load.



**Figure C5 Coherence from an average of 5 impacts for rotor assembly uncoupled and coupled to drive motor**

### **Theoretical Prediction of Stiffness, Mass and Damping Coefficients of Rotor Assembly**

A prediction of structural stiffness and mass for the rotor assembly without the coupling in place are obtained using the fundamental static load deflection shape,

$\psi(z) = \frac{3Lz^2 - z^3}{2L^3}$ , for a cantilever circular beam [25]. Recall from Figure C2, the section

of the shaft inserted inside the disk is considerably thicker than the slender section. Consequently, it is expected that most of the shaft deflection will occur at  $z = L_s$ , see Figure C1.

The fundamental static shape is used to calculate the assembly parameters at the actual location the impact load,  $L_f$ , from the system potential and kinetic energies.

$$M_B = M_D \left( \frac{\psi(L_s)}{\psi(L_f)} \right)^2 + \int_0^{L_f} \rho A \psi(z)^2 dz; \quad (2)$$

$$K_{Beam} = \frac{3EI}{L_s^3} \left( \frac{\psi(L_s)}{\psi(L_f)} \right)^2$$

where  $M_D$  is the steel disk (3.58 kg) and  $(\rho, A, E, I)$  denote the shaft density, cross-sectional area, modulus of elasticity and moment of inertia.

Table C2 presents the predicted parameters for the disk and shaft assembly without coupling using the fundamental static shape of a cantilever beam. These results validate the experimental values shown in Table C1.

**Table C2 Predicted structural parameters of rotor assembly**

Units	Predicted Parameters	No coupling
S.I.	Stiffness, $K_{beam}$ [kN/m]	75.7
	Mass, $M_B$ [kg]	4.4
US	Stiffness, $K_{beam}$ [lbf/in]	432
	Mass, $M_B$ [lb]	9.7
	Natural Frequency, $f_n$ [Hz]	20

**APPENDIX D**

**NATURAL FREQUENCY AND MODE SHAPES OF ROTOR  
ASSEMBLY (ROTORDYNAMIC TEST RIG CONFIGURATION)**

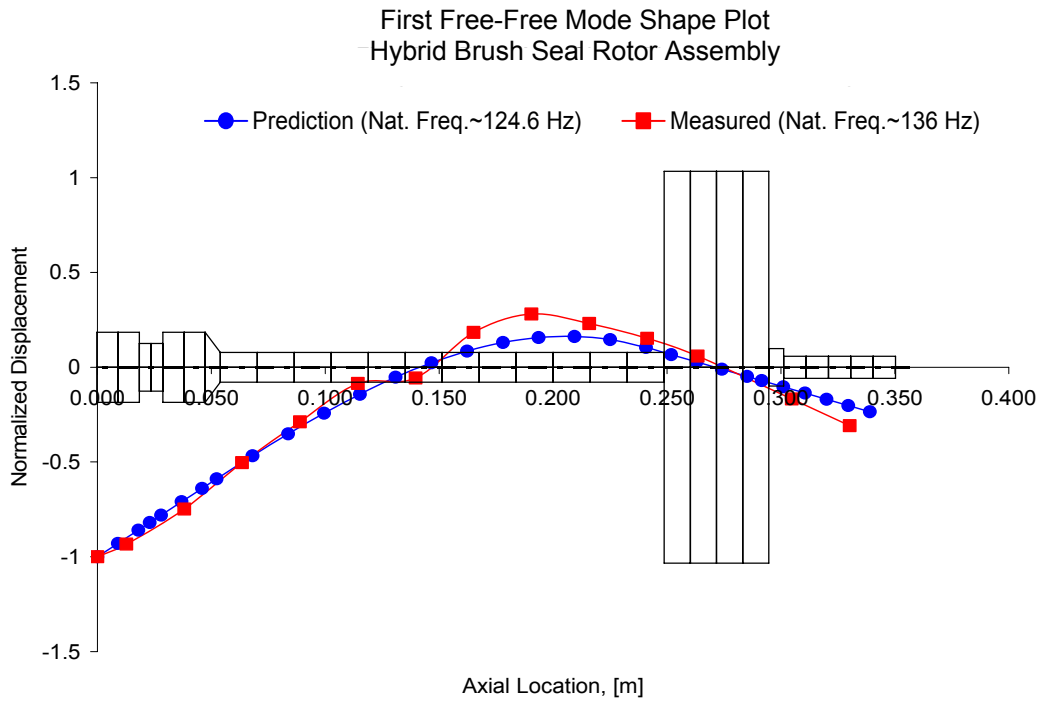
**Free-Free Mode Shapes**

Table D1 shows the experimental and predicted first three free-free mode natural frequencies of the rotor (disk and shaft) assembly for the rotordynamic test rig configuration. Predictions obtained using XLTRC<sup>2</sup> correlate well with experimental values. The maximum percent (~9.41%) difference occurs at the third natural frequency.

**Table D1 Natural Frequencies for rotor assembly, measurements and predictions.**

Free-Free Condition			
	Measured	Prediction	Percent Difference (%)
First Natural Freq. [Hz]	124.6	136	8.38
Second Natural Freq. [Hz]	770	822.6	6.39
Third Natural Freq. [Hz]	2407	2200	9.41

Figures D1 thru D3 show comparisons of the measured and predicted first, second and third free-free mode shapes for the rotor assembly. The figure shows excellent correlation between the measured and the predicted values. This also indicates that the geometric model for the test rotor is also accurate.



**Figure D1 First free-free mode shape for rotor assembly, measurements and predictions**

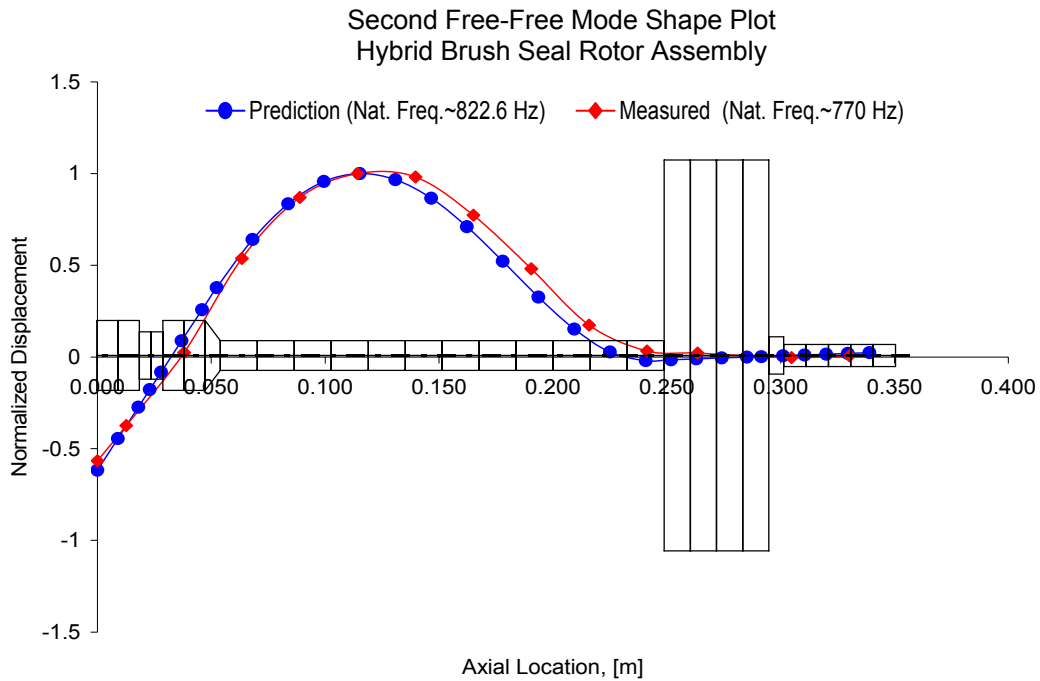


**Figure D2 Second free-free mode shape for rotor assembly, measurements and predictions**

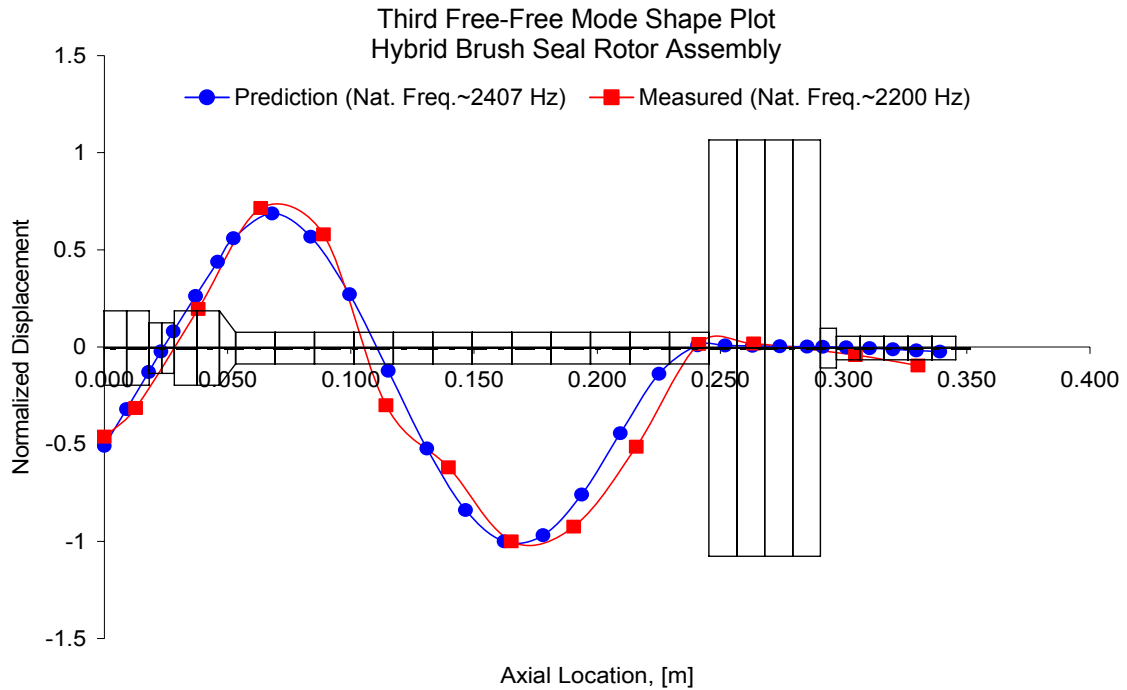


**Figure D3 Third free-free mode shape for rotor assembly, measurements and predictions**

### Fixed-Free Mode Shapes

Table D2 shows the experimental and predicted values obtained for the first two natural frequencies of the rotor assembly with the shaft end constrained by ball bearings. The measured natural frequencies correlate well with the predicted results. The maximum percent ( $\sim 5.21\%$ ) difference occurs at the second natural frequency.

**Table D2 Natural Frequencies for rotor assembly, measurements and predictions.**

	Fixed-Free Condition		
	Measured	Prediction	Difference (%)
First Natural Freq. [Hz]	20	21	5.00
Second Natural Freq. [Hz]	144	151.5	5.21

Figures D4 and D5 show the results obtained for the measured and predicted first, and second mode shapes for the rotor assembly, respectively. For the experimental case, the rotor assembly was constrained at one end (fixed at axial location = 0.0 m) and free



at the other end; like a cantilever beam. The first measured mode shape reproduces accurately the prediction calculated by XLTRC<sup>2</sup>.

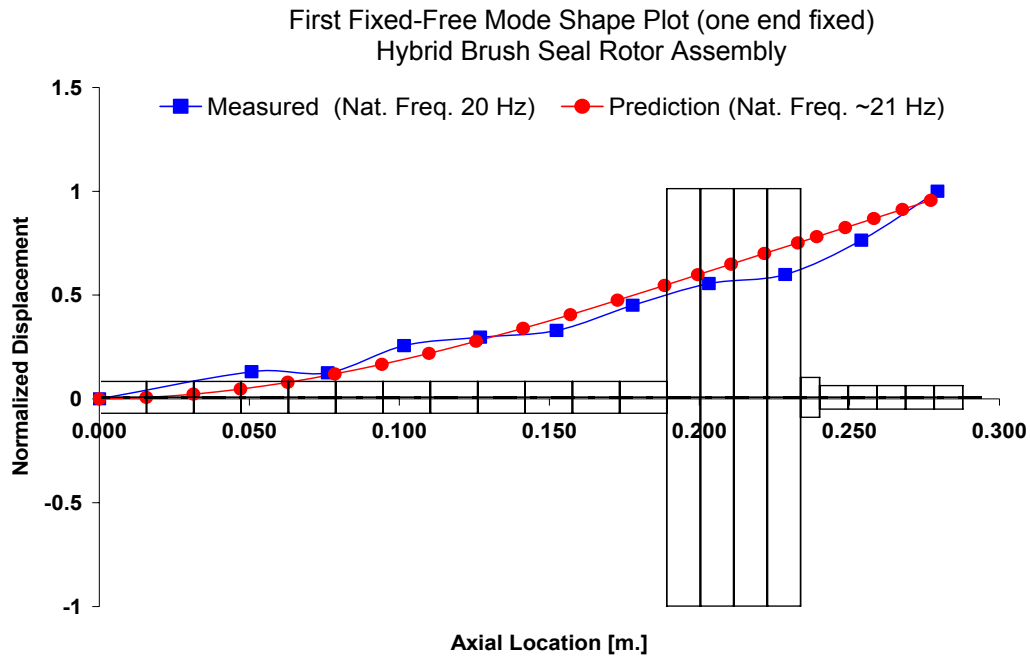
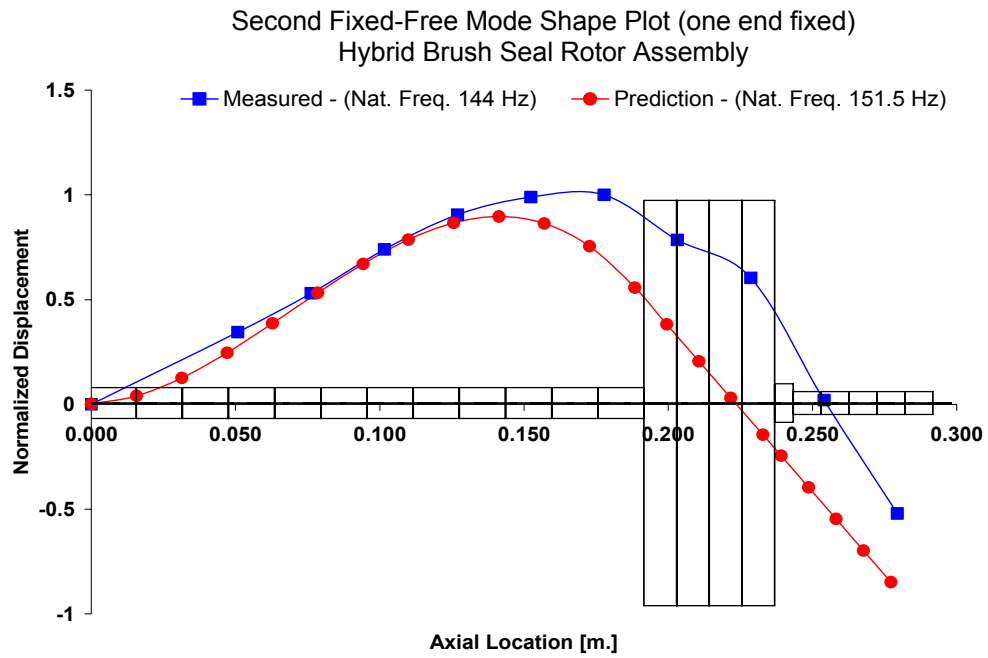


Figure D4 First fixed-free mode shape for rotor assembly, measurements and predictions



**Figure D5** Second fixed-free mode shape for rotor assembly, measurements and predictions

## APPENDIX E

### UNCERTAINTY ANALYSIS

This section details the estimation of the uncertainty associated to the experimental values presented in this report. The formulae and methodology follow definitions and procedures described by Coleman and Steel [27]. The uncertainty analysis includes the combination of precision errors associated to the instruments and repeatability of experimental results and their propagation. In general terms, the uncertainty associated to an experimental parameter ( $v$ ) is

$$U_v = \left[ \left( \frac{\partial v}{\partial x_1} U_{x_1} \right)^2 + \left( \frac{\partial v}{\partial x_2} U_{x_2} \right)^2 + \dots + \left( \frac{\partial v}{\partial x_i} U_{x_i} \right)^2 \right]^{1/2} \quad \text{E.1}$$

which can be rewritten as

$$\frac{U_v}{v} = \left[ \left( \frac{U_{x_1}}{x_1} \right)^2 + \left( \frac{U_{x_2}}{x_2} \right)^2 + \dots + \left( \frac{U_{x_i}}{x_i} \right)^2 \right]^{1/2} \quad \text{E.2}$$

In equation E.2 the individual sources of uncertainty correspond to precision errors introduced by the instrumentation and variability errors resulting from averaging independent test trials. The uncertainty associated to the variation of a set of data points can be assessed in terms of a precision index limit  $P_{\bar{x}}$ ,

$$P_{\bar{x}} = tS_{\bar{x}}, \quad S_{\bar{x}} = S_x / \sqrt{N} \quad ; \quad S_x = \left[ \frac{1}{N-1} \sum_{i=0}^N (X_i - \bar{X})^2 \right]^{1/2} \quad \text{E.3}$$

where  $S_{\bar{x}}$  represents the precision index of the mean value  $\bar{X}$  for  $N$  individual samples ( $\{X_i\}_{i=1, \dots, N}$ ) and  $t$  is the 95% confidence interval coefficient for a  $t$ -distribution of data points. The uncertainty associated to the instruments includes the combination and propagation of errors associated with their calibration and errors introduced by the data acquisition instruments. Appendix G presents the calibration curve of eddy current

sensors, flowmeter and pressure transducer. The overall uncertainty associated to a experimental parameter is

$$\bar{U}_v = (U_v^2 + P_x^2)^{1/2} \quad \text{E.4}$$

The uncertainty associated with the different types of measurements follow. The resulting uncertainty from all the experimental results is included in the figures presented in the report.

### Dynamic Loading Tests

The instrumental precision uncertainty of the stiffness and mass coefficients obtained from the dynamic load tests is represented by the uncertainty associated to the transfer function and the frequency measurements. i.e.

$$\frac{U_k}{C_k} = \left[ \left( \frac{U_\omega}{\omega} \right)^2 + \left( \frac{U_H}{H} \right)^2 \right]^{1/2} \quad \text{E.5}$$

The uncertainty of the measured impedance ( $H$ ) is

$$\frac{U_H}{H} = \left[ \left( \frac{U_{F_y}}{F_y} \right)^2 + \left( \frac{U_y}{y} \right)^2 \right]^{1/2} \quad \text{E.6}$$

where

$$\frac{U_\omega}{\omega} \leq 2.5\%, \frac{U_y}{y} \leq 3\%, \frac{U_{F_y}}{F_y} = 1\% \quad \text{E.7}$$

based on the instrumentation resolution and sensitivity calibration within its linear range. The error associated to the curve fit of the real part of the impedance  $\text{Re}(\bar{F}/\bar{x})$  follows from the standard error of estimate (SEE) of curve fit. For the different pressure tested the SEE ranges from 9 kN to 15 kN, which translates to a 9-11 % error for the stiffness and 4% for the mass estimates.

The error associated to the friction and loss coefficients is related to SEE of the dissipated energy curve fit. The SEE varies from  $2.09 \times 10^{-3}$  to  $4.52 \times 10^{-3}$  which yields an average variation of  $\sim 0.04$  and  $\sim 0.03$  for the dry friction and loss coefficient, respectively. In this case, the uncertainty associated to the instrumental precision error is negligible.

### Drag Torque Estimation

The uncertainty associated to the torque estimation combines the precision error introduced by the multimeters, tachometer, and the variation from averaging independent tests. Thus the precision uncertainty of the measured torque associated to the instrumentation is

$$\frac{\bar{U}_T}{T} = \left[ \left( \frac{\bar{U}_A}{A} \right)^2 + \left( \frac{\bar{U}_V}{V} \right)^2 + \left( \frac{\bar{U}_\omega}{\omega} \right)^2 \right]^{1/2} \quad \text{E.8}$$

with

$$U_A = 0.005 \text{ Amp}, \frac{U_\omega}{\omega} \leq 2.5\%, U_V = 0.0005 \text{ Volt} \quad \text{E.9}$$

Combining equation E.9 with the precision index calculated from C.2 yields the overall uncertainty of the torque estimation.

### Leakage Tests

The air flow is measured using a turbine flowmeter. The precision error associated to the instrument is ( $\pm 0.2$  scfm) as indicated by the manufacturer. The precision uncertainty is

$$\frac{\bar{U}_{\dot{m}}}{\dot{m}} = \left[ \left( \frac{\bar{U}_{\dot{q}}}{\dot{q}} \right)^2 + \left( \frac{\bar{U}_f}{f} \right)^2 \right]^{1/2} \quad \text{E.10}$$

with  $U_{\dot{q}} = \pm 0.2$  scfm and  $U_f = \pm 0.05$  Hz. Above,  $\dot{q}$  represents the volumetric flow rate and  $f$  the frequency acquired with a multimeter.

## APPENDIX F

### EVALUATION OF DISK AND SEAL WEAR

The rotor and seal were disassembled to inspect their surfaces after 10 combined hours of rotation at pressurized (~8 hours) and unpressurized conditions (~2 hours). Figure F1 shows the surface profile of the disk along its axial span. Note, the scale for the ordinate (i.e. surface profile) is in micrometers and the abscissa (i.e. axial length) is in millimeters. Measurements show disk wear of nearly 60 micrometers at the seal location. The significant surface wear of the disk mainly occurred during tests performed with shaft rotation and without external air pressurization ( $P_r = 1.0$ ).

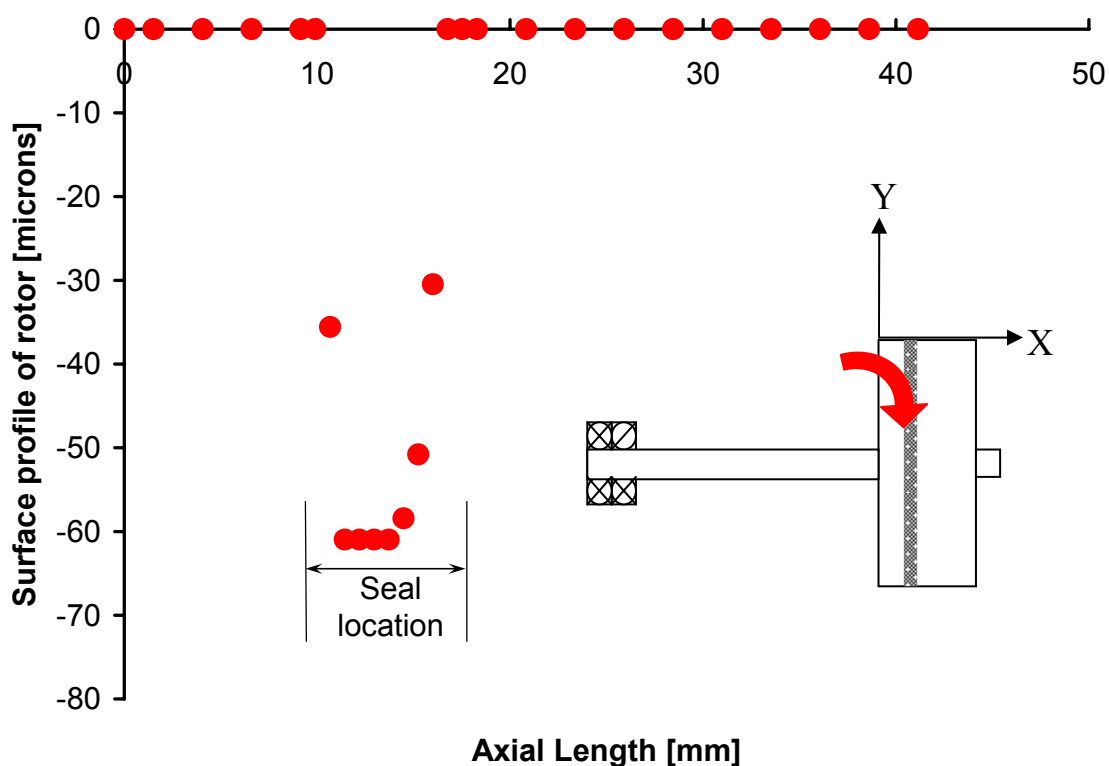
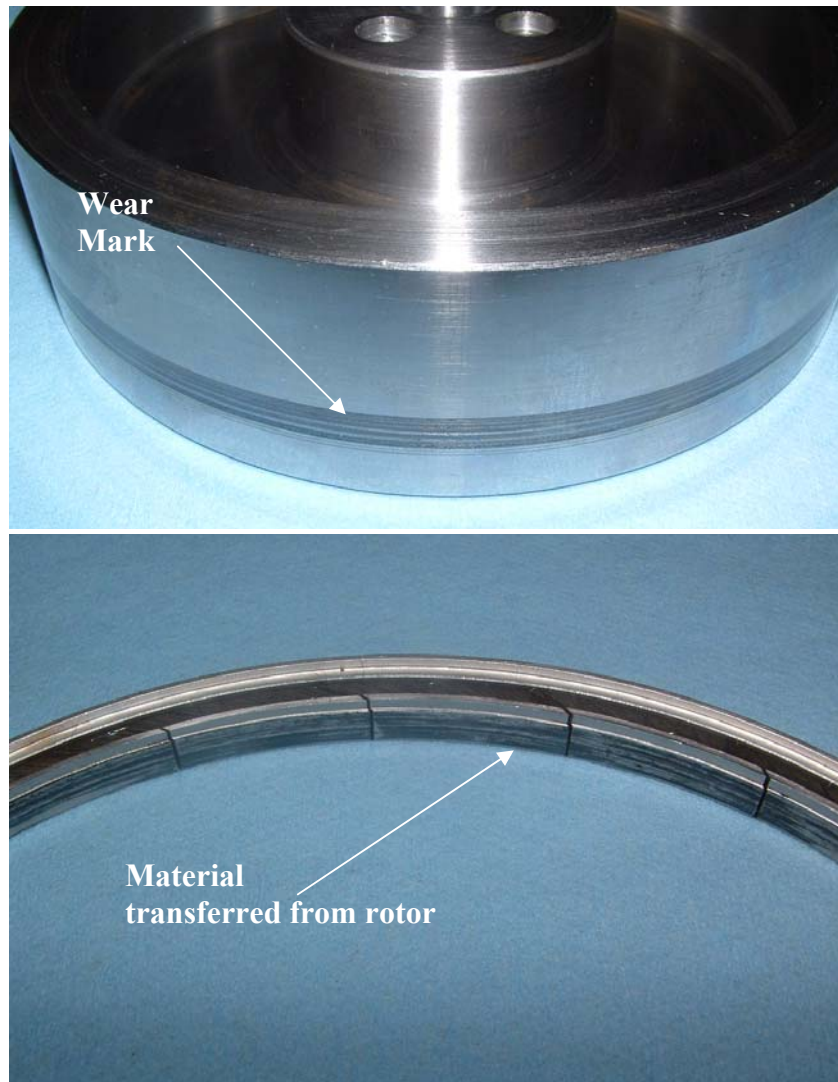


Figure F1 Surface profile of disk along its axial span. Estimation of wear after 10 hours of operation (tests with shaft rotation)

Figure F2 shows a close up photograph showing the wear conditions of the disk and HBS after rotating tests. Wear marks are readily visible on the disk surface. Also, visual inspection of the HBS shows metal residue on seal pads indicating material transfer from the rotor during rotating tests with no air pressurization.



**Figure F2 Close up photograph of disk and HBS for wear assessment after tests with shaft rotation**

## APPENDIX G

### CALIBRATION OF INSTRUMENTATION

#### Pressure Sensors

Figure G1 shows the voltage versus pressure curve resulting from a calibration performed with a dead weight tester.

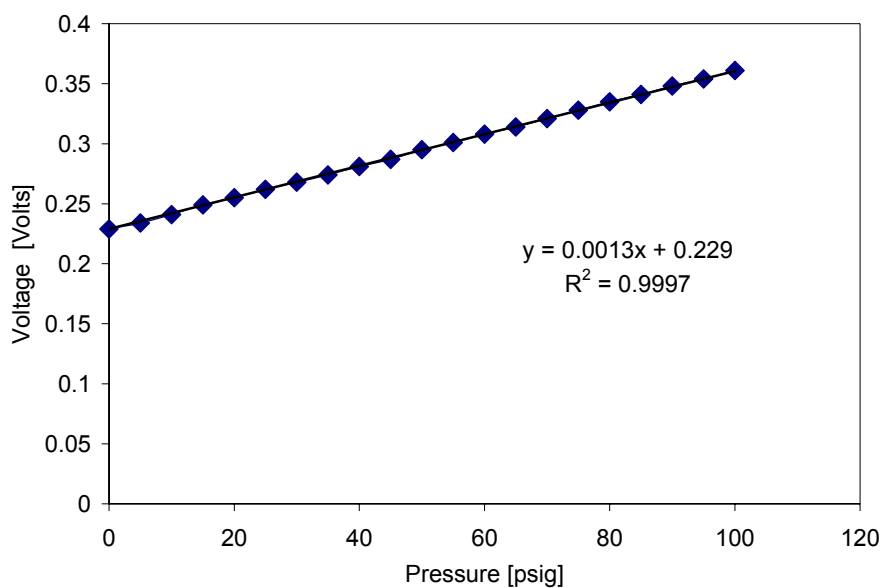


**Figure G1 Output voltage versus applied pressure using a dead weight tester**

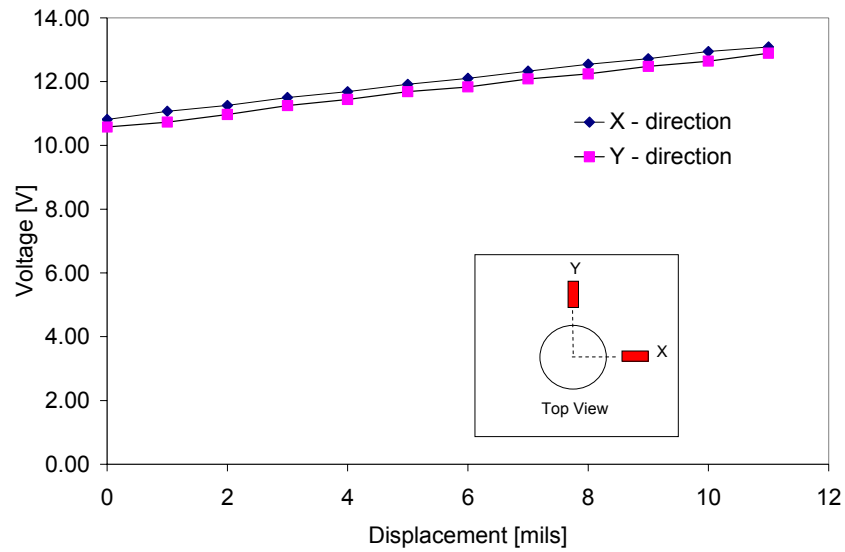
#### Eddy Current Sensors

Table G1 present the gain of the eddy current sensors resulting from a calibration conducted on a lathe equipped with high precision position sensors. The actual was used as target. Figure G2 depicts the calibration curve for the two sensors.

**Table G1 Eddy current sensors gain estimated from calibration tests.**

	<i>X</i>	<i>Y</i>
Gain[mV/mils]	209.9	207.8
R <sup>2</sup>	0.9984	0.9988
Range[volts] ~	-10.6 to -12.9	-10.8 to -13.1
Uncertainty	2%	2%





**Figure G2 Output voltage of eddy current sensor versus measured displacement. Calibration curve**

### **Turbine Flowmeter**

Figure G3 shows the calibration curve for turbine flowmeter Serial#120872 and Model# FT-12NEYABGEH-5. The data points are provided from the manufacturer Flow Technology Inc. The uncertainty associated to the calibration is +/-0.2 scfm.

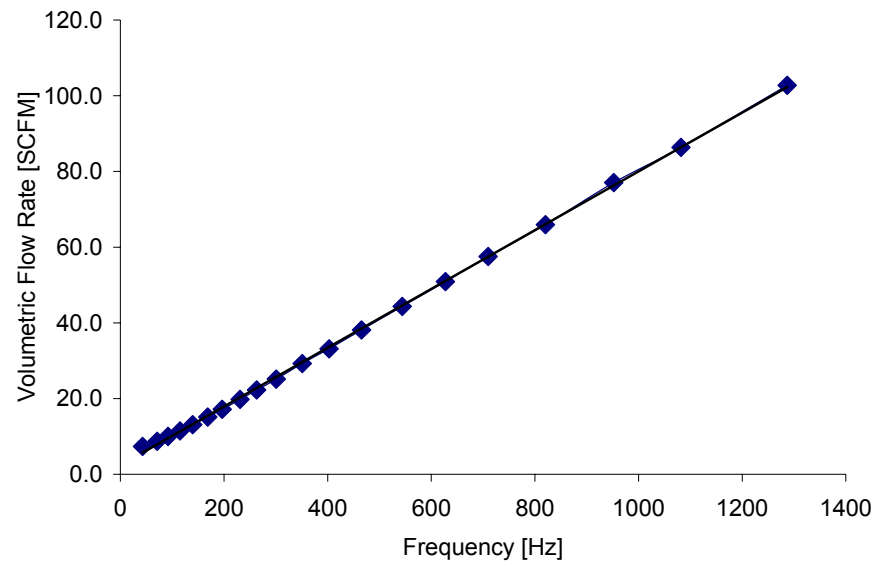


**Figure G3 Volumetric flow rate versus output frequency (turbine flowmeter). Data provided from manufacturer. (Upstream pressure 100 psi)**

**VITA**

Name: José Enrique Baker

Address: Department of Mechanical Engineering, 3123 TAMU,  
College Station, TX 77843, USA

Email: jbakerv@yahoo.com

Education: B.S., Mechanical Engineering, University of New Orleans,  
New Orleans, LA, 2005

M.S., Mechanical Engineering, Texas A&M University,  
College Station, TX, 2007

Permanent Address: 801 Toulouse St. Apt. D  
New Orleans, LA 70005, USA